https://lib.uliege.be https://matheo.uliege.be

Mémoire

Auteur : Wiels, Morgane
Promoteur(s) : Bonfond, Bertrand
Faculté : Faculté des Sciences
Diplôme : Master en sciences spatiales, à finalité approfondie
Année académique : 2024-2025
URI/URL : http://hdl.handle.net/2268.2/23961

Avertissement à l'attention des usagers :

Tous les documents placés en accès ouvert sur le site le site MatheO sont protégés par le droit d'auteur. Conformément aux principes énoncés par la "Budapest Open Access Initiative"(BOAI, 2002), l'utilisateur du site peut lire, télécharger, copier, transmettre, imprimer, chercher ou faire un lien vers le texte intégral de ces documents, les disséquer pour les indexer, s'en servir de données pour un logiciel, ou s'en servir à toute autre fin légale (ou prévue par la réglementation relative au droit d'auteur). Toute utilisation du document à des fins commerciales est strictement interdite.

Par ailleurs, l'utilisateur s'engage à respecter les droits moraux de l'auteur, principalement le droit à l'intégrité de l'oeuvre et le droit de paternité et ce dans toute utilisation que l'utilisateur entreprend. Ainsi, à titre d'exemple, lorsqu'il reproduira un document par extrait ou dans son intégralité, l'utilisateur citera de manière complète les sources telles que mentionnées ci-dessus. Toute utilisation non explicitement autorisée ci-avant (telle que par exemple, la modification du document ou son résumé) nécessite l'autorisation préalable et expresse des auteurs ou de leurs ayants droit.

UNIVERSITY OF LIEGE
FACULTY OF SCIENCES
DEPARTMENT OF ASTROPHYSICS, GEOPHYSICS AND OCEANOGRAPHY

SEARCHING FOR WAVES ON JUPITER'S MAGNETOPAUSE

Author: Morgane Wiels

Supervisor: Bertrand Bonfond

Reading Committee:
Grégor Rauw
Benoît Hubert
Gaël Buldgen
Bertrand Bonfond

MASTER IN SPACE SCIENCES - RESEARCH FOCUS
ACADEMIC YEAR 2024–2025

Acknowledgements

Firstly, I would like to express my sincere gratitude to Bertrand Bonfond for his guidance and invaluable support throughout this year. I feel extremely fortunate to have worked on such a fascinating subject as Jupiter's magnetosphere, and it is thanks to him that I was introduced to the study of magnetopause perturbations and the methods to detect them.

I am also grateful to him for giving me the opportunity to present my work to the Juno magnetosphere group, which was an enriching experience. In this context, I warmly thank all those who provided constructive feedback on my presentation, in particular Denis Grodent, Jean-Claude Gérard, and Alessandro Moirano.

Secondly, I thank the members of the reading committee -Grégor Rauw, Benoît Hubert, Gaël Buldgen, and Bertrand Bonfond- for the time they devoted to the reading of this manuscript.

To my family, thank you for your unwavering support throughout my life, and especially during this academic journey. To my parents, a special thank you for the Euro Space Centre and Utopiales trips, which played a decisive role in helping me find my path.

To my dear friends Clarice, Léa, and Maëlle, thank you for your unconditional love during these past years. To Lara, Apolline, Perrine, Marine, Guillaume, Pierre, and Nathan, thank you for making my university years so full of joy and laughter. To my Astrobees, I am deeply grateful for our adventures that always cheer me up.

Last but certainly not least, I would like to thank my partner, Guillaume. You are my constant, the one who never fails to make me laugh, and you have been an incredible source of support over the past six years. I cannot wait to celebrate the next chapters of life with you. I love you.

Abstract

The magnetosphere of Jupiter is the largest object inside the heliosphere, with a volume equivalent to 70,000 times that of the Sun. If Jupiter's magnetosphere were visible in the sky, it would be bigger than the Moon. This vast region has been observed by numerous spacecraft since the dawn of space exploration and is still being investigated to this day. In this master's thesis, we examine the boundary between the Jovian magnetosphere and the interplanetary space: the magnetopause. We analyse the measurements of various spacecraft to search for waves on its surface, and discuss their potential origin.

In Chapter 1, we present theoretical notions necessary for the comprehension of this work. We introduce the magnetosphere of Jupiter and its inner dynamics, along with our boundary of interest: the magnetopause. Afterwards, we take an interest in the different mechanisms that create boundary waves on its surface. We then introduce the model of magnetopause used throughout the entire work, dependent on the solar wind dynamic pressure.

Chapter 2 contains the presentation of the different space missions and their related magnetic field data. We also exhibit their different trajectories around Jupiter, and we establish the list of magnetopause crossings essential for the following computations.

In Chapter 3, we introduce the five different boundary analysis methods that enable us to calculate the normal to the Jovian magnetopause, with two possible options for the choice of the window of operation.

We present these computed normals for the dawn and dusk sides of Jupiter's magnetosphere in Chapter 4, along with the statistical results for the crossings of all the spacecrafts combined. Afterwards, we take an interest in specific cases of consecutive crossings that we study in detail in Chapter 5.

Chapter 6 allows us to address the reliability of our results and methods, and to question them in the context of the different mechanisms creating waves on the Jovian magnetopause.

Last but not least, we conclude on our results and evoke the potential perspectives for future improvements in Chapter 6.4.

The results that could not be included in the main text can be found in the different appendices of this document.

Contents

Chapter 1

About Jupiter's magnetopause

1.1 Jupiter

Jupiter stands as a planet of superlatives in the Solar System: it is the largest planet, the fastest rotator, and possesses the densest planetary atmosphere, the strongest magnetic field, and the most extensive magnetosphere. As the fifth planet from the Sun, this gas giant represents an extreme environment, shaped by its unique combination of temperature, pressure, and composition.

Jupiter is thought to have formed through the process of core accretion: a solid core gradually grew by accumulating planetesimals until it reached a critical mass, triggering the rapid gravitational contraction of its surrounding envelope. This initiated runaway gas accretion from the solar nebula, ultimately giving rise to the massive hydrogen–helium planet we observe today [Mizuno, Nakazawa, and Hayashi, 1978]. However, the formation of gas giants is more intricate than the simple core accretion model suggests, and remains an active topic of research. Jupiter's origin and evolution are of particular interest because they offer valuable insights into the study of exoplanets, especially hot Jupiters [Ikoma and Kobayashi, 2025].

The visible atmosphere of Jupiter is recognisable: it is organised into alternating dark belts and bright zones, shaped by powerful zonal winds flowing both in the prograde and retrograde directions relative to the planet's rotation [Helled, Movshovitz, and Nettelmann, 2023]. In rapidly rotating fluid planets, such banded patterns emerge from the interplay of the Coriolis force, the transfer of energy and momentum from small-scale features to large-scale jets, and the conservation of angular momentum and potential vorticity as differentially heated air moves across latitudes [Guillot et al., 2022].

Early models described Jupiter's interior as three distinct layers: a compact core of heavy elements, surrounded by a helium-rich shell of metallic hydrogen, and topped by a helium-poor molecular hydrogen envelope [Helled and Howard, 2024]. More precise gravity data from the Juno mission have since led to refined structural models that include composition gradients and account for dynamical effects [Helled, Movshovitz, and Nettelmann, 2023]. The core is now believed to contain not only heavy elements but also significant amounts of hydrogen and helium, potentially forming a diluted core extending over a large fraction of the planet's radius (several tens of percent) [Helled and Howard, 2024]. Between the inner and outer envelopes lies a transition region with variable helium abundance, where helium droplets are thought to form and precipitate [Guillot et al., 2022].

Jupiter has 95 officially recognised moons. The four largest —Io, Europa, Ganymede, and Callisto— discovered by Galileo Galilei in 1610, are collectively known as the Galilean moons. Each is remarkable in its own way: Io is the most volcanically active body in the Solar System; Ganymede is the largest moon; and Europa may harbour a subsurface ocean beneath its icy crust, potentially capable of supporting life [NASA, 2025a].

Jupiter has been observed by numerous spacecraft, including Pioneer 10 and 11, Voyager 1 and 2, Galileo, Cassini, and Juno, with Europa Clipper scheduled to join them in the near future. The planet's atmosphere, magnetosphere, and auroras remain the focus of extensive ongoing research.

1.2 Magnetosphere and magnetopause

As discussed earlier, Jupiter possesses the strongest magnetic field and the largest magnetosphere in the Solar System. Its magnetic field is predominantly dipolar, with the magnetic axis tilted by about 10° relative to the rotation axis. The interaction between this magnetic field and the solar wind shapes the planet's magnetosphere, defined as the region in which the magnetic field dominates over other forces. The outer boundary, the *magnetopause*, marks the location where the planet's magnetic pressure balances the dynamic pressure of the solar wind, separating magnetospheric plasma from solar wind plasma. A second boundary, the *bow shock*, forms upstream of the magnetosphere where the fast solar wind slows abruptly upon encountering the obstacle [Guillot et al., 2022; Krishan K Khurana et al., 2004].

The terrestrial magnetosphere is the most extensively studied example, with the solar wind acting as the primary source of plasma and energy, which is stored and dissipated within the magnetosphere–ionosphere system. By contrast, Jupiter's magnetosphere operates on fundamentally different principles: external solar wind inputs of mass and energy are relatively minor compared to its powerful internal sources [Krupp et al., 2004].

Over most of its volume, Jupiter's magnetosphere is governed by planetary rotation. Internal plasma sources are dominated by its moons, which inject approximately 10^3 kg/s of SO_2 from Io and about 50 kg/s of O_2 from Europa. This neutral material is ionised and subsequently picked up by the motional electric field generated by Jupiter's rapid rotation. The resulting plasma is subject to strong centrifugal forces, driving outward radial transport. However, as the plasma moves away from the planet, the conservation of angular momentum causes it to gradually depart from rigid corotation [Saur, Chané, and Hartkorn, 2018].

Jupiter's rotation-driven magnetosphere shares similarities with that of Saturn: plasma originates from ionised neutral gases emitted by volcanic moons (Io for Jupiter, Enceladus for Saturn), and corotates with the planet's $\sim$ 10-hour period through strong magnetic coupling. These rotational flows generate significant centrifugal forces, confining the plasma into a relatively thin disk [Fran Bagenal and Peter A. Delamere, 2011].

Within the first $10R_J$[1] lies the inner magnetosphere, where the strong planetary magnetic field organises plasma motion along field lines and tightly couples it to Jupiter's rotation. The dominant plasma source is Io's volcanic output of neutral SO_2 gas, which dissociates and ionises into multiple charge states of sulfur and oxygen. These ions form the *Io plasma torus* between $5.2\,R_J$ and $10\,R_J$, a doughnut-shaped structure with pronounced radial, longitudinal, and latitudinal variations in density and temperature. This region also hosts Jupiter's intense radiation belts, composed of highly energetic electrons trapped in the strong magnetic field [Fran Bagenal, 2024; Krishan K Khurana et al., 2004; Roth et al., 2025].

Between $10\,R_J$ and $40\,R_J$ lies the middle magnetosphere, where plasma gradually departs from full corotation with Jupiter. Here, the plasma is confined to a thin plasma sheet centred on the magnetic equator. In this region, magnetic field lines become increasingly stretched as they balance plasma pressure against intense centrifugal and thermal pressures [Krishan K Khurana et al., 2004].

Figure 1.1 shows a side view of Jupiter's magnetosphere with the Sun to the left. The solar wind flows from the left, encountering the bow shock before entering the magnetosheath —a region of shocked solar wind plasma— bounded internally by the magnetopause. Inside the magnetosphere, the magnetic field lines, the Io plasma torus, and the equatorial current sheet are illustrated, the latter stretching the field lines outward from the planet.

1.3 Searching for waves

Jupiter's magnetopause is highly dynamic and is subject to deformation by multiple mechanisms that will be examined in detail in the following sections; boundary waves may arise from the interaction of corotating plasma with the magnetopause or the influence of the solar wind.

In this study, we analyse magnetic field measurements from multiple missions that have explored the Jovian magnetosphere, computing magnetopause

---

[1] R_J is Jupiter's equatorial radius, 71,492 km, approximately eleven times Earth's radius.

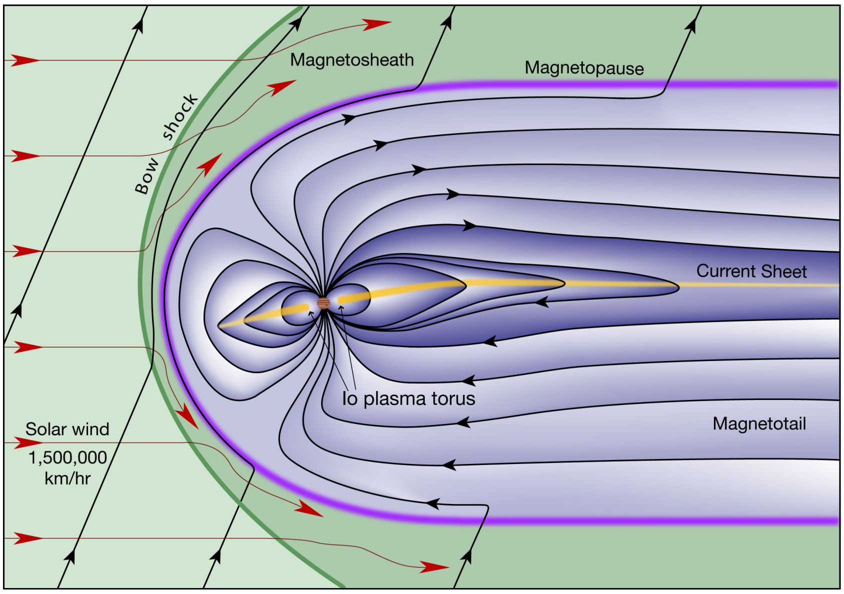

Figure 1.1: The Jovian magnetosphere, viewed from the side. The Sun is on the left, and the solar wind meets the magnetosphere at the magnetopause, establishing the bow shock. The magnetic field lines are represented, as well as the Io plasma torus, current sheet, magnetosheath and magnetotail. Figure from Fran Bagenal and Bartlett (2025).

normals as a proxy for identifying boundary waves. We then assess potential wave-generation mechanisms at Jupiter's magnetopause, focusing on the centrifugal interchange instability, the Kelvin–Helmholtz instability, and compression–decompression events.

1.3.1 Centrifugal interchange instability

Consider a layer of dense fluid overlying a lighter one under the influence of gravity. In this configuration, the Rayleigh–Taylor instability develops, producing characteristic "fingers" of dense fluid penetrating into the lighter fluid. The centrifugal interchange instability follows the same physical principle, but in the context of Jupiter's magnetosphere.

As described earlier, plasma in Jupiter's magnetosphere originates primarily from Io, forming a torus of various ionisation states of sulfur and oxygen [Krishan K Khurana et al., 2004]. Since plasma cannot accumulate indefinitely, there must be a mechanism to transport it outward from the disk region [Tanaka et al., 2023]. The centrifugal interchange instability fulfils this role, driving large-scale radial plasma transport in a process analogous to the Rayleigh–Taylor instability [Ma, P. Delamere, and Otto, 2016].

In this analogy, the cool, dense Io plasma torus corresponds to the heavy fluid, the hot and less dense plasma of the outer magnetosphere plays the role of the lighter fluid, and the effective gravity is provided by the centripetal acceleration associated with Jupiter's rapid rotation [Krupp et al., 2004].

Because of the frozen-in condition, radial plasma outflow carries magnetic flux away from Jupiter's inner magnetosphere. A compensating inward flow must occur to replace the displaced flux [Ma, P. Delamere, and Otto, 2016]. This exchange is mediated by the interchange instability, in which dense plasma on field lines in the Io plasma torus swaps places with lighter plasma on more distant field lines [Tanaka et al., 2023].

The criterion for centrifugal interchange instability can be derived under different assumptions, such as considering only centrifugal forces or including magnetic curvature effects [Achilleos et al., 2015]. In the simplest case of a cold plasma —where thermal energy is negligible compared to rotational kinetic energy— the instability occurs when the plasma content per unit magnetic flux decreases with radial distance. In the Io plasma torus, the maximum flux-tube content is found near Io's orbit, making regions beyond it unstable while the inner edge remains stable [Krupp et al., 2004].

In the cold-plasma approximation, the stability condition is

$$\mathbf{g} \cdot \nabla \eta \geq 0,$$

where $\eta = \int (\rho/B)\, ds$ is the mass per unit magnetic flux, and $\mathbf{g}$ the effective gravity [Achilleos et al., 2015]. If a flux tube is displaced outward into a region where η increases, the system remains stable. Conversely, if η decreases in that direction, the system becomes unstable and interchange motion develops.

When plasma "fingers" generated by the centrifugal interchange instability corotate with Jupiter and interact with the magnetopause, they can introduce spatial and temporal variability along the boundary [Feng, Binzheng Zhang, et al., 2023]. Figure 1.2, adapted from the supporting information of Feng, Binzheng Zhang, et al. (2025), is the result of a three-dimensional global Jovian magnetosphere magnetohydrodynamic (MHD) simulation. It shows the density distribution in Jupiter's magnetosphere viewed from the top or the side for high and low mass-loading rates. The image serves here as a visual illustration: from the top view, radial plasma fingers are seen extending outward from Jupiter, corotating from the dawn side to the dusk side, and grazing the magnetopause near the noon region.

1.3.2 Kelvin-Helmholtz instability

Consider two superposed horizontal layers of immiscible fluid. When both layers are at rest, their interface remains flat. If the layers move with different horizontal velocities —such as wind blowing over the sea— the interface still remains flat provided the velocity difference is below a critical threshold. However, when the velocity shear exceeds this threshold, the Kelvin–Helmholtz instability (KHI) develops, producing undulations along the interface.

For the incompressible, ideal MHD case, the onset condition for KHI is given

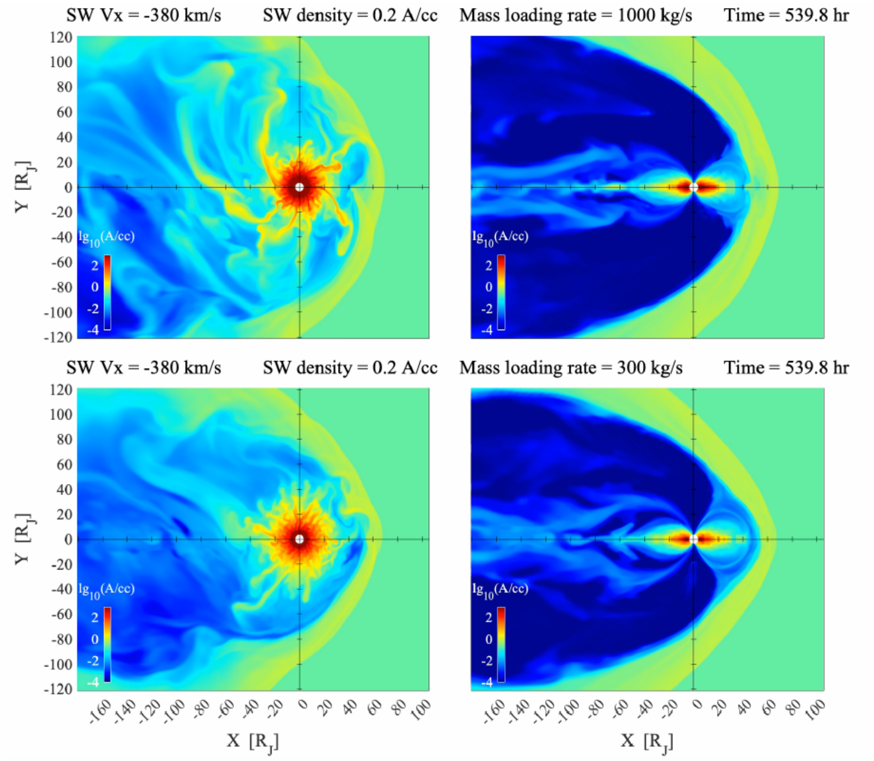

Figure 1.2: Figure from Feng, Binzheng Zhang, et al. (2025). The left figures show the density distribution viewed from the top, and right figures show the density distribution viewed from the side for high mass loading rate (top two panels) and low mass loading rate (bottom two panels) cases at ST = 539.8 hour. The Sun is considered on the right in this figure.

by Montgomery et al. (2023):

$$[\mathbf{k} \cdot (\mathbf{v}_{\mathrm{MSP}} - \mathbf{v}_{\mathrm{MSH}})]^2 > \frac{\rho_{\mathrm{MSP}} + \rho_{\mathrm{MSH}}}{\mu_0 \rho_{\mathrm{MSP}} \rho_{\mathrm{MSH}}} \left[(\mathbf{k} \cdot \mathbf{B}_{\mathrm{MSP}})^2 + (\mathbf{k} \cdot \mathbf{B}_{\mathrm{MSH}})^2 \right], \tag{1.1}$$

where $\mathbf{k}$ is the wave vector, $\mathbf{v}$ the plasma velocity, $\mathbf{B}$ the magnetic field, ρ the mass density, and μ_0 the permeability of free space. Subscripts MSP and MSH refer to the magnetosphere and magnetosheath, respectively. Physically, instability arises when the velocity shear across the boundary exceeds the stabilising effect of magnetic tension; if magnetic tension dominates, the boundary remains stable.

Processes at the magnetopause are fundamental to the transport of plasma, momentum, and energy from the solar wind into the magnetosphere [Otto and Fairfield, 2000]. The Kelvin-Helmholtz instability has been detected at the magnetopauses of Earth, Saturn, and Jupiter.

At Earth, Otto and Fairfield (2000) and Fairfield et al. (2000) found evidence for KHI at the magnetopause in the form of vortices propagating past the spacecraft. Their results indicated substantial transport of magnetosheath plasma into the magnetosphere via magnetic reconnection occurring within KHI vortices. Subsequent multi-spacecraft missions have enabled statistical studies demonstrating that KHI is a common feature of Earth's magnetopause [Masson and Nykyri, 2018].

At Saturn, Masters et al. (2009) identified KHI-driven surface waves on the dawn flank of the magnetopause, while Cutler et al. (2011) reported their presence on the dusk flank — an unexpected result, as this region was previously thought to be stable to the instability. P. Delamere, Wilson, et al. (2013) found that most KHI activity occurred on the dusk flank, suggesting that the subsolar magnetopause may be particularly susceptible to KHI onset, with vortices subsequently transported toward dusk by magnetospheric co-rotation. More recently, Feng, Zheng, et al. (2025) used three-dimensional global MHD simulations to investigate dawn–dusk asymmetries, finding that vortices on the dusk side propagate more stably, whereas those on the dawn side are subject to more variable and complex dynamics. They concluded that KHI events are significantly more likely to be observed in the dusk sector.

In Jupiter's rotationally dominated magnetosphere, plasma is largely confined to an equatorial disk in the outer magnetosphere, which interacts with tailward-flowing magnetosheath plasma. This configuration produces strong velocity shear across the magnetopause, creating conditions favourable for KHI [Montgomery et al., 2023]. When the velocity shear exceeds magnetic tension, perturbations can grow into vortices characteristic of the instability's non-linear stage. These processes facilitate the transport of solar wind plasma, magnetic flux, and momentum into Jupiter's magnetosphere [P. Delamere and Bagenal, 2010].

Ma, P. Delamere, Schok, et al. (2022) analysed perturbations on the dawnside, low-latitude flank of Jupiter's magnetopause, attributing them to possible KHI driven by the large velocity shear between tailward magnetosheath flow and sunward corotating magnetospheric plasma. Using the multi-fluid Lyon–Fedder–Mobarry (MFLFM) global magnetosphere model, Zhang et al. (2018) simulated the interaction between the solar wind and Jupiter's rapidly rotating magnetosphere. Their results, the first global simulations to capture KHI in the subsolar region, show that vortices predominantly occur in the dusk sector. The simulations suggest that KHI modes grow in the pre-noon and subsolar regions before being advected toward dusk by magnetospheric flows.

Figure 1.3 shows an example from these simulations, where KHI waves are clearly visible at the magnetopause boundary between the magnetosphere and magnetosheath.

1.3.3 Compression/decompression

It is well established that Earth's magnetosphere responds to variations in solar wind dynamic pressure. For example, Sibeck, Lopez, and Edmond C Roelof (1991) quantified how the shape and position of the magnetopause vary under different solar wind conditions. Southwood and Margaret G Kivelson (1990) reviewed how a magnetospheric cavity reacts to perturbations in external pressure at the mag-

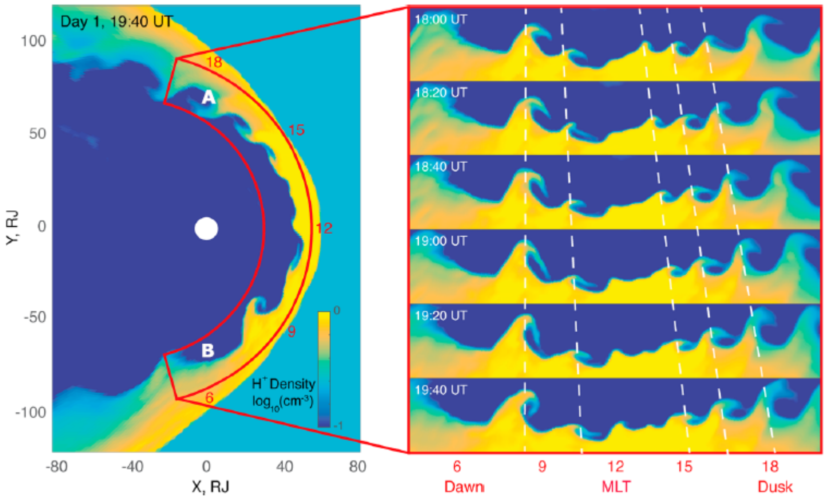

Figure 1.3: Figure from Zhang et al. (2018), representing Kelvin-Helmholtz instability at Jupiter's magnetosphere. The left figure is a snapshot of H^+ number density in the equatorial plane at 19:40 ST, while the right figure shows the temporal evolution of the K-H vortices between 18:00 and 19:40 ST.

netopause, showing that such effects can propagate down to ionospheric altitudes.

Changes in solar wind dynamic pressure can also excite boundary waves along the magnetopause. Analysing over a decade of data, Song, Elphic, and Russell (1988) showed that under northward interplanetary magnetic field conditions, the magnetopause position changes can be attributed to pressure fluctuations and/or magnetic reconnection. They concluded that the Kelvin-Helmholtz instability, previously thought to be the dominant driver of such surface waves, plays at most a minor role on the dayside magnetopause for oscillations with periods longer than about two minutes.

Jupiter's magnetosphere is among the most dynamic in the Solar System, with the subsolar magnetopause observed to vary between $\sim 40\,R_J$ and $\sim 100\,R_J$ over short timescales. On average, it is more expanded during solar minimum and more compressed during solar maximum [Krupp et al., 2004]. The stand-off distance is set primarily by the balance between the solar wind dynamic pressure and the planet's internal magnetic and plasma pressures. Rotational stresses further stretch the magnetic field, enhancing the internal pressure and contributing to the large overall size [Krupp et al., 2004].

A probabilistic model for the shape and location of Jupiter's magnetopause as a function of solar wind dynamic pressure was developed by Joy et al. (2002) and will be introduced in the following section.

Single-spacecraft observations at Jupiter have shown that the magnetopause moves inward and outward in response to solar wind dynamic pressure changes. At Earth, multi-spacecraft measurements have proven crucial for understanding such motion by providing snapshots of transient events in progress. One of the few comparable cases at Jupiter was reported by Kurth et al. (2002), who described a near-simultaneous magnetopause crossing observed by both the Cassini and Galileo spacecraft. Each recorded only a single outbound crossing on that day, ruling out Kelvin-Helmholtz instability, which would produce small-amplitude, periodic boundary oscillations. Assuming negligible internal variability, the authors attributed the motion to a compression of the magnetopause by an increase in solar wind dynamic pressure.

Figure 1.4 comes from Kurth et al. (2002), and shows the trajectories of Cassini and Galileo near the crossing time. The orange curve represents a qualitative model of the magnetopause, with observed crossings marked by triangles. The figure illustrates the change from an expanded to a compressed magnetopause (propagating "fold"), highlighting how such transient events can perturb the boundary surface and be detectable when searching for magnetopause waves at Jupiter.

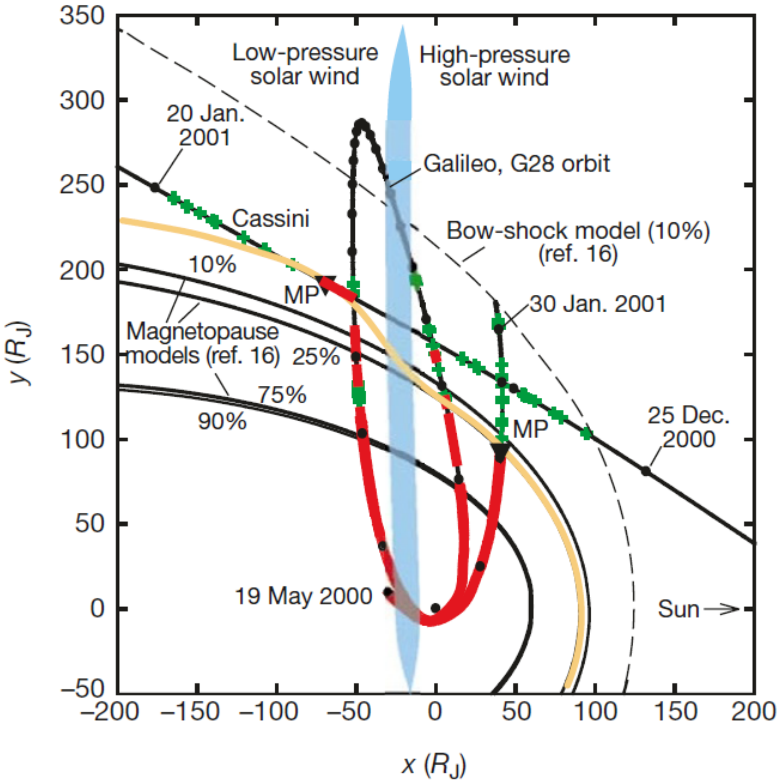

Figure 1.4: Figure from Kurth et al. (2002), representing of the trajectories of Cassini and Galileo during the time interval surrounding the Cassini closest approach. The coordinate system is centred on Jupiter with the positive X axis directed from Jupiter to the Sun, the Z axis is normal to Jupiter's orbital plane with positive north, and the Y axis completes an orthogonal system. On both trajectories, crosses indicate the bow shock crossings and triangles the magnetopause crossings. Intervals with thick red lines indicate times when the spacecrafts were in the magnetosphere. For comparison, four magnetopause models and one bow-shock model are shown [Joy et al., 2002]. Also included is a qualitative model of the magnetopause in orange.

This event is a rare example of two-point observations of the Jovian magnetopause, capturing its transition from a more extended to a more compressed configuration. The response closely parallels Earth's magnetopause behaviour, reinforcing the applicability of terrestrial models to Jupiter [Kurth et al., 2002].

1.4 Joy's magnetopause

In this master's thesis, we compute the normals to Jupiter's magnetopause using several methods and compare them to an established empirical model by Joy et al. (2002). Their model was constructed using observations from Pioneer 10 and 11, Voyager 1 and 2, Ulysses, and Galileo, combined with boundary characteristics derived from a magnetohydrodynamic simulation, to determine the positions of Jupiter's bow shock and magnetopause.

The simulation employed a coordinate system with the X axis pointing Sunward, the Z axis aligned with Jupiter's spin axis (positive in the direction of angular momentum), and the Y axis completing the right-handed frame, positive towards dusk. This reference frame, hereafter referred to as the *Jupiter Missions* frame, will be used for all figures in this work.

In the MHD simulation, points belonging to either the bow shock or the magnetopause surface were fitted via the least squares method to a second-degree polynomial of the form

$$z^2 = A(P_d) + B(P_d)\,x + C(P_d)\,x^2 + D(P_d)\,y + E(P_d)\,y^2 + F(P_d)\,xy, \tag{1.2}$$

where P_d is the solar wind dynamic pressure, and the coefficients A–F are defined below.

This functional form was chosen to allow for dawn-dusk asymmetry and polar flattening or steepening, while imposing north-south symmetry. Earlier models typically employed conic sections, which lack this flexibility.

Both the magnetopause and bow shock locations vary with P_d, and the corresponding coefficients differ for the two boundaries. When implementing the model, one must account for the fact that the coefficients were derived using distances scaled by $R_J/120$ to reduce numerical errors in the least-squares fit. As this study focuses on the magnetopause, the coefficients for that boundary are

$$\begin{aligned}
A(P_d) &= -0.134 + 0.488\,P_d^{-1/4},\\
B(P_d) &= -0.581 - 0.225\,P_d^{-1/4},\\
C(P_d) &= -0.186 - 0.016\,P_d^{-1/4},\\
D(P_d) &= -0.014 + 0.096\,P_d,\\
E(P_d) &= -0.814 - 0.811\,P_d,\\
F(P_d) &= -0.050 + 0.168\,P_d.
\end{aligned}$$

Because Joy's magnetopause model depends explicitly on solar wind dynamic pressure, it can be used to examine how P_d influences the boundary shape. Figure 1.5 shows the magnetopause in the XY plane for increasing P_d. Higher dynamic pressure shifts the magnetopause closer to Jupiter, reflecting the compression by the solar wind. The curves were obtained by setting $z = 0$ in Equation 1.2 and solving for y for 1000 values of P_d between 0.001 and 1 nPa.

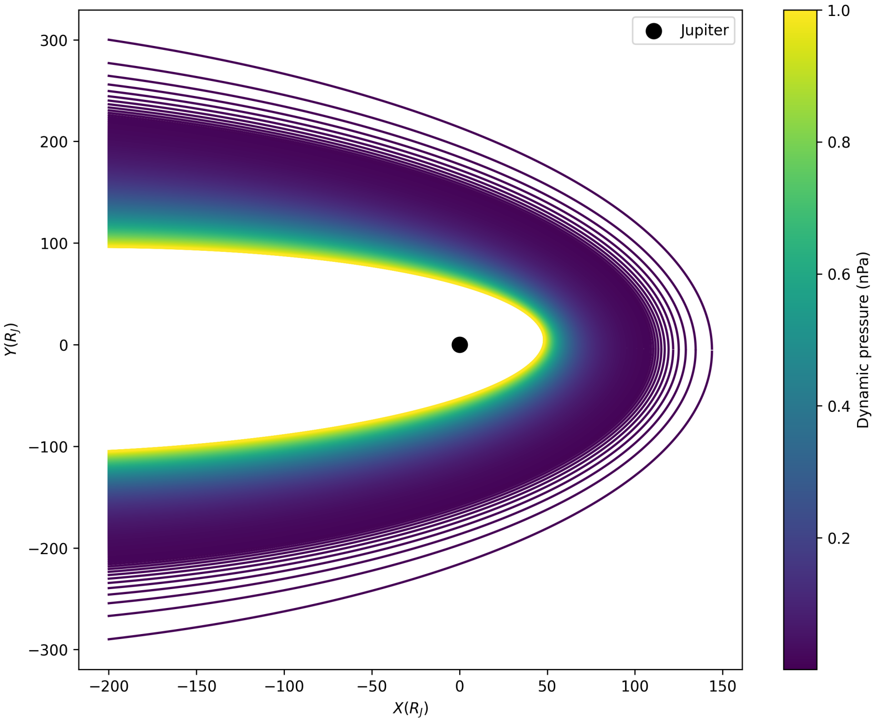

Figure 1.5: Jupiter's magnetopause from the Joy et al. model as a function of solar wind dynamic pressure (in nPa), represented in the XY plane.

In this work, Joy's model is used as a reference. We compare the normals obtained from different calculation methods to those derived directly from the Joy surface. Figure 1.6 shows the model magnetopause at $P_d = 0.1$ nPa, along with its normals at selected points in the XY plane. When referring to "Joy's normals" later in this thesis, we mean these model-derived vectors.

We interpret Joy's normals as representing an idealised, unperturbed magnetopause in a quiet state. In contrast, normals computed from in-situ magnetic field measurements will reflect perturbations such as waves on the boundary.

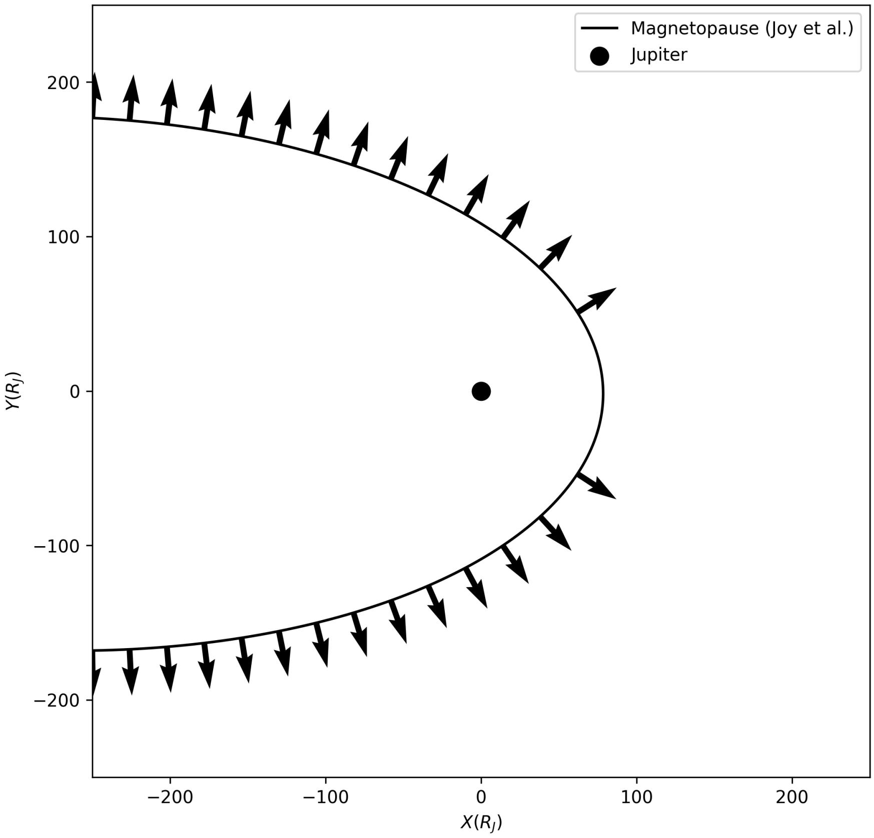

Figure 1.6: Joy's magnetopause of Jupiter at a solar wind dynamic pressure of 0.1 nPa in the XY plane, with the normals to that magnetopause plotted along the boundary.

Chapter 2

Multi-spacecraft approach

This study focuses on magnetopause observations from spacecrafts that have visited Jupiter. A multi-spacecraft approach enables the investigation of different regions of the magnetosphere, as each mission follows a unique trajectory around the planet. During approach, the spacecraft may cross both the bow shock and the magnetopause. Here, we concentrate on magnetopause crossings and the associated magnetic field variations in their immediate vicinity.

In this chapter, we review the spacecraft missions to Jupiter and the magnetometers they carried, and we describe the datasets used for the normal computation. Data subsets from the *PDS*[1] were selected to encompass the relevant crossing dates, with high-resolution measurements prioritised to improve the accuracy of the results. Indeed, high-resolution data have been shown to reduce angular errors in boundary normal determinations for specific analysis methods [Cutler et al., 2011]. The magnetic field measurements are provided in multiple reference frames, and we take an in-depth journey between the various frames. Finally, we present an example of a magnetopause crossing and compile the complete list of crossings used in this work.

2.1 Space missions

The missions of interest that have crossed Jupiter's magnetopause are Pioneer 10 and 11, Voyager 1 and 2, Ulysses, Galileo, and Juno. Their trajectories, magnetometers, datasets, and magnetopause crossings are discussed in the following sections.

2.1.1 Magnetometers

The various spacecraft carried two main types of magnetometers, introduced below.

---

[1] The Planetary Data System (PDS) is a curated archive of digital data from NASA's planetary missions, maintained to ensure long-term accessibility and usability for the scientific community.

Fluxgate magnetometers (FGM) are the primary instruments for measuring the magnetic field in the vicinity of a spacecraft. They are included in most magnetic field experiments as they present a combination of high sensitivity and accuracy, fine resolution, compact and simple design, and low noise characteristics. They consist of two coils -a drive coil and a sense coil- wound around a magnetically permeable core. A strong alternating current in the drive (exciting) coil generates an oscillating magnetic field in the core, inducing a periodic current in the sense coil. In the absence of a background magnetic field, the current in the sense coil matches that in the drive coil. When an external magnetic field is present, the core saturates preferentially in that direction, producing an imbalance between the two currents proportional to the field's strength. The difference between these currents is used to estimate the strength of the magnetic field. As FGMs are sensitive to the direction of the magnetic field, they are classified as 'vector' magnetometers [Bennett et al., 2021; Wei et al., 2021].

The basic structures of parallel and orthogonal fluxgate magnetometers are shown in Figure 2.1, where the orientation between the excitation magnetic field and probe magnetic field is different.

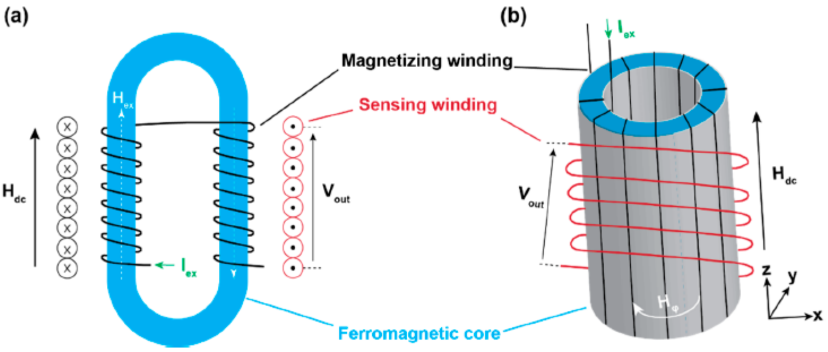

Figure 2.1: Schematic representation of a fluxgate magnetometer where (a) the excitation and probed magnetic field are parallel, (b) the excitation and probed magnetic field are orthogonal. This figure comes from Wei et al. (2021)

Helium vector magnetometers (HVM) operate on the principle of optical pumping of metastable helium. In optical pumping, incident polarised light selectively excites atoms in specific magnetic substates, which -through repeated absorption and relaxation- accumulate in states that no longer absorb that light. In a magnetic field, atomic absorption and transition probabilities between substates depend on the field's strength and direction. As a result, the efficiency of the optical pumping process varies in a way that can be measured to determine the magnetic field vector.

The HVM sensor, presented in Figure 2.2, contains a helium lamp in a collimating reflector, a circular polariser, a helium absorption cell, and an infrared detector. A collimated beam of light passes along the optic axis from the lamp, through the circular polariser and absorption cell, to the infrared detector [Smith, Connor, and Foster, 1975].

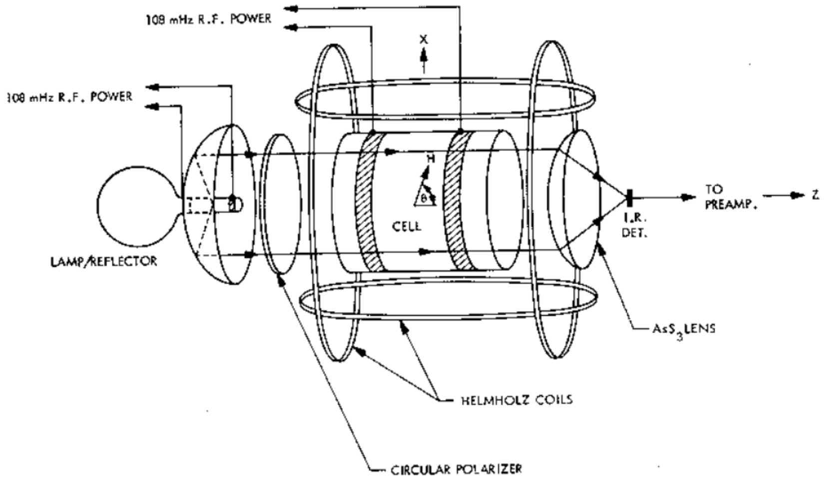

Figure 2.2: Schematic representation of a vector helium magnetometer sensor, coming from Smith, Connor, and Foster (1975). Absorption of circularly polarised light from a helium *He* lamp by a *He* cell is modulated by the vector sum of the ambient magnetic field and the rotating field generated by the coils. The resulting variations are monitored by an infrared detector. For clarity, only two of the three coil pairs are depicted.

2.1.2 Pioneer 10 and 11

Pioneer 10 was launched on 2 March 1972 to perform a flyby of Jupiter, making its closest approach to the planet on 4 December 1973. As the first mission to the outer planets, it was a landmark achievement, exceeding its planned duration and accomplishing a series of historic firsts. Pioneer 10 became the first spacecraft to travel beyond Mars, cross the asteroid belt, and follow a trajectory leading out of the solar system into interstellar space. During its encounter with Jupiter, it returned the first close-up images of the planet and conducted pioneering measurements of its atmosphere and magnetic field [NASA, 2025d].

This spacecraft was equipped with a variety of instruments, but the most interesting one for this study of Jupiter's magnetopause is its Helium Vector Magnetometer. The experiment was situated at the extremity of a 6.6-metre lightweight boom to reduce the detection of the spacecraft's internal magnetic field and enhance its equilibrium. The primary objectives of the HVM were threefold: firstly, to measure the fine structure of the interplanetary magnetic field; secondly, to map Jupiter's magnetic field; and thirdly, to collect data to evaluate the interaction between the solar wind and Jupiter's magnetosphere [NASA Planetary Data System, 2025c].

The Pioneer 10 magnetic field data is available on the *PDS* in high resolution and at one-minute sampling. To have magnetic field data covering all of the Pioneer 10 crossings, we selected both datasets and combined them. So we have one-minute data from 3 November 1973 to 29 December 1973 and high-resolution data (one-second sampling) from 24 November 1973 to 5 December 1973 [NASA Planetary Data System, 2001; NASA Planetary Data System, 2004a].

On the other hand, Pioneer 11 was launched on 5 April 1973 to study both Jupiter and Saturn. It flew by Jupiter with a perijove on 3 December 1974, taking images of the planet and making measurements of its magnetosphere, completing those of its sister mission. It was the first mission to achieve close proximity to Saturn, observing the planet, its rings and its moons [NASA, 2025e].

The measurements of the magnetic fields were conducted using both a HVM and a FGM. The HVM is the same instrument as the one embarked on Pioneer 10, while the primary function of the single-range triaxial FGM was to increase the spacecraft's upper limit measurement capacity by approximately an order of magnitude [NASA Planetary Data System, 2025d].

The Pioneer 11 spacecraft has also gathered measurements of the magnetic field of Jupiter in high resolution and with one-minute sampling. As the high-resolution data covers the entirety of the crossings for Pioneer 11, we will consider the dataset between 25 November 1974 and 14 December 1974 [NASA Planetary Data System, 2004b].

The magnetic field data measured by both spacecrafts as stored on the *PDS* is expressed in spherical coordinates in the *Jupiter System III* (1965) coordinates. In this frame, R is along the Jupiter to spacecraft line (positive away from Jupiter), ϕ is parallel to the Jovigraphic equator, and θ completes the right-handed set. Thus, B_r is the radial component, B_ϕ is the southward field component, and B_θ is the co-rotational field component. This coordinate system is well-known and is used in various magnetic field measurements.

The Pioneer 10 and 11 missions paved the way for other spacecraft to explore the outer planets, especially the Voyager missions.

2.1.3 Voyager 1 and 2

Voyager 1 was launched on 5 September 1977 to conduct flybys of Jupiter and Saturn before departing the solar system. The spacecraft reached perijove on 5 March 1979, observing Jupiter's atmosphere, magnetosphere, and moons, and notably discovering two new satellites. It then continued toward Saturn, where it conducted observations of the planet and its moons, discovering a new ring and five additional satellites. Voyager 1 subsequently became the first spacecraft to exit the heliosphere and continues to transmit data from interstellar space. It remains the most distant human-made object from Earth [NASA, 2025g].

Voyager 2 was launched ahead of its sister mission on 20 August 1977, but placed on a slower trajectory toward Jupiter, reaching perijove on 9 July 1979. Its mission objective was to carry out flybys of Jupiter, Saturn, Uranus, and Neptune before leaving the solar system. At Jupiter, Voyager 2 conducted atmospheric and magnetospheric measurements as well as detailed observations of the planet's moons. At Saturn, it studied the planet and its rings before being directed to Uranus, becoming the first human-made object to fly by the planet and discovering ten new moons, two new rings, and a tilted magnetic field. Completing its "Grand

Tour" of the giant planets, Voyager 2 made a flyby of Neptune, again a first for humanity, and discovered additional moons and rings. It remains the only spacecraft to have conducted close-up observations of all four giant planets, and, like Voyager 1, has since left the solar system and continues to return valuable data from interstellar space [NASA, 2025h].

The Voyager magnetic field experiment consists of dual low field (LFM) and high field (HFM) triaxial fluxgate magnetometers. This dual system provides great reliability, a wide dynamic range, and allows the correction of the spacecraft's internal magnetic field from the ambient field. The primary objectives of this magnetic experiment were to study the magnetic field of the planets in the outer solar system, investigate the interplanetary magnetic field, and measure the interstellar magnetic field once the spacecrafts had left the heliosphere [NASA Planetary Data System, 2025f].

The Voyager missions have measured Jupiter's magnetic field with different samplings: 1.92, 9.60, 48 seconds or one hour. These different datasets are available in different reference frames on the *PDS*: the *Jupiter System III* and the *heliographic (RTN)* coordinates.

Still in the idea to have all our crossings covered by the data and in the best sampling possible, we have chosen to use the *heliographic (RTN)* coordinates in a 1.92-second sampling. This coordinate system is defined with the radial direction R along the Sun-to-spacecraft line and positive in the anti-Sunward direction. The tangential direction is parallel to the Solar Equatorial plane (it is defined as the cross-product of the Sun's spin axis and R), and the normal direction completes the right-handed set. Thus, in these coordinates, B_R is the radial component of the magnetic field, B_T is the tangential component, and B_N is the normal component.

We use data from the Voyager 1 spacecraft between 26 February 1979 and 24 March 1979 and data from the Voyager 2 spacecraft between 20 June 1979 and 19 August 1979 [NASA Planetary Data System, 1998b; NASA Planetary Data System, 2022].

2.1.4 Ulysses

Ulysses was launched on 6 October 1990 with the primary objective of studying the inner heliosphere. On 8 February 1992, the spacecraft made its closest approach to Jupiter, taking advantage of the planet's gravitational pull to alter its trajectory and pass beneath the ecliptic plane. It then travelled beyond the solar South pole before ascending above the ecliptic and flying over the North pole. Ulysses operated for more than four times its planned mission duration, completing nearly three full orbits around the Sun. Among its many important discoveries was that the Sun's magnetic field "reverses" polarity approximately every 11 years [NASA, 2025f].

The spacecraft was equipped with a triaxial FGM and a VHM that aimed to take measurements of the interplanetary field in the inner heliosphere. In our case, it is interesting because it also measured the magnetic field at the Jovian magnetosphere [NASA Planetary Data System, 2025e].

In the case of Ulysses, we used the one-minute average dataset of the magnetic field covering dates between 25 January 1992 and 17 February 1992 [NASA Planetary Data System, 1998a]. The magnetic field is expressed in the *Jupiter System III* (1965) coordinates, which were introduced before.

2.1.5 Galileo

The Galileo mission, launched on 18 October 1989, was the first spacecraft to orbit an outer planet, with the objective of studying Jupiter, its moons, and its magnetosphere. The mission consisted of an orbiter and a probe, the latter entering Jupiter's atmosphere to measure its composition and structure. Although the spacecraft's high-gain antenna failed to deploy, modifications to the communication system enabled the mission to achieve most of its planned objectives using the lower-gain antennas. Galileo arrived at Jupiter on 7 December 1995 and completed 34 orbits, including 35 close encounters with its major moons: Europa, Callisto, Ganymede, Io, and Amalthea. Over its mission, Galileo made numerous groundbreaking discoveries, including the detection of a magnetic field around Ganymede, evidence for subsurface liquid-saltwater layers on Europa, Ganymede, and Callisto, and extensive observations of Io's volcanic activity. It was also the first spacecraft to operate long enough within a giant planet's magnetosphere to map its global structure and study its dynamics in detail [NASA, 2025b].

The Galileo Orbiter was equipped with two triaxial FGM mounted on a boom, and notably aimed to provide data to map Jupiter's magnetosphere, monitor magnetospheric dynamics, investigate the possible magnetic fields of the Galilean satellites and study the magnetosphere-ionosphere coupling [NASA Planetary Data System, 2025a].

The Galileo Jupiter magnetometer magnetospheric survey data collection is composed of different datasets corresponding to the different orbits of the spacecraft, and the sampling rate varies in time. These magnetic fields measured are available in the *IRC (Inertial Rotor Coordinates)*, *JSE (Jupiter Solar Equatorial)*, *JSO (Jupiter Solar Orbital)*, and *System III* coordinates [NASA Planetary Data System, 2024a].

We chose to use the data expressed in the *Jupiter Solar Equatorial* coordinates, where Z is along the Jovian spin axis, positive northward. X is the projection of the Sun direction into Jupiter's equatorial plane, positive Sunward, and Y completes the right-handed set and points towards dusk. This system is equivalent to Juno's *JSS (Jupiter-De-Spun-Sun)* [Bagenal and Wilson, 2016].

Some of our computations can become time-consuming, so having the lightest possible datasets makes the manipulations easier. For the Galileo spacecraft, we created a dataset of the magnetic field data only during the orbits where crossings were detected.

2.1.6 Juno

Juno is one of the most recent spacecraft used to study Jupiter; launched on 5 August 2011, it reached Jupiter after a 5-year journey on 4 July 2016. Juno was put in orbit around Jupiter to understand its origin and evolution. After observing the planet's atmosphere and magnetosphere for five years, the mission was extended in 2021 and is still observing the big planet thanks to its numerous instruments. Juno is a solar-powered spacecraft operating at a great distance from the Sun, and so it is equipped with three 9-meter-long solar panels, giving it its recognisable geometry. As for scientific results, Juno has made numerous observations: close-up pictures of Jupiter's north pole, the Jovian cyclones, the volcanoes on Io, and the auroras. The magnetic field experiment adds to what was already discovered via the previous spacecrafts to get closer to understanding Jupiter's magnetosphere field and its dynamics. It notably led to the discovery that the magnetic field is extremely intense than previously thought, more than 30 times as powerful as the one surrounding Earth [NASA, 2025c].

Juno's Magnetic Field Investigation is composed of a vector fluxgate magnetometer placed at the end of one of the three solar panels, away from the spacecraft body [NASA Planetary Data System, 2025b]. Its scientific objectives are to obtain accurate magnetic field measurements and map the planetary magnetic field [J. E. P. Connerney et al., 2017].

The magnetic field data acquired by Juno's fluxgate magnetometer is available in the *payload*, *planetocentric*, and *Sun-State* coordinates. The time resolution depends on the telemetry rate available when the data were taken, but was also downsampled to one second or sixty seconds to have more compact datasets [NASA Planetary Data System, 2024b].

In our case, we used the magnetic field data in one-second sampling and the *planetocentric* coordinates that are defined with Z along the rotation axis and positive in the direction of positive angular momentum, X is in the equatorial plane of the body in the direction of the prime meridian, and Y completes the right-handed set. The magnetic field components are thus B_X, B_Y, and B_Z.

Some of our computations can become time-consuming, so having the lightest possible datasets makes the manipulations easier. For the Juno spacecraft, we created a dataset of the magnetic field data only around the crossings: one hundred minutes before and after the crossing times.

2.2 Introduction to SPICE kernels

As seen in the previous sections, the magnetic field data are available in different coordinate systems. To compute the normals to the magnetopause in the same system for all missions, we are going to define a reference system that will be used for the entirety of this work. In the considered *Jupiter Missions* frame, the X axis is defined along the Jupiter-to-Sun line and positive Sunward, the Z axis is defined as Jupiter's spin axis, positive Northward, and the Y axis completes the right-handed frame positive towards dusk. This is a classic reference frame when studying Jupiter, and it allows an easy visualisation of the different phenomena encountered later in the work: it was, for instance, used by Joy et al. (2002) for their model definition. Similar systems were used in the case of Jupiter [Ma, P. Delamere, Schok, et al., 2022], but also for Saturn [Cutler et al., 2011], in the scope of boundary normal computations.

To transform our magnetic field data into this new reference frame and to determine the position of the seven different spacecrafts at the time of crossings, we use the SPICE (Spacecraft, Planet, Instrument, C-matrix, Events) kernels of the Navigation and Ancillary Information Facility (NAIF) [NASA, 2025i]. Indeed, the NAIF offers a range of kernels that give scientists access to a wide range of geometry information, from the position of the spacecraft relative to a planet of choice to the orientation of the different instruments on said spacecraft. They provide precision observation geometry practical for planetary science.

For our work, we used predefined SPICE SPK kernels (location of target body as a function of time) for our different missions, which were notably employed to plot the trajectories in Figure 2.3. We also used FK kernels (frame of reference) for transforming the data from the reference frames specific to the mission to the *Jupiter Missions* frame defined earlier. The complete list of used kernels can be found in Appendix A.

To better visualise the different reference frames used by the considered spacecrafts and how they relate to each other, we used the document by Bagenal and Wilson (2016). It shows the definitions of Juno's frame, their SPICE names, and how they can be associated with other spacecrafts.

The SPICE kernels are an incredibly complete tool that offers a wide range of applications when using data from spatial observatories. In this work, we only scratched the surface of the possibilities provided by the Navigation and Ancillary Information Facility.

2.3 Trajectories around Jupiter

The various spacecrafts have described a multitude of different trajectories around Jupiter, exploring different parts of the magnetosphere. A representation of the different trajectories of the multiple missions around Jupiter can be found in Figure 2.3. The courses of the spacecrafts are plotted in the XY plane of the *Jupiter Missions* frame, defined in the previous section.

The Voyager missions approached Jupiter on the dawn side of its magnetosphere, arriving from the direction of the inner solar system. Both spacecrafts entered and exited the magnetosphere on the dawn side, remaining at low latitudes throughout their trajectories before continuing toward the outer solar system.

The Pioneer missions followed a broadly similar approach, also arriving from the inner solar system on the dawn side. After perijove, Pioneer 10 continued toward the outer solar system along a trajectory comparable to that of the Voyagers. In contrast, Pioneer 11 reversed course after closest approach, exiting the Jovian magnetosphere in the Sun's direction. Unlike the Voyagers, the Pioneers eventually departed the magnetosphere at higher latitudes. Ulysses also approached

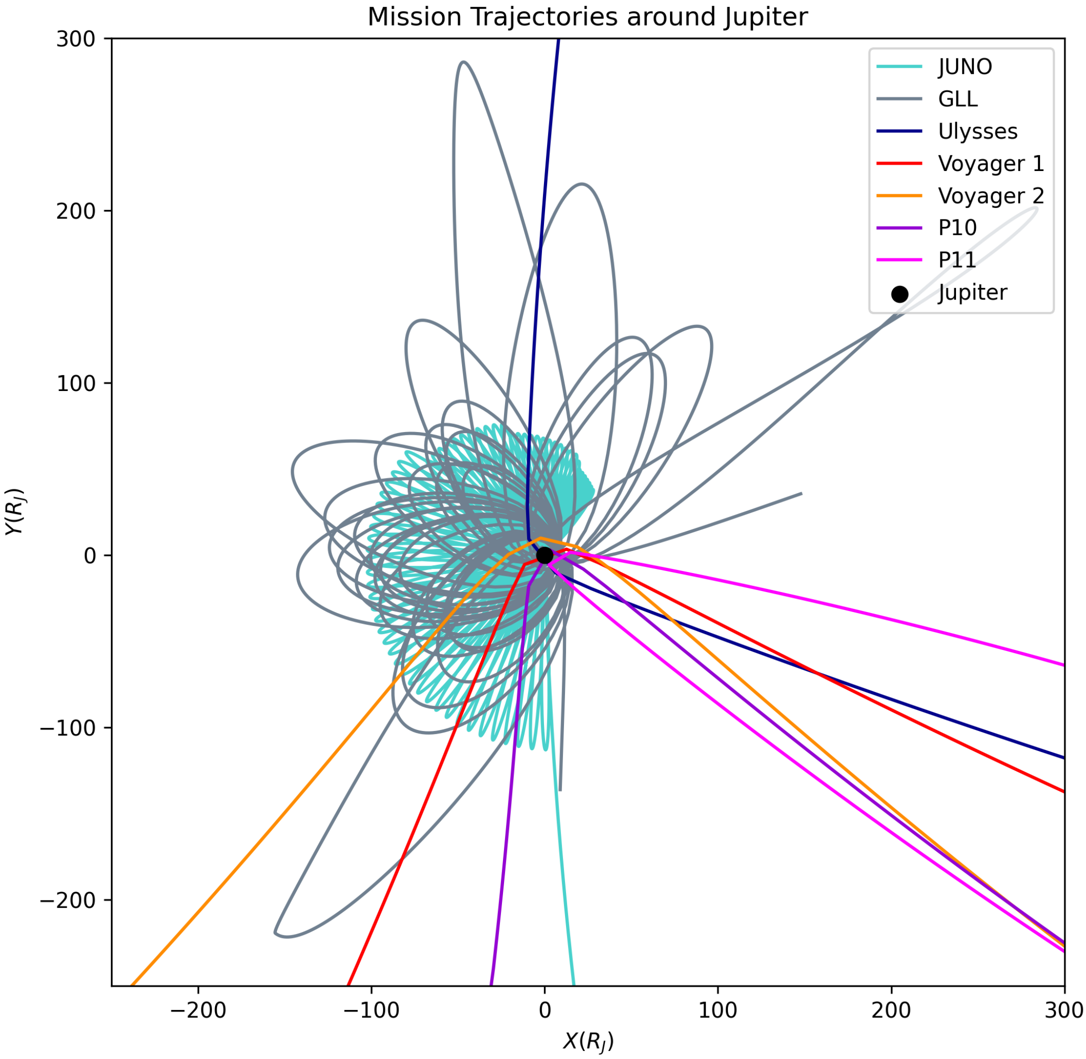

Figure 2.3: Trajectories of the different spacecrafts around Jupiter in the XY plane of the *Jupiter Missions* frame. Juno and Galileo were put in orbit around Jupiter, while Pioneer 10 and 11, Voyager 1 and 2, and Ulysses made flybys of the planet.

from the same general direction but, after perijove, exited the magnetosphere on the dusk side. Its trajectory carried it vertically out of the system, exiting the magnetosphere on its South boundary.

Whereas Pioneer 10, Pioneer 11, Voyager 1, Voyager 2, and Ulysses performed flybys of Jupiter, the Galileo and Juno missions were placed into orbit around the planet.

Galileo arrived on the dawn side of the magnetosphere and later concentrated its observations on the dusk side, where it crossed the magnetopause multiple times. Throughout its orbital mission, it remained close to the equatorial plane.

In contrast, Juno was placed in a highly elliptical, polar orbit designed to enable close-in measurements of Jupiter while avoiding the regions of most intense radiation [Bolton et al., 2017]. Its orbits gradually migrate from the dawn to the dusk side. Although this shift is not apparent in Figure 2.3, it is important to note that, unlike Galileo, which remained near the equatorial plane, Juno's magnetopause crossings occur predominantly at high latitudes on the dusk side.

2.4 Crossings

We now focus on the transitions of the spacecrafts between the magnetosheath and the magnetosphere, and establish a list of crossings to be used in the normal computation. Magnetopause crossings can occur in two directions, referred to as **in** and **out**. An **in** crossing occurs when the spacecraft moves from the magnetosheath into the magnetosphere, while an **out** crossing occurs when it exits the magnetosphere into the magnetosheath. For our analysis, the key information is the precise date and time of each crossing, along with its classification as either **in** or **out**.

A magnetopause crossing is defined as a short interval during which the magnetic field transitions from magnetosphere-like to magnetosheath-like, or vice versa. These events can be identified through changes in magnetic field measurements, particle populations, wave observations, and other indicators. The suite of instruments onboard spacecraft exploring Jupiter's environment enables the detection of such crossings by comparing multiple characteristics of the two regions [Ma, P. Delamere, Schok, et al., 2022]:

- The magnetic field is smoother in the magnetosphere than in the magnetosheath.
- The magnetosheath has a high flux of keV ion particles, while the magnetosphere has a high electron flux in the keV range.
- As the He is from solar wind origin, and internal sources of magnetospheric ions produce the O and S, the magnetosphere has a high flux of O and S while the magnetosheath has a high flux of He.

Later, we will use magnetic field data from the previously introduced missions to compute the magnetopause normals at the crossing points. It is therefore useful to highlight the changes in the magnetic field components during a typical crossing, as illustrated in Figure 2.4. The magnetic field components —B_X, B_Y, and B_Z—are defined along the axes of the Jupiter Missions reference frame.

In the example shown, Juno crossed from the magnetosphere into the magnetosheath on 24 July 2016 at 18:47:00. The change in the magnetic field is clearly visible: B_{total} decreases and the B_Z component becomes positive after the crossing. Additionally, the magnetic field is smoother within the magnetosphere, whereas the components exhibit larger oscillations in the magnetosheath. These changes in magnetic field characteristics will be used to compute the normal at the crossing location.

In this work, we use lists from other authors who observed the difference in

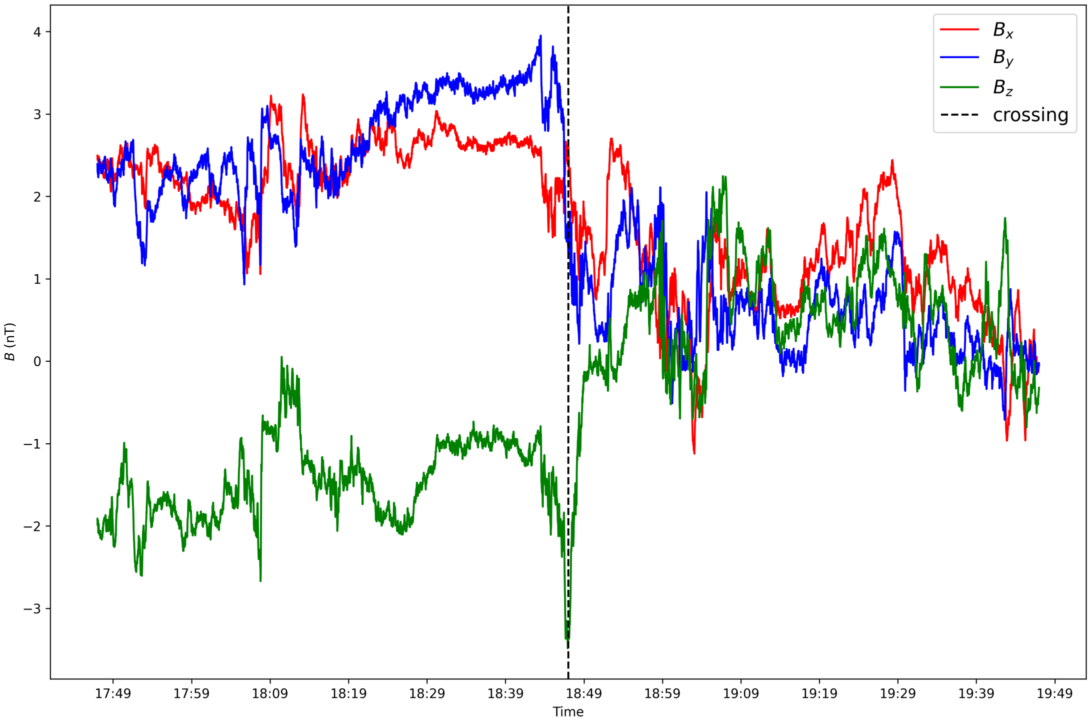

Figure 2.4: Magnetic field components in the *Jupiter Missions* frame during the magnetopause **out** crossing by Juno on 24 July 2016 at 18:47:00. A change in magnetic field is observable at the crossing, and the magnetic field components are smoother in the magnetosphere than in the magnetosheath.

properties of the magnetosphere and magnetosheath to identify the **in** and **out** crossings of Jupiter's magnetopause.

We work on the basis of the list furnished by Fran Bagenal (personal communication), which combines bow shock and magnetopause crossings. This list is a combination of the ones established by Collier et al. (2020), C. K. Louis et al. (2023), R. W. Ebert et al. (2017), and Ranquist et al. (2019). It gives useful information such as the date and time of the crossing, its position in the *JSS*[2] reference frame, the spacecraft that measured it and from which of the above list come this crossing.

The key information missing from this list is whether the crossing is towards the magnetosphere (**in**) or the magnetosheath (**out**). We combine Bagenal's list with others from the literature to have all the needed data. For the Voyager spacecrafts, we use the list from Lepping, Silverstein, and Ness (1981), for the Pioneer spacecrafts, we use the list from Intriligator and Wolfe (1976), for Ulysses, we use the list from Margaret Kivelson (personal communication), and for Galileo, we use the supporting information of Collier et al. (2020).

In the case of the Juno spacecraft, we do not have access to the list of crossings created by R. W. Ebert et al. (2017), so we put aside 266 crossings that Juno

---

[2] The *Jupiter-De-Spun-Sun* reference frame is defined with the Z axis along Jupiter's spin axis, the Y axis as the cross-product between the Z axis and the unit vector from Jupiter to the Sun and X completes the right-handed set [Bagenal and Wilson, 2016].

made on the dusk side of the magnetopause as we do not know their direction (**in** or **out**). However, the orbits of Juno made during this period (2021-2023) are at high latitudes, and here we concentrate on lower latitudes crossings. For the other Juno crossings, we use the list from C. K. Louis et al. (2023) that contains the **in/out** information.

In the end, our list contains 381 crossings: 101 on the dusk side and 280 on the dawn side. Figure 2.5 shows the positions of Jupiter's magnetopause crossings associated with the different missions. We can already say that this disparity between dawn and dusk sides will have an impact on the comparison between both sides later in the work.

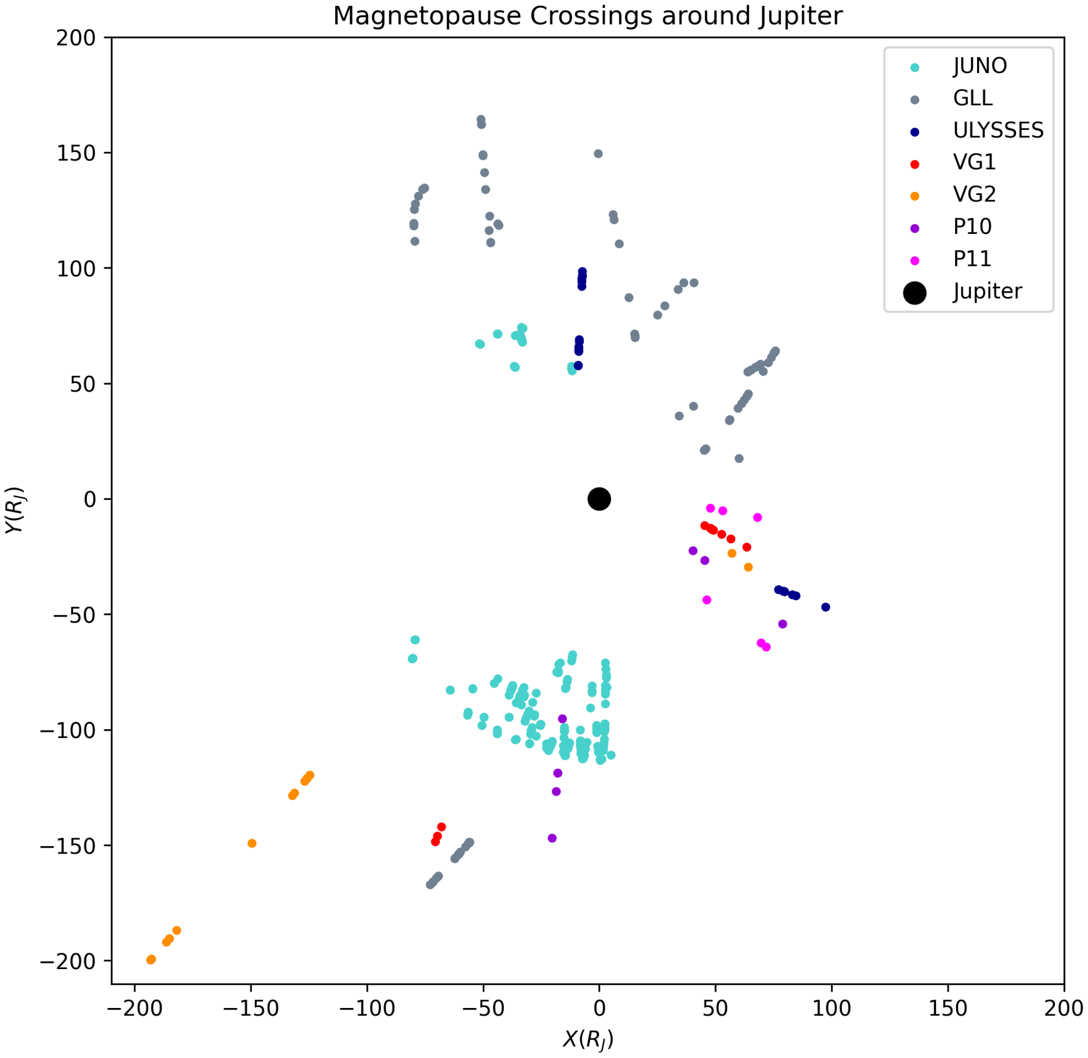

Figure 2.5: Positions of the magnetopause crossings of the different spacecrafts in the XY plane. This figure highlights the disparity between the number of crossings on the dawn and dusk sides of the magnetosphere.

It is important to note that we do not use the entirety of the 381 magnetopause crossings for our computation: we do not have the direction for 4 of them, and 24 of them are either not covered by data or the data is insufficient. In the end, our crossing list contains 357 crossings: 85 on the dusk side and 272 on the dawn side. The complete list of the 357 crossings can be found in the Appendix B, which contains the name of the spacecraft detecting the crossing, and the precise date, time, direction, and position in the *Jupiter Missions* frame of the magnetopause crossing.

Chapter 3

Normal computation

3.1 Methods

The core of this master's thesis is to determine the normal to Jupiter's magnetopause at each crossing point. To achieve this, five distinct methodologies are employed, enabling us to estimate the robustness of the computed normal and also to determine which methods are more effective in our case. We were inspired by Ma, P. Delamere, Schok, et al. (2022), who employed four boundary analysis methods and compared the resulting normals. Masters et al. (2009) also used the two different techniques to obtain the normal to Saturn's magnetopause, with one in common with Ma, P. Delamere, Schok, et al. (2022). In this section, we introduce the five different methods used in these articles, as we will use them to compute the normals to the magnetopause crossings from our list.

3.1.1 The Minimum Variance Analysis method

The minimum variance analysis (MVA) is the most widely employed method for computing the normal to the magnetopause. A detailed description on how to calculate the vector normal to the magnetopause using magnetic field vectors was exposed by Sonnerup and Cahill Jr (1967). As suggested by its name, the MVA identifies the direction of minimum variance as the normal vector by minimising the variance

$$\sigma^2 = \frac{1}{N} \sum (\mathbf{B^i} \cdot \mathbf{n} - \bar{\mathbf{B}} \cdot \mathbf{n})^2, \tag{3.1}$$

where $\bar{\mathbf{B}} = \frac{1}{N} \sum_{i=1}^{N} \mathbf{B^i}$ and under the constraint $|\mathbf{n}|^2 = 1$.

The minimisation of σ^2 is equivalent to finding the smallest eigenvalue of the covariant matrix defined as

$$M_{\alpha\beta} = (\overline{B_\alpha B_\beta} - \bar{B}_\alpha \bar{B}_\beta), \tag{3.2}$$

with $\alpha, \beta = 1, 2, 3$. In this expression, B_α and B_β are the Cartesian components of the magnetic field vectors, while the bar indicates the mean over all measurements used in the calculation. The normal vector is the eigenvector corresponding to the smallest eigenvalue. It can be noted that the greater the ratio of the intermediate to the smallest eigenvalue is, the better the normal vector obtained by the MVA is defined.

3.1.2 The Siscoe method

As the MVA, the Siscoe method (SIS) is another commonly used method for computing boundary normals, identifying the normal vector as the smallest average field amplitude. Siscoe et al. (1968) exposes that the vectors tend to rotate from a pre-event to a post-event direction when crossing a simple discontinuity[1]. If $\mathbf{B}^k (k = 1, 2, ...)$ are the magnetic field vectors of the crossing event and $\mathbf{n}$ is the normal to the rotation plane, it is defined as the value that minimises

$$\sum_k (\mathbf{B^k} \cdot \mathbf{n})^2 = s^2, \tag{3.3}$$

subject to the constraint $\mathbf{n}^2 = 1$.

If instead we choose to minimise $(s^2 - \lambda n^2)$, where λ is a Lagrange multiplier, we obtain

$$\sum_j (T_{ij} - \lambda \delta_{ij}) n_j = 0, \quad \text{with} \quad T_{ij} = \sum_k B_i^k B_j^k. \tag{3.4}$$

These are the equations that allow us to determine the components of $\mathbf{n}$. In finding the eigenvalues and eigenvectors of T_{ij}, we can identify the normal as the vector corresponding to the smallest eigenvalue. The bigger the ratio of the intermediate to the smallest eigenvalue is, the better the normal vector obtained by the Siscoe method is defined.

3.1.3 The BMBS method

The BMBS method was first introduced in the article by Xuanye Ma et al. (2016) as an MVA-Siscoe hybrid method. We can define the N direction as the normal direction pointing outwards of the magnetosphere, L as the direction perpendicular to the normal and pointing to the north and M as the direction perpendicular to the normal and oriented tailward. These L, M, N directions correspond to the eigenvectors related to the maximum, intermediate and minimum eigenvalues of the MVA and SIS methods. The BMBS method determines the L direction via the MVA method, before finding the M and N directions in the MN plane through the Siscoe method.

3.1.4 The constraint method

As presented by Sonnerup and Cahill Jr (1968), the constraint method (CSTR) is similar to the MVA in defining the variance as in Equation 3.1. However, the minimisation of σ^2 is here subject to two constraints instead of one: $\mathbf{n}^2 = 1$ and $\bar{\mathbf{B}} \cdot \mathbf{n} = 0$. Indeed, this method is adequate for tangential discontinuities, where the normal field component should be zero.

---

[1] Simple discontinuities are characterised by a direct change from one vector field to the other.

From there, the minimisation is simplified by choosing a coordinate system such that the covariant matrix $M_{\alpha\beta}$ in Equation 3.2 is diagonal. This process is then performed using Lagrange multipliers and gives the normal component along the jth principal axis of $M_{\alpha\beta}$ as

$$n_j = \Gamma \bar{B}_j / (\lambda_j - \Lambda), \tag{3.5}$$

with $j = 1, 2, 3$. In this expression, $\bar{B}_j$ is the component of $\bar{\mathbf{B}}$ along the same j axis, while the normalisation factor Γ is given by

$$\Gamma^2 = \left[\sum_{j=1}^{3} (\bar{B}_j{}^2 / (\lambda_j - \Lambda)^2) \right]^{-1}. \tag{3.6}$$

The quantity Λ is equal to the variance σ^2 when the direction $\mathbf{n}$ is given by n_j, defined in Equation 3.5. Hence, Λ is the smallest root of the equation

$$\Lambda^2 \left(\bar{B}_1{}^2 + \bar{B}_2{}^2 + \bar{B}_3{}^2 \right) - \Lambda \left((\lambda_2 + \lambda_3) \bar{B}_1{}^2 + (\lambda_1 + \lambda_3) \bar{B}_2{}^2 + (\lambda_1 + \lambda_2) \bar{B}_3{}^2 \right) \\ + \left(\lambda_2 \lambda_3 \bar{B}_1{}^2 + \lambda_1 \lambda_3 \bar{B}_2{}^2 + \lambda_2 \lambda_1 \bar{B}_3{}^2 \right) = 0 \tag{3.7}$$

Therefore, the constraint method consists of computing the covariance matrix before determining its eigenvalues and eigenvectors. Then, the average magnetic field $\bar{\mathbf{B}}$ is projected in the principal axis of $M_{\alpha\beta}$ and the Equation 3.7 is resolved in Λ. When the corresponding minimum root is obtained, one can find the quantity Γ from Equation 3.6, and Equation 3.5 can be used to find the normal component in the principal axis of the covariant matrix. Finally, by projecting these normals in the initial frame, one can obtain the desired normal, which is best defined the greater the ratio between the largest and smallest roots Λ is.

3.1.5 The Tangential Discontinuity Analysis method

The tangential discontinuity analysis (TDA), also called the cross-product method, is appropriate in the case of tangential discontinuities[2] between the planetary and interplanetary magnetic field. This technique was, for example, applied by Adam Masters et al. (2012) to Saturn's magnetopause current layer crossings. In this method, average magnetic fields are determined at a few-minute intervals on both sides of the crossing, and the normal direction is given by the vector product of these two average fields.

3.2 Windows

As previously outlined, a range of different techniques is employed to calculate the normal to the magnetopause of Jupiter. This will facilitate a comparative analysis of the efficiency of the various methods, enabling the identification of those that demonstrate superior performance in specific contexts.

---

[2] Tangential discontinuities are characterised by a zero normal field component.

In order to compute a normal, the idea is to apply the methods to the crossing, over a specific range of data. One of the crucial questions of this master's thesis is to decide on which window of data to apply these methods to. We can use fixed windows, but there is the problem of the arbitrary choice of the fixed time interval. We can also explore an optimised solution, where the chosen time interval is different at each crossing.

In this section, we discuss the impact of the window choice on the normal obtained by the different methods, and the possibility of using fixed or optimised windows for the calculation.

3.2.1 Impact of the window's size

We first examine the impact of the window's size on the computation of the normal via the different methods. This is done by increasing the size of the window, from 1 to 30 minutes on both sides of the crossing. Then we measure the angle between the normal obtained by the method and the normal determined by the model of Joy et al. (2002).

This experiment was done for the crossings detected by Juno, and similar figures were obtained in all cases. Figure 3.1 shows the angle in the XY plane between the model and the method normals for all five methods (called "methods" normals in the rest of the text) for the crossing on 24 July 2016. We chose to test sizes going from 1 to 30 minutes on both sides of the crossing, creating windows of sizes going from 2 to 60 minutes.

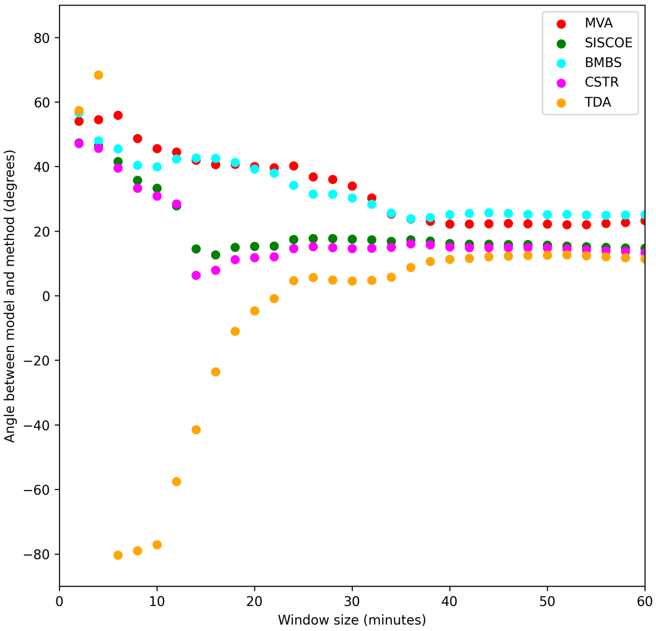

Figure 3.1: Angles (in degrees) between the model and method normals in function of the size of the window of computation (in minutes) for the 24 July 2016 crossing. The various methods give different normals, which are dependent on the size of the time window.

A few observations can be made from this figure. First, the different methods give different normals as five different outlines are observed on the figure. Secondly, the size of the chosen window affects the normal computed by our methods, but this variation is different for the five methods. For this crossing, the TDA is the most affected by the increase in the window's size. However, this difference between the normals from the different methods tends to decrease starting from the 10-minute mark, and this is observed for most of the crossings. Thirdly, the CSTR and SIS methods agree with each other, while the same can be said for the BMBS and MVA.

This analysis tells us that we have to be mindful of the choice of our computation windows, as it has a considerable impact on the obtained normals. This problem is discussed in the following points.

3.2.2 Fixed windows

The first possibility that can be explored for the choice of the computation windows is the arbitrary case. We observed that in reference articles computing normals to the magnetopause, fixed windows tend to be chosen and applied for all methods and crossings to facilitate a systematic comparison. In Ma, P. Delamere, Schok, et al. (2022), the authors chose fixed 10 and 20-minute windows, while Adam Masters et al. (2012) used small intervals of a few minutes for the computation of the MVA and TDA.

In our case, to have a point of comparison with the results obtained by the optimised methods explained below, we chose to compute the normals on arbitrary time windows of 10 minutes before and after the crossing (i.e. 20-minute windows).

The advantages of this option are the short computation time, easy reproducibility, and systematic comparison between methods and crossings. Conversely, the main drawbacks are the purely arbitrary time interval choice and the fact that these time windows are not necessarily the most adapted for the different crossings and methods.

3.2.3 Optimised windows

The other option for the choice of the time windows is the optimised one. In this section, we will identify the conditions for the best-defined normal for each method and then select the corresponding time windows. Indeed, we will individually move the lower and upper bounds of a test interval and then compute the normal and evaluate the condition. In light of the impact of the window's size on the normal computation, where we saw that the tested methods give unstable and different results under 10-minute windows, we chose to impose the optimised computation between 10 and 60-minute windows. Let us now tackle the definition of the conditions for the different methods.

We first focus on the Minimum Variance Analysis. As explained before, the ratio of the intermediate to the smallest eigenvalue evaluates the extent to which the normal is well-defined. Thus, to obtain the best possible normal via this method, we have to maximise this ratio. The optimised version of the MVA computes the normal on increasingly large windows and keeps the one providing the maximum ratio as the best normal. Of course, the window lengths obtained will be different for all crossings.

The Siscoe method evaluates the definition of the normal as the MVA method, i.e. it maximises the ratio of the intermediate to the smallest eigenvalue. On the other hand, the BMBS technique finds the L direction via the MVA and then computes the M and N directions via the SIS. Thus, the best defined normal can be evaluated using the Siscoe method.

As explained above, the Constraint method gives a well-defined normal when the ratio between the largest and smallest roots Λ from Equation 3.7 is the greatest. Hence, in the optimised version of the method, we maximise this ratio and keep the normal and window associated with it.

Finally, we can consider how to obtain the best normal by the cross-product method (or TDA). We want the mean magnetic field to be computed on a range of data representative of the behaviour before and after the crossing. This requires the search for a time interval (before and after the crossing) where the variance of the magnetic field is relatively stable (authorising a variation of 10%) before computing the TDA on this window.

The main benefits of this option are that the obtained normal is assured to be the best possible one, and is also totally justified by the conditions of optimisation. The drawback is that the optimised windows can be vastly different, which limits the systematic comparison between methods.

3.2.4 Comparison

In this section, we compare the arbitrary 20-minute window to the optimised ones obtained for a single crossing, while the same can, of course, be done for all the crossings. In Figure 3.2, one can observe the crossing of the 24 July 2016 that was already discussed earlier, where the colour lines are the lower and upper bounds of the optimised windows, and the grey lines are the ones from the arbitrary 20-minute case.

This figure displays the position of the lower and upper bounds of the time intervals linked to the different methods, going from the crossing towards the exterior. As can be observed, the MVA and TDA are close to the 10-minute window chosen as the minimum one for the optimised computation. Then, we have the arbitrary bounds of the 20-minute window. The limits of the Constraint and Siscoe methods are superposed. The lower and upper bounds of the BMBS, CSTR and SIS methods are not symmetric compared to the crossing point, as the lower and upper limits are moved independently during the optimisation. We can point out that such figures can be drawn for the entirety of the crossing list, and give different time interval boundaries for the various methods.

Now that we have introduced the different techniques that were used on magnetic field data surrounding the magnetopause crossings detected by the different spacecrafts, the results obtained via the use of these methods and windows will be explored in the next chapter.

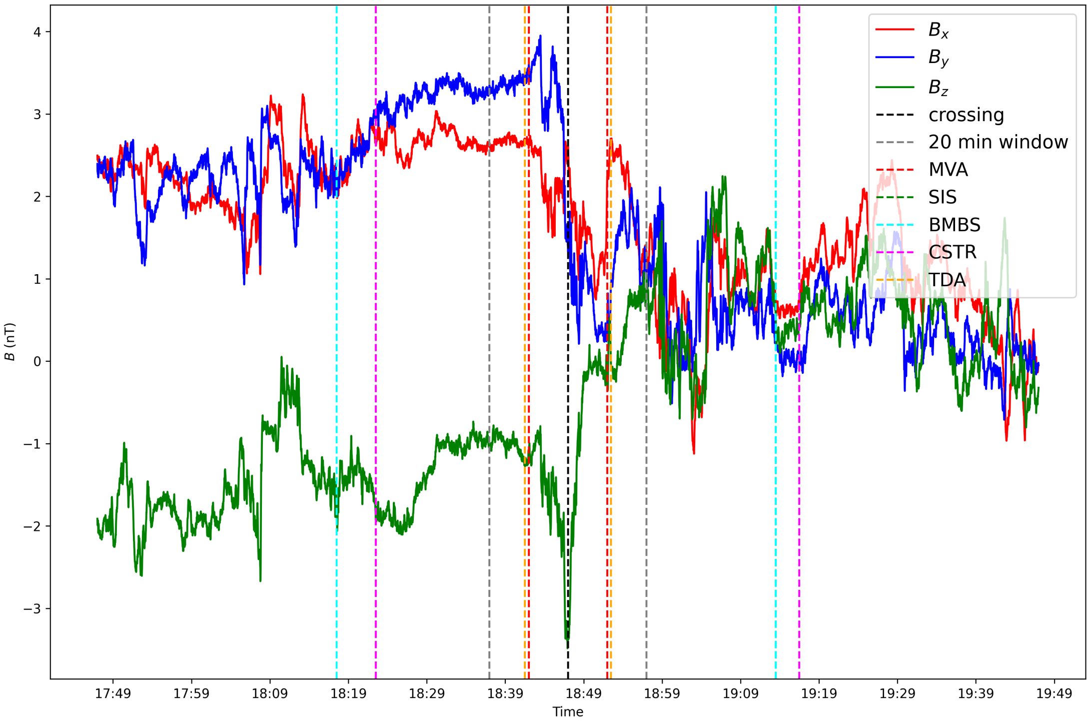

Figure 3.2: Jupiter's magnetopause **out** crossing by Juno on 24 July 2016 at 18:47:00, with the representation of the windows taken by the optimised and fixed methods. The smallest windows are the ones for the TDA and MVA methods, then the fixed window. The SIS lines are not visible as they are under the CSTR one. The CSTR and BMBS windows are not symmetric, as the lower and upper bounds are moved independently for the optimised windows.

Chapter 4

Results

In this chapter, we present the global results of our analysis. For each crossing point, the magnetopause normal vectors were computed using five different methods and two window-size options. In the first section, we examine the normals derived from the Galileo and Juno missions in detail. We then analyse the statistical properties of the normals obtained from all crossings across all spacecrafts.

4.1 Normals

We employed five methods to calculate the normal to the magnetopause at each crossing from our list, distinguishing between the **in** and **out** crossings. The resulting vectors were plotted in the XY, XZ, and YZ plane of the *Jupiter Missions* frame with X towards the Sun, Z towards the North of Jupiter and Y completing the right-handed frame. As this computation was done for each mission and each crossing, it represents a large number of plots, and not all of them will be shown here. We are going to focus on some of them, and the rest of the plotted normals can be found in Appendix C.

4.1.1 Orientation of the normal vectors

Figure 4.1a represents the results from the normal computation for the Pioneer missions on the optimised windows. We can observe the trajectories of the two spacecrafts around Jupiter, between November 1973 and January 1974 for Pioneer 10, and between November 1974 and December 1974 for Pioneer 11. The normals obtained by the five methods were plotted at the crossing points in different colours, and we focus here on the orientation of the normals regardless of the direction of the crossing (**in** or **out**).

The normals are represented in the figures as vectors, but what we computed is the normal direction, which means that they can be represented oriented to either side. We want the normals to be oriented away from Jupiter, as it is inherently how we consider a normal vector to a magnetopause surface. To modify the orientation of the vectors, we tried two different modifications to the plotted normals, which are shown in Figure 4.1.

First, we decided to modify the orientation of all the normals, including those obtained by the methods, as well as the normal from Joy's model. We modified their orientation through the position of the Sun, flipping the ones that were directed towards the negative X. We obtained the normals plotted in Figure 4.1b, where we can see that they are all oriented towards the right of the plot, towards the Sun.

The second modification was motivated by the position of Joy's normal vector. As we can see in the plot of the normal oriented via the position of the Sun, some normals obtained through the methods are at angles greater than 90 degrees from the model normal. For those vectors, we flipped them so all the normals plotted are within 90 degrees (left or right) of Joy's normal. This final representation of the normal vectors to the magnetopause at the crossing points is shown in Figure 4.1c.

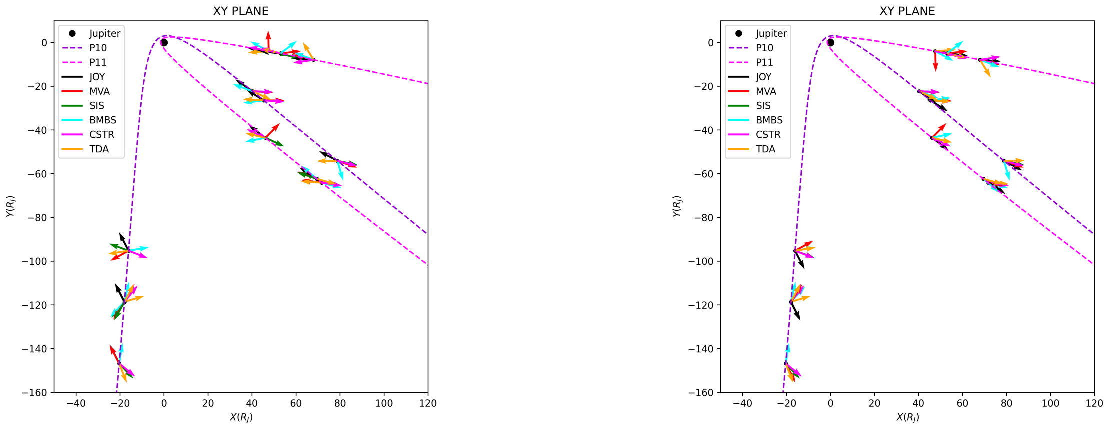

(a) Not modified.

(b) Oriented via Sun.

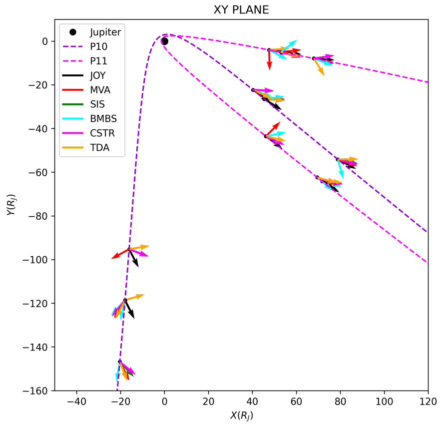

(c) Oriented via Joy.

Figure 4.1: Different possible orientations of the normals due to modifications applied to the vectors, represented in the XY plane. The trajectories of the Pioneers around Jupiter are plotted in dotted lines, and the normals computed via each method are represented in different colours. The vectors' orientations are shown in (a) the initial case, (b) oriented via the position of the Sun, and (c) oriented via the position of Joy's vector.

The normals will be oriented via the position of the model normal by Joy in the rest of the work, and all the figures and computations will be done with these oriented normals.

4.1.2 Normals on the dawn side

As Juno is in orbit around Jupiter and started on the dawn side, it is the spacecraft that has made the most crossings on that side of Jupiter's magnetopause. We can represent the trajectory of Juno in the XY, XZ, and YZ planes between July 2016 and June 2024, which allows us to visualise its movement around the planet. This was done in Figure 4.2, where we can see the normals found with the different methods plotted on the magnetopause crossings. As we discussed just above, the vectors were obtained by the optimised methods and oriented thanks to Joy's normal.

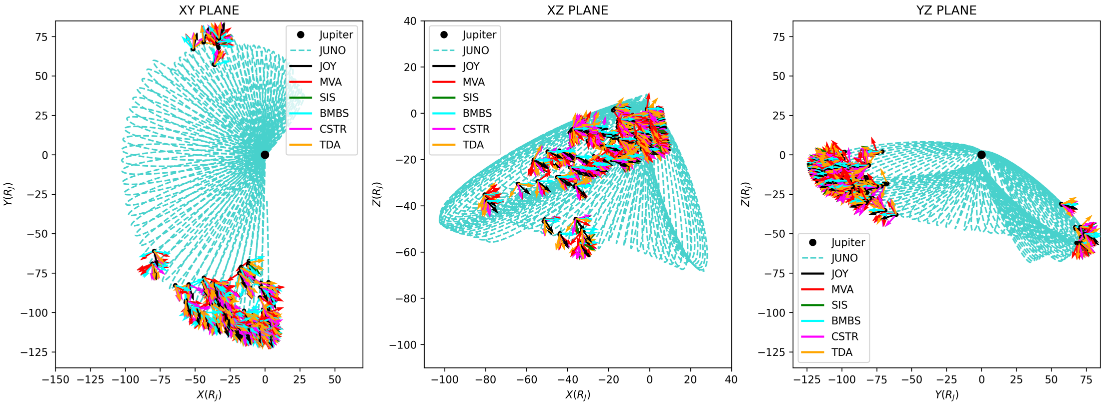

Figure 4.2: Trajectory of Juno in the XY, XZ, and YZ planes with the model and methods normals computed at the different crossings in different colours.

The distribution of the colour vectors around the black arrows representing the model can give the first impression that the different methods give incoherent results. However, it is essential to note that successive crossings can give normals directed in very different directions - this will be discussed in the following chapters - but appear to be from the same crossing on figures representing whole trajectories. These plots are shown here to illustrate the results obtained by the five possible normal computations, but the comparison between the methods will be done later in this work.

After looking at the plots of all methods, which allow us to see the distribution of the vectors around the model normal, we can also examine the normals while differentiating the **in** and **out** crossings computed via the different methods. As an example, Figure 4.3 shows the vectors obtained via the MVA and SIS methods, plotted on the trajectory of Juno in the XY plane. These figures allow us to see that the normals at the **in** and **out** crossings can have wildly different orientations, and give this impression of distribution in the previous figures. However, these plots also show that different approaches can provide different results: one can look at the normals plotted around $X = -75R_J$ and note that the MVA and SIS vectors are oriented differently. The difference between the results given by the various methods will be studied and discussed in the following chapters.

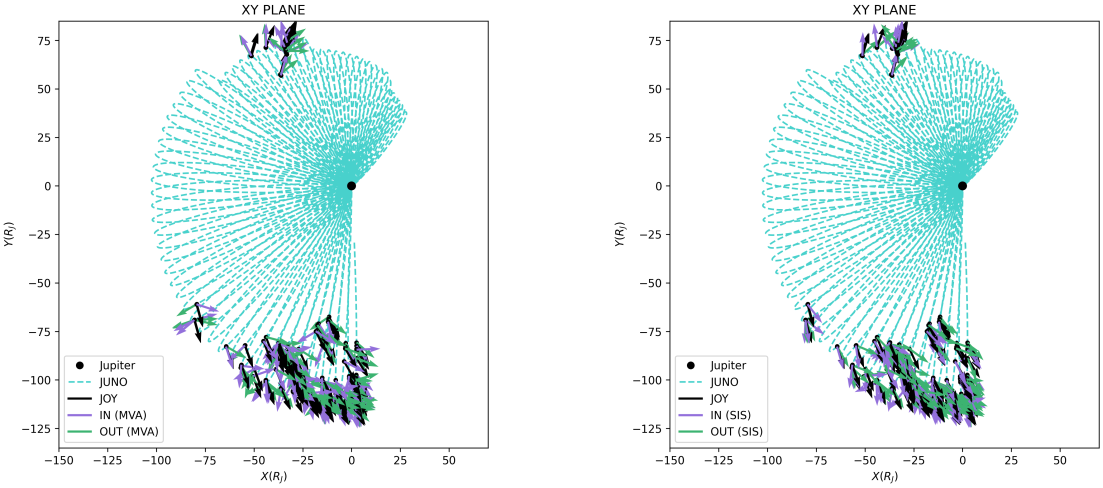

(a) Computed via MVA.

(b) Computed via SIS.

Figure 4.3: Comparison of the normals computed by the MVA and the SIS methods, plotted in the XY plane on Juno's trajectory. The colours differentiate the direction of crossings: **in** towards the magnetosphere and **out** towards the magnetosheath.

4.1.3 Normals on the dusk side

In all missions, Galileo is the spacecraft that has crossed the magnetopause the most on the dusk side (for our crossing list, excluding a significant portion of Juno's crossings on the dusk side). Hence, we consider its crossings to represent the normals computed on the dusk side of the magnetopause. We represent its trajectory in the XY, XZ, and YZ planes between May 1996 and November 2002, which allows us to visualise its movement around the planet. This can be observed in Figure 4.4, where the normals at the crossing points by the different methods were obtained by the optimised option and oriented via Joy's normal. The remarks on the distribution of the vectors around the model normal are the same as for the Juno spacecraft; no conclusion on the coherence of the results obtained by the methods can be drawn from such plots, which are there for an illustration purpose.

Some interesting comments can be made on the trajectory of Galileo compared to the trajectory of the Juno spacecraft. If we focus on the XZ plane of the figure, we see that Galileo stays close to the equator during its orbits around Jupiter. This is not the case for Juno, which goes to high latitudes on the dusk side of the magnetosphere. Furthermore, in considering the XY planes, we observe that Juno reaches maximum distances of around -125 R_J in the Y direction during its orbit, on the dawn side of the magnetosphere. On the other hand, Galileo reaches maximum distances of around 280 R_J in the Y direction during its orbit, on the dusk side of the magnetosphere. This difference in coverage will have to be taken

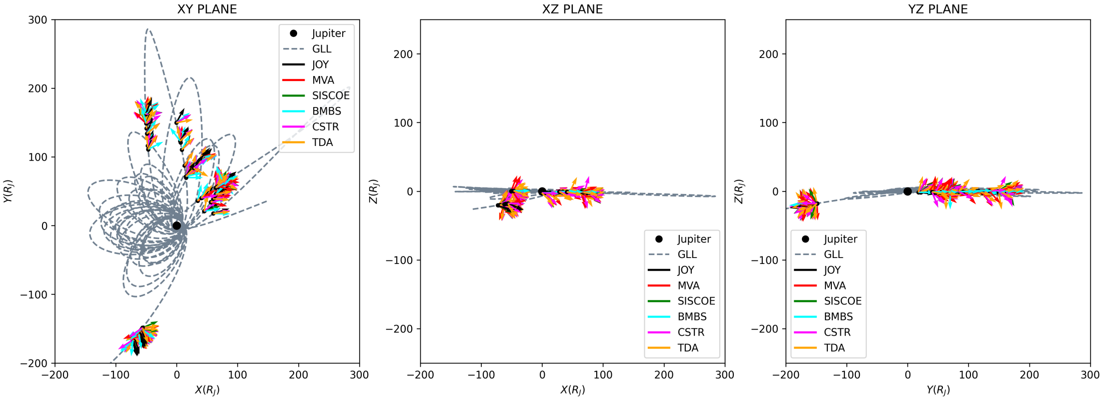

Figure 4.4: Trajectory of Galileo in the XY, XZ, and YZ planes with the model and methods normals computed at the different crossings in different colours.

into consideration for the difference in dynamic pressure considered later in the statistical results.

As done for Juno, we can focus on the normals computed by two methods, and differentiate the **in** and **out** crossings. Figure 4.5 compares the vectors obtained by the SIS and CSTR methods, plotted on Galileo's trajectory in the XY plane. These figures allow us once again to see that the normals at the **in** and **out** can have wildly different orientations, and give this impression of a wide distribution in the previous figures. The comparison of both plots shows a remarkable similarity between the vector normals obtained by the Siscoe and Constraint methods, contrary to what was noted for the SIS and MVA. These observations will be investigated in the rest of this work.

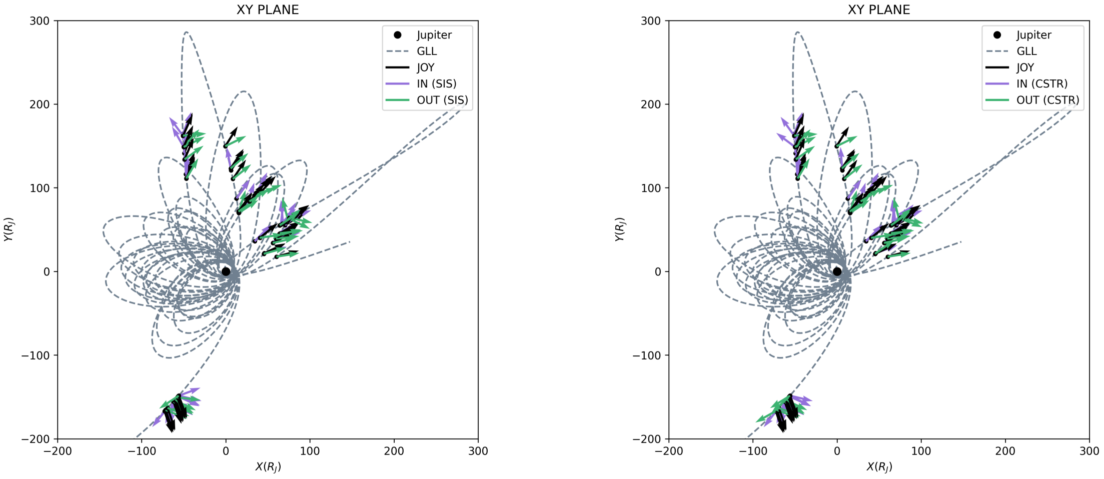

(a) Computed via SIS.

(b) Computed via CSTR.

Figure 4.5: Comparison of the normals computed by the SIS and the CSTR methods, plotted in the XY plane on Galileo's trajectory. The colours differentiate the direction of crossings: **in** towards the magnetosphere and **out** towards the magnetosheath.

4.2 Statistical results

In this section, we are going to present the statistical results obtained based on the normal computation via the different methods. We will explore the time separating two successive crossings, the solar wind dynamic pressure, the angles between two consecutive crossings, and the angles between the model and the normal obtained by the different methods. All the statistics were produced for all the crossings of all the missions, for the normals computed by the optimised processes, and oriented outward via the position of the one obtained by Joy's model.

4.2.1 Time between successive crossings

We computed the time between successive crossings, defined in this case as crossings that occurred within one day of each other. As seen in Figure 4.6, the distribution of the time has the shape of an exponential law for the dawn and dusk sides of the magnetosphere. We observe that a significant proportion of the crossings have a separating time below 180 minutes, for both cases. These histograms are similar to the distribution of the waiting time for the Juno spacecraft, found by Ma, P. Delamere, Schok, et al. (2022), with a transition time scale τ of around 6 hours.

In our case, by fitting an exponential law of the form $A\exp(-\Delta t/\tau)$ to our separating time data, we obtain a transition time scale of around 4.74 hours for the dawn side and around 4.82 hours for the dusk side. We also carried out a Kolmogorov-Smirnov (K-S) statistical test; the null hypothesis being that the two distributions are identical, and the statistic is the maximum absolute difference between the empirical distribution functions of the samples. With a test statistic of 0.0816 and a p-value of 0.9103, there is no significant difference between the separating time distributions for the dawn and dusk sides.

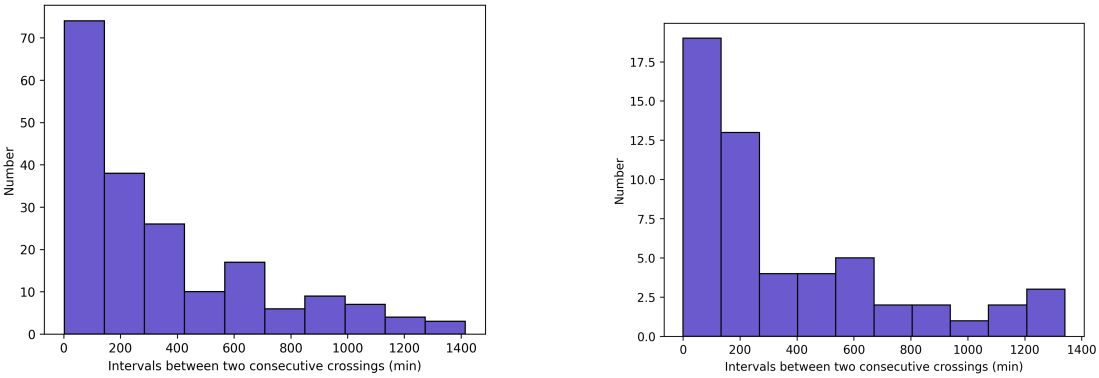

(a) Dawn side

(b) Dusk side

Figure 4.6: Time (in minutes) between successive crossings, defined as at less than a day apart from each other. The distributions are represented for the dawn and dusk sides of Jupiter's magnetopause.

4.2.2 Dynamic pressure

In the introduction, we discussed the model established by Joy et al. (2002) of the magnetopause of Jupiter. In this model, the position of the magnetopause is only dependent on the dynamic pressure of the solar wind; thus, we can compute the dynamic pressure at each crossing if we suppose that Joy's magnetopause passes through that point at the crossing time.

Figure 4.7 shows the comparison between the solar wind dynamic pressures obtained on both sides of the magnetosphere, expressed in nPa. On the dusk side, we observe that most of the crossings occur at dynamic pressures inferior to 0.1nPa, and the histogram shows a second peak around 0.6nPa.

On the other hand, we see on the dawn side that the majority of the crossings occur at dynamic pressure inferior to 0.2nPa, which is twice the amount for the dusk side. This is probably due to a trajectory bias induced by Juno: the Juno apojove[1] on the dawn side is closer to Jupiter than Galileo's apojove on the dusk side. Hence, Juno is unable to detect magnetopause crossings beyond -125 R_J. Juno crosses the magnetopause when it is closer to Jupiter, so when the dynamic pressure is higher than what we have on the other side with Galileo.

Via a Kolmogorov-Smirnov statistical test, where we obtained a p-value of 0.0006, we verified that the distributions are statistically different.

Let us consider now the bimodal shape of these pressure distributions, which was also observed by Ma, P. Delamere, Schok, et al. (2022). Joy et al. (2002) showed that Jupiter's magnetopause has two preferred locations, a compressed state with a subsolar stand-off distance of $63R_J$ and an expanded state at a subsolar stand-off distance of $92R_J$. This distribution shape is mainly due to a bimodal distribution of the solar wind dynamic pressure used to build their model. Still, it has not yet been shown that the solar wind parameters near Jupiter exhibit bimodal features.[Feng, Binzheng Zhang, et al., 2023]

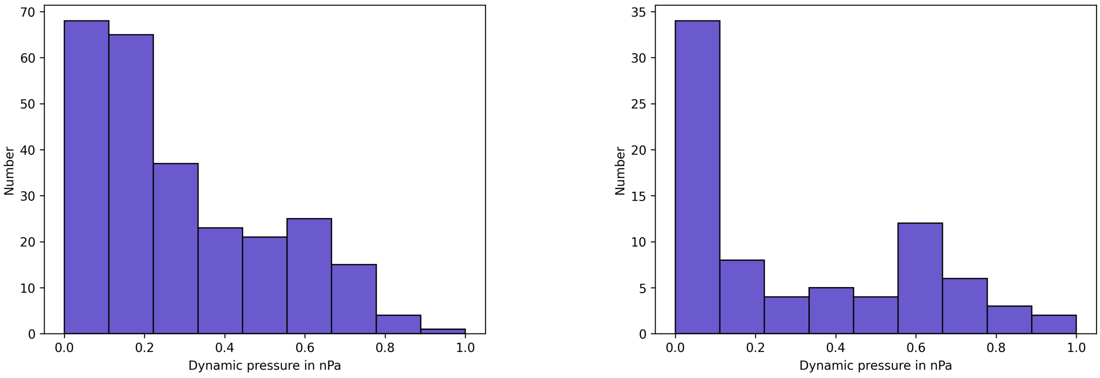

(a) Dawn side

(b) Dusk side

Figure 4.7: Solar wind dynamic pressure obtained by Joy's model, in nPa.

---

[1] The apojove is the point of the orbit farthest from Jupiter.

4.2.3 Angle between two consecutive crossings

After computing the normals to the magnetopause at the crossing points, we calculated the angles between consecutive crossings, expressed in degrees. This angle was measured in the XY plane of the *Jupiter Missions* frame already defined in this work. When looking from the north pole, the angle is positive counter-clock wise and negative clock wise.

Let us introduce what we consider as consecutive crossings. Given the previous results of the time intervals (Fig. 4.6), we stated that the condition for two crossings to be considered neighbours is a time interval of under three hours between the two. The statistics on the angles were done for the normals computed by the different methods, for comparison. We could show the histograms for the five methods and the two sides, but to be concise, we will represent here the cases of the Minimum Variance Analysis and Siscoe methods.

We pay particular attention to these methods since Minimum Variance Analysis is the most widely used technique for determining the magnetopause normal. However, as discussed later, our results show that it performs less reliably compared to other approaches —especially the Siscoe method, which proves to be the most effective in this study.

Figure 4.8 shows the histograms for the angles between normals computed by the MVA method on consecutive crossings, on the dawn and dusk sides. We calculated the angles from a normal computed at an **out** crossing to a normal computed at a consecutive **in** crossing, and vice-versa. To be clearer, these will be called **out/in** angles (and vice-versa).

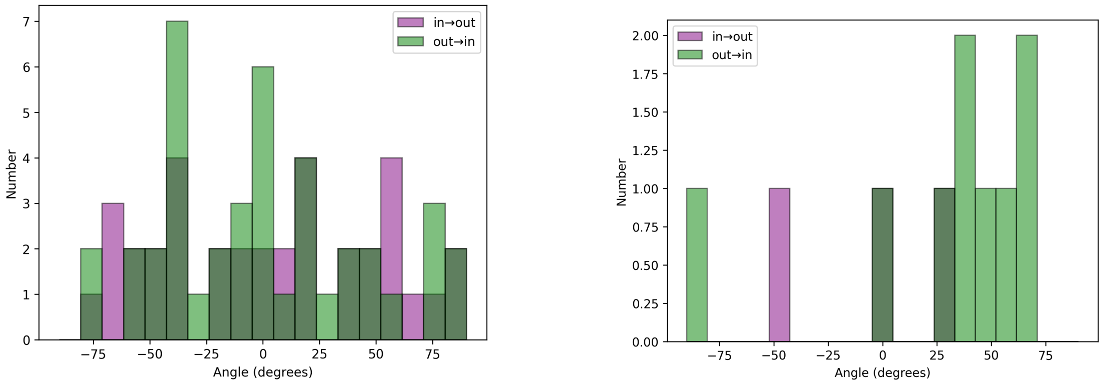

(a) Dawn side

(b) Dusk side

Figure 4.8: Angles between the normals at consecutive crossings in the XY plane, computed via the Minimum Variance Analysis (MVA). The angles between the vectors from an **in** to an **out** crossing are plotted in pink, and in green for the inverse; the dark green corresponds to the superposition of both colours.

If we focus first on the dawn side, we plotted the **out/in** and **in/out** angle distributions, but they are not statistically different (as determined by a K-S test). We did the same on the dusk side, but the results are not statistically significant. The problem on that side of the magnetopause is that we have fewer crossings than on the dawn side, and when we add the condition to have consecutive crossings, we have 12 crossings left, which is not enough to conclude on the angle distributions. As a comparison, we have 77 crossings on the dawn side that respect the condition exposed above.

We can now look at the results for the normals computed via the Siscoe method. As for the MVA, we can see on Figure 4.9 the histograms for the angles between normals computed by the SIS method on consecutive crossings, for the dawn and dusk sides. We observe two statistically different distributions (as determined by a K-S test) on the dawn side: one for the angles from **in/out** crossings distributed on the positive signs and one for the angles from **out/in** normals distributed on the negative signs. For the dusk side, the same problem as broached for the MVA method is represented here: we do not have enough consecutive crossings on the dusk side to draw statistical conclusions.

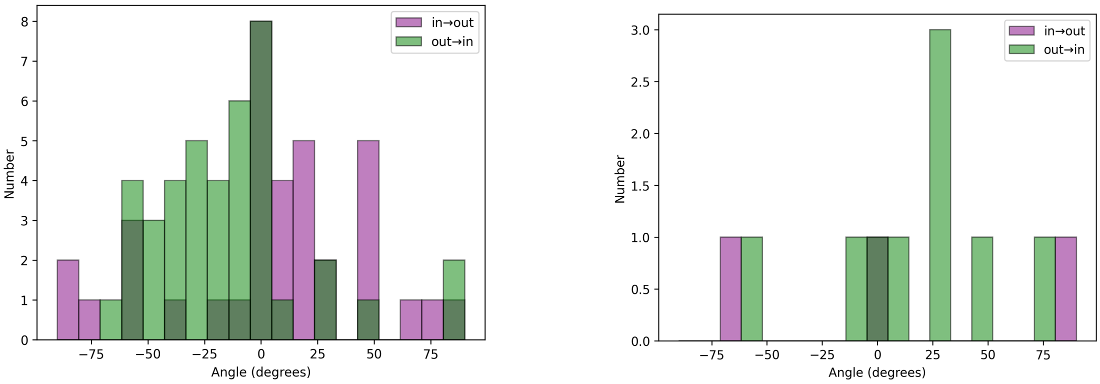

(a) Dawn side

(b) Dusk side

Figure 4.9: Angles between consecutive crossings in the XY plane, with the normals computed by the Siscoe method (SIS). The angles between the vectors from an **in** to an **out** crossing are plotted in pink, and in green for the inverse; the dark green corresponds to the superposition of both colours.

The histograms for the other methods can be found in the Appendix D, but we can comment here that we observe similar patterns to those discussed above. The BMBS and CSTR give similar distributions to the SIS method, with two statistically different distributions on the dawn side, distributed on different sides of the histograms, i.e. different signs for the angles between consecutive crossings. The histogram on the dawn side for the normals computed by the TDA is similar to that of the MVA: the distributions are not statistically different and cover all the angle values. For the dusk side, the results are the same for all methods: more crossings are needed to have statistically significant angle distributions.

As the results for the angles between consecutive crossings are not conclusive, we consider two approaches in order to study the normals to the magnetopause. First, we take on a statistical approach where we take Joy's normal as a reference in order to increase the number of dusk crossings; this is done in the next section. Then, we carry out a case study of the normal orientation for multiple consecutive crossings; this analysis can be found in the following chapter.

4.2.4 Angle between model and method normal

We were not able to obtain statistically significant angle results for the dusk side in the previous section, and this is due to the low amount of consecutive crossings (within three hours of each other). Thus, we try another approach in this section; we measure the angles between the normals obtained by the methods and the normals obtained by the model of Joy et al. (2002). These angles were measured in the XY plane defined already in this work. The angle is positive if the second vector is to the left of the first one, and negative if the second vector is to the right of the first one. In this case, we do not have conditions on the time between crossings that reduce the populations. We carry out this measurement for all methods on all crossings and have statistically significant results. As for the previous section, we concentrate on the results given by the Minimum Variance Analysis and Siscoe method.

Figure 4.10 shows the histograms for the angles between the MVA and Joy normals, computed at each crossing, for the dawn and dusk sides of the magnetopause. If we focus on the dawn side first, we see two distributions: one for the angles between the normals at the **in** crossings distributed roughly on the negative angles, and one for the angles between normals at the **out** crossings distributed roughly on the positive angles. We verified the difference between the two distributions thanks to a Kolmogorov-Smirnov test and obtained two statistically different distributions.

For the dusk side of the magnetopause, we also observe two distributions that are statistically different. The main difference between the two sides is that the distribution for the angles between the normals at the **in** crossings is distributed on the positive angles, and the one for the angles between normals at **out** crossings is distributed on the negative angles. We have an inversion of the angle signs between the dawn and dusk sides, and this is an essential observation that we will revisit later.

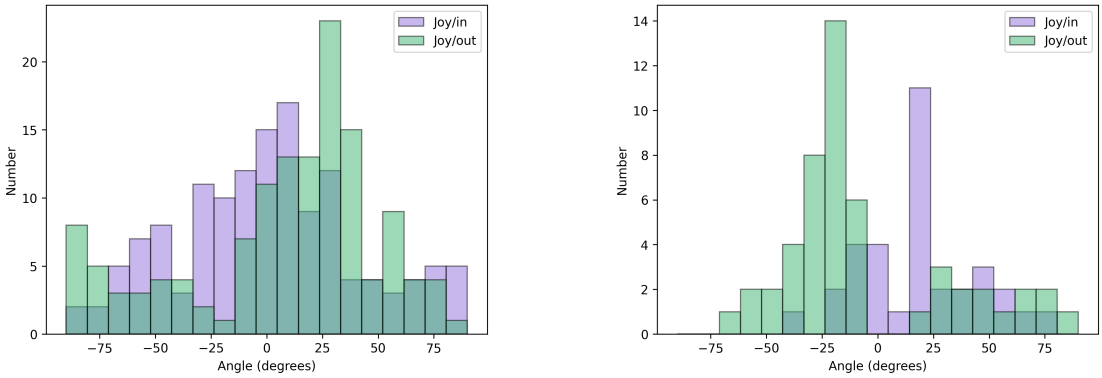

(a) Dawn side

(b) Dusk side

Figure 4.10: Angles between the normal of Joy et al. (2002) and the normal obtained by the MVA method, measured in the XY plane. The colours differentiate the angles measured at **in** or **out** crossings.

We can now look at the results for the Siscoe method: Figure 4.11 represents the histograms for the angles between the SIS and Joy normals for all crossings, on the dawn and dusk sides. We observe similar results as for the MVA method: two statistically different distributions for the **in** and **out** crossings, centred on angles of opposite signs, and an inversion of those signs between the dawn and dusk sides. Nevertheless, we remark that the distributions obtained via the MVA method on the dawn side of the magnetopause are broader than the ones obtained via the Siscoe methods, being noisier and containing more outliers, showing that this second approach gives better-defined normals than the MVA.

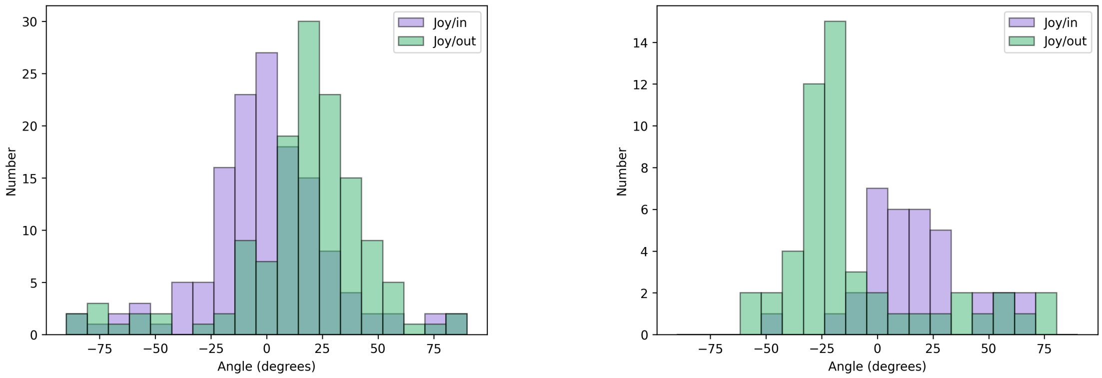

(a) Dawn side

(b) Dusk side

Figure 4.11: Angles between the normal of Joy et al. (2002) and the normal obtained by the SIS method, measured in the XY plane. The colours differentiate the angles measured at **in** or **out** crossings.

To avoid overloading this section, the histograms for the BMBS, CSTR and TDA methods can be found in Appendix D. However, it is still worth noting that the statistical results are similar to what was observed for the MVA and SIS methods. For each method, we have two statistically different distributions for the **in** and **out** crossings centred on opposite signs of angles, and we have an inversion of those signs between the dawn and dusk sides. This shows that even if the normals from the various methods give slightly different results, the statistics drawn from those normals are essentially the same.

4.2.5 Fixed windows

The statistical results shown above are associated with the normals computed via the optimised methods, on time windows depending on the methods and the crossings. In order to question the usefulness and accuracy of our optimised methods, we also generate the statistical results for the normals computed via the fixed 20-minute windows that can be found in Appendix D. In this section, we only show some of the results found for the fixed windows to compare them to the previous results for the optimised ones.

In Figure 4.12, we compare the histograms for the angles in the XY plane between the MVA normals and Joy's normals on the dusk side of the magnetopause. The first one was computed for the normals obtained via the optimised version of the MVA, where the windows are chosen to have the best possible normals; it is the same as in the previous section. The second one was computed for the normals obtained via the arbitrary version of the MVA, where the time windows are fixed at 20 minutes for all crossings.

In both cases, we have two statistically different distributions for the **in** and **out** crossings, distributed over angles of opposite signs: positive for the **in** and negative for the **out** crossings. We observe that the histograms have similar shapes and the Kolmogorov-Smirnov statistical test showed no significant difference for the distributions of angles for the **in** crossings (and **out**, respectively) between the two approaches.

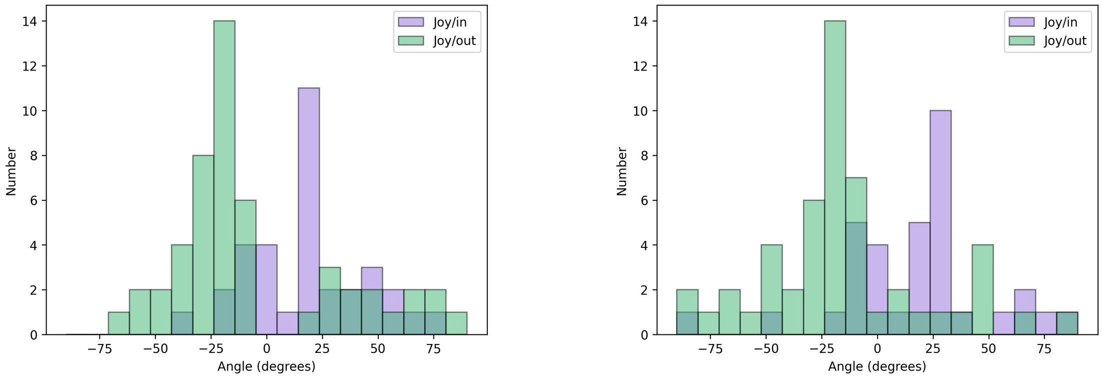

(a) Computed via optimised windows.

(b) Computed via fixed windows.

Figure 4.12: Angles between the normal of Joy et al. (2002) and the normal obtained by the MVA method on the dusk side, measured in the XY plane. The colours differentiate the angles measured at **in** or **out** crossings.

To be complete, we can also compare the histograms for the angles between consecutive crossings on the dawn side for the Siscoe method, for example. Figure 4.13 shows those statistical results for the optimised and fixed windows. The first histogram is the one we already showed above, with the angles between normals computed via the optimised SIS method on consecutive crossings. The second one represents the angles between normals computed at consecutive crossings, but with the fixed 20-minute windows option. We can see that both of those histograms have two distributions of angles, one for the angles between normals from **in** to **out** crossings and one for the angles between normals from **out** to **in** crossings. The distribution shapes are similar between the two computation options, and are spread on the same signs.

Of course, we could compare the results for the optimised and fixed option two by two: for the angles between consecutive crossings or the angles between the model and method normals, for the dawn and dusk side, and the different methods. However, this is not useful as the results are similar between the two options in all cases. The observations made in this section allow us to conclude that the optimised and fixed options of computation give **broadly similar statistical results**, but with a more noisy distribution with the fixed windows.

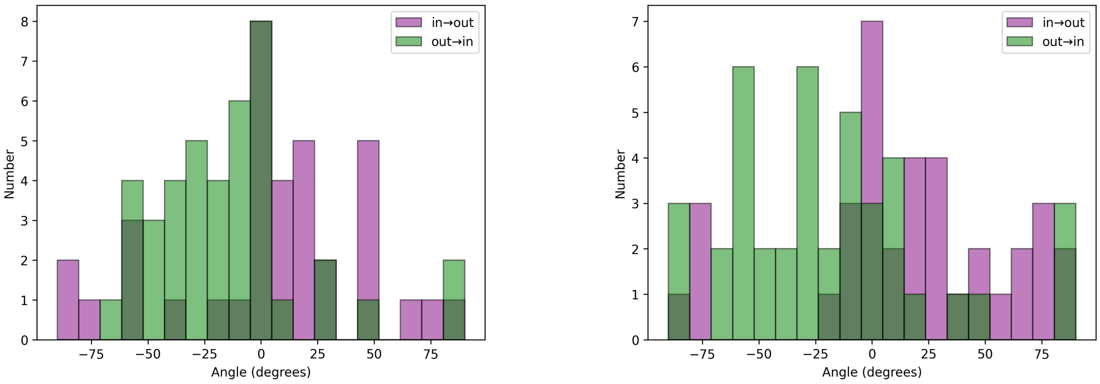

(a) Computed via optimised windows

(b) Computed via fixed windows

Figure 4.13: Angles between consecutive crossings on the dawn side in the XY plane, with the normals computed by the Siscoe method (SIS). The angles between the vectors from an **in** to an **out** crossing are plotted in pink, and in green for the inverse.

Chapter 5

Case study

In the previous chapter, we presented the normals and statistical results from our computations to have a global view of the phenomenon happening at the magnetopause's surface. In this chapter, we focus on specific cases of magnetopause crossings and analyse them in detail. We look for cases of crossings that meet two conditions: consecutive, so at time intervals of less than three hours, and alternate, **in** then **out**, or the inverse. Indeed, we have consecutive crossings in the same direction in our crossings list, which is, of course, not physically possible. This can be due to gaps in the analysed data that led to the loss of crossing signatures, or chaotic crossing of the complex boundary layer that hindered their identification.

This search is done for all missions, but conclusive results are only found for the Galileo and Juno spacecraft. We kept cases that comprised at least three consecutive alternate crossings, and we obtained 17 cases (these dates can be found in Table 5.3).

Here, we take a particular interest in the cases where the computed normals oscillate around the model normal. We obtained seven such events, three for the Galileo spacecraft and four for the Juno mission. In this chapter, we explore one case for each spacecraft, which allows us to see one for each side of the magnetopause. Then, we question the reliability of the detection of oscillating normals.

5.1 Galileo

We identified four cases of consecutive alternate crossings for the Galileo spacecraft, three on the dawn side and one on the dusk side. There were other cases of crossings completing the conditions, but they were only pairs of crossings, and we only took cases starting from three alternate consecutive crossings. We present here the case on the dusk side of the magnetopause.

5.1.1 4 December 2000

On 4 December 2000, Galileo crossed Jupiter's magnetopause three times: two **out** crossings separated by one **in** crossing. We can observe the changes in the magnetic field due to these crossings in Figure 5.1, where its components in the *Jupiter Missions* frame are plotted. First, the satellite is in the magnetosphere, and the magnetic field is relatively smooth. Then, we see an abrupt change in the B_X and B_Y components and a highly oscillating magnetic field characteristic of the magnetosheath. During the second crossing, the spacecraft goes from the magnetosheath to the magnetosphere, and this is accompanied by a brutal change in the B_X and B_Z components and a calmer magnetic field. Finally, Galileo goes back to the magnetosheath with a change in all the components, and the magnetic field is once again highly oscillating.

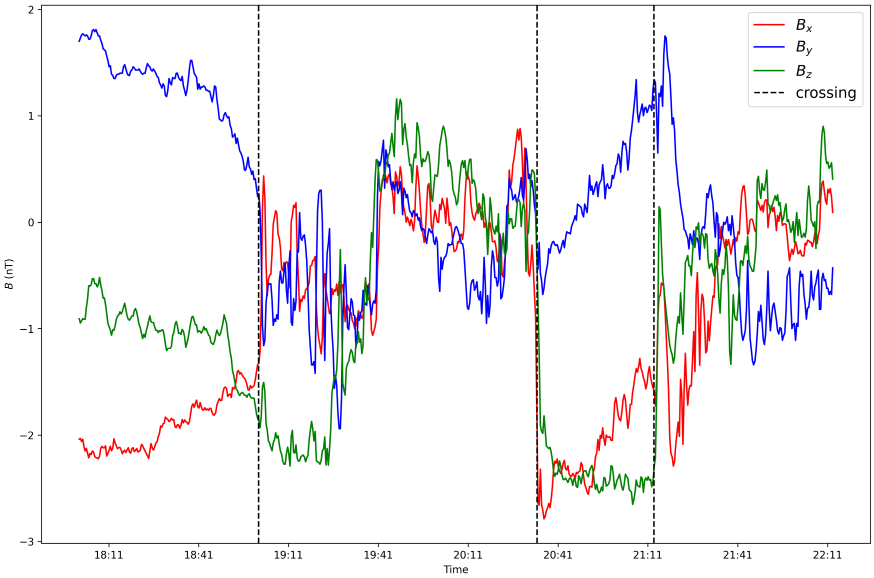

Figure 5.1: Magnetic field in the *Jupiter Missions* frame during the crossings of 4 December 2000, measured by Galileo.

Table 5.1 contains the precise information for the three consecutive crossings. As seen in the first column, the crossings are close in time, within an hour and forty minutes of each other. The direction of the crossing, the position in the XY plane and the angle between Siscoe's normal and Joy's normal in the XY plane are also listed in the table.

An interesting observation can be made on this angle: it is negative for the **out** crossings and positive for the **in** crossing. Siscoe's normals at the **out** crossings are on the right side of Joy's normals, and Siscoe's normal at the **in** crossing is on the left side of Joy's normal. This means that the normals oscillate in response to a perturbation on the magnetopause's surface, and it is a significant result that will be explored more in Chapter 6.

Figure 5.2a shows the trajectory of Galileo between 4 November 2000 and 4 January 2001, on the dusk side of the magnetopause. On the left figure, the normals at the **in** and **out** crossings computed by the Siscoe method are displayed, and the normals of Joy's model are shown as a reference. On the right figure, we represent the normals computed by the different methods as a way to compare the results and evaluate the trustworthiness of Siscoe's normal in that case. This figure allows us to have an idea of where the crossing happened on Galileo's trajectory, and we now zoom in on those crossings to study them in detail.

TIME	IN/OUT	X (R_J)	Y (R_J)	ANGLE (°)
19:01:00	out	-50.07	149.07	-17.94
20:34:00	in	-50.06	148.82	53.38
21:13:00	out	-50.05	148.72	-40.06

Table 5.1: Time, direction, position and angle between the normal by Siscoe and the normal by Joy in the XY plane, for the three consecutive alternate crossings made by Galileo on 4 December 2000.

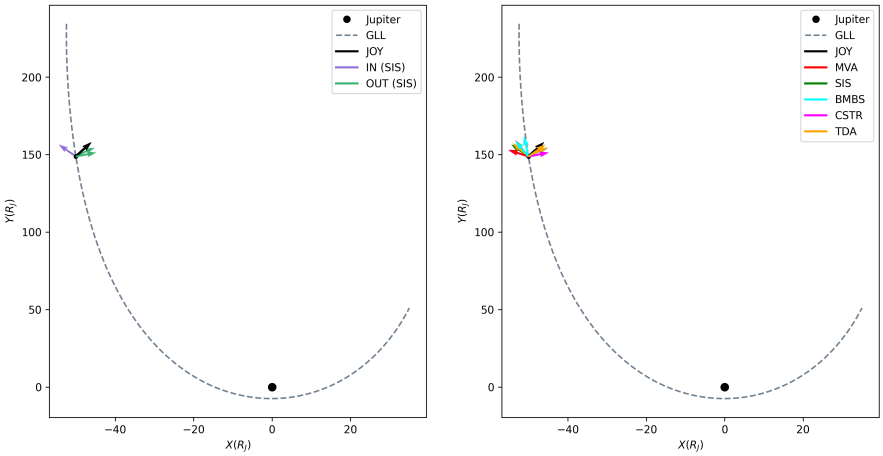

(a) Trajectory between 4 November 2000 and 4 January 2001.

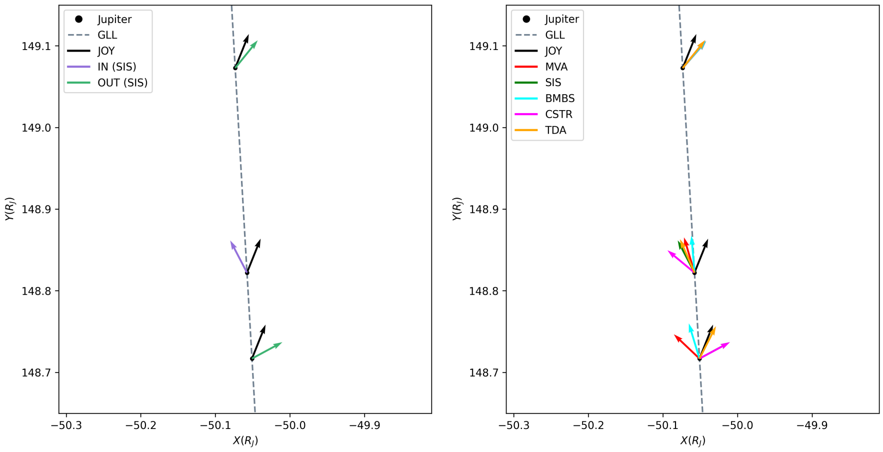

(b) Trajectory on 4 December 2000, around 20:30.

Figure 5.2: Trajectory of Galileo in the XY plane. The normals computed via the model of Joy et al. (2002) are plotted on both figures. On the left figures are plotted the normals computed via the SIS method, with the two colours for the **in** and **out** crossings. On the right figures are plotted the normals computed via the different methods, one for each colour.

Figure 5.2b shows the normals computed at the magnetopause crossings made by Galileo on 4 December 2000. Like for the previous figure, the two plots correspond to the normals computed by the Siscoe method on the left and the comparison between the normals computed via all the methods on the right. We can see that the condition of the alternate crossings is respected on the right figure, as we have one **out**, then an **in**, and finally an **out** crossing. By looking at the right figure, we can consider the three crossings individually, from the top one to the bottom one:

- For the first crossing: all methods point in the same direction.
- For the second crossing: all the normals are close to each other but do not point in the same direction.
- For the last crossing: the SIS, CSTR normals point in the same direction (the SIS is not visible as it is under the CSTR vector), the TDA vector is closer to the normal of Joy, while the MVA and BMBS ones point on the other side.

We note that if we only look at the right panel of Figure 5.2a, we see a wide distribution of the method normals around the normal of Joy, and we could have the impression that the normals obtained by the different methods give greatly incoherent results. However, Figure 5.2b and the comparisons made above show that it is only an impression because the **in** and **out** crossings are on top of each other.

We have made a qualitative estimation of the difference between the plotted normals, and to better estimate the difference between the normals, we computed the angles between the vectors obtained by the different normals and Joy's model in the XY plane. We can see those angles in Figure 5.3, plotted for the three consecutive crossings of Galileo.

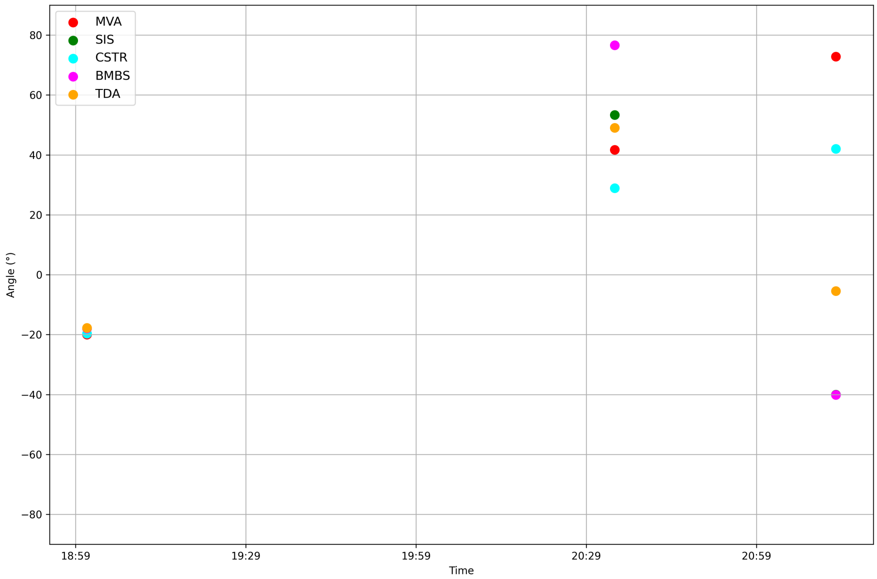

Figure 5.3: Angles (in degrees) between the normals computed by the different methods and the normal of Joy et al. (2002) in the XY plane for each crossing of Galileo on 4 December 2000.

For the first crossing at 19:01, it is evident that all methods demonstrate a high degree of concordance. For the second crossing at 20:34, we see that the SIS, TDA and MVA are within 15 degrees of each other, while the CSTR and BMBS are farther away. For the last crossing at 21:13, the SIS and CSTR are on top of each other, the TDA has the same sign, but is 30 degrees away, and the BMBS and the MVA have angles of opposite signs.

The comparison between the different methods allows us to be confident in the Siscoe normals plotted on the left-hand side of the figure, because at least one other method agrees with this normal for each crossing. The difference between the methods and the trustworthiness of their results is discussed in Chapter 6.

5.2 Juno

The Juno mission has made the most magnetopause crossings, and we identified thirteen cases of consecutive alternate crossings, all on the dawn side except for one case on the dusk side. There were other cases of crossings completing the conditions, but they were only pairs of crossings, and we only took cases starting from three alternate consecutive crossings. Here, we present one of the cases on the dawn side.

5.2.1 19 February 2017

On 19 February 2017, Juno made three consecutive alternate crossings of Jupiter's magnetopause: two **out** and one **in** the magnetosphere. We can observe the changes in the magnetic field due to these crossings in Figure 5.4, where its components in the *Jupiter Missions* frame are plotted.

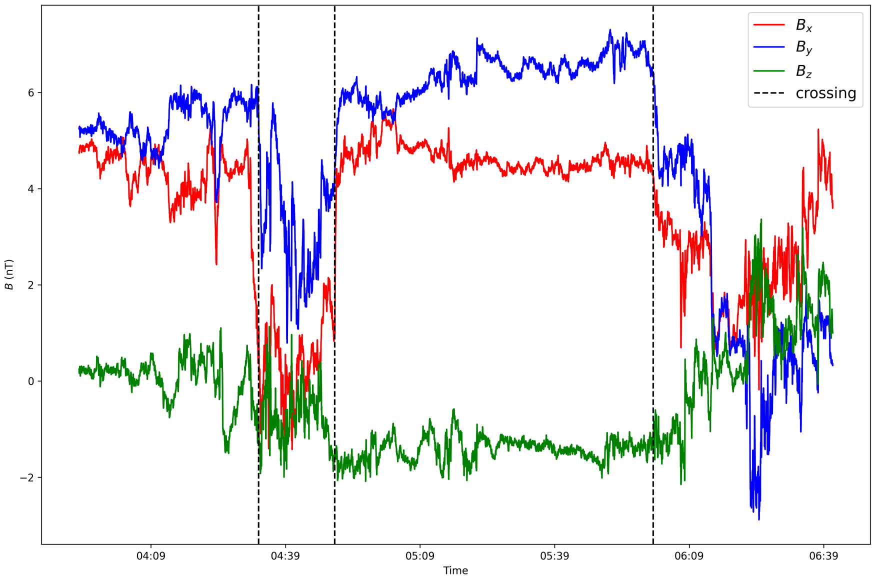

Figure 5.4: Magnetic field in the *Jupiter Missions* frame during the crossings of 19 February 2017, measured by Juno.

First, the satellite is in the magnetosphere, and then we see an abrupt change in the B_X component. It is in the magnetosheath, and we observe the characteristic highly oscillating magnetic field. Afterwards, the spacecraft goes into the magnetosphere, and the magnetic field is calmer. We then see a last crossing, towards the magnetosheath, accompanied by a modification of the magnetic field components.

The difference between the aspects of the magnetic field curves for the Galileo (Fig. 5.1) and Juno (Fig. 5.4) missions is due to the difference in sampling rate. Indeed, Galileo typically has a lower sampling rate than Juno's one-second one due to the failed high-gain antenna deployment.

Table 5.2 contains the precise information for the three consecutive crossings made by Juno on that date. As seen in the first column, the crossings are close in time, as they are all contained in a time interval of one and a half hours. The direction of the crossing, the position in the XY plane and the angle between Siscoe's normal and Joy's normal in the XY plane are also listed in the table.

An interesting observation can be made on this angle: it is positive for the **out** crossings and negative for the **in** crossing. The normals at the **out** crossings are on the left side of Joy's normals, and the normals at the **in** crossings are on the right side of Joy's normals. We can note that the signs for **in** and **out** crossings are inverted compared to what we observed on the dusk side with Galileo. The reasons for such oscillations and the dawn/dusk inversion will be discussed in the following chapter.

TIME	IN/OUT	X (R_J)	Y (R_J)	ANGLE (°)
04:33:00	out	-25.31	-97.53	28.39
04:50:00	in	-25.32	-97.56	-21.43
06:01:00	out	-25.36	-97.66	21.42

Table 5.2: Time, direction, position and angle between the normal by Siscoe and the normal by Joy in the XY plane, for the three consecutive alternate crossings made by Juno on 19 February 2017.

Figure 5.5a shows the trajectory of Juno from one month before to one month after 19 February 2017, on the dawn side of the magnetosphere. On the left figure, the normals at the **in** and **out** crossings computed by the Siscoe method are displayed, and the normals of Joy's model are shown as a reference. On the right figure, we represent the normals computed by the different methods as a way to compare the results and evaluate the trustworthiness of Siscoe's normal in that case. This figure allows us to have an idea of where the crossing happened on Juno's trajectory, and we now zoom in on those crossings to study them in detail.

Figure 5.5b shows the normals computed at the magnetopause crossings made by Juno on 19 February 2017. Like for the previous figure, the two plots correspond to the normals computed by the Siscoe method on the left and the comparison between the normals computed via all the methods on the right. We can see that the condition of the alternate crossings is respected on the right figure, as we have one **out**, then an **in**, and then an **out** crossing. By looking at the right figure, we can consider the three crossings individually, from top to bottom:

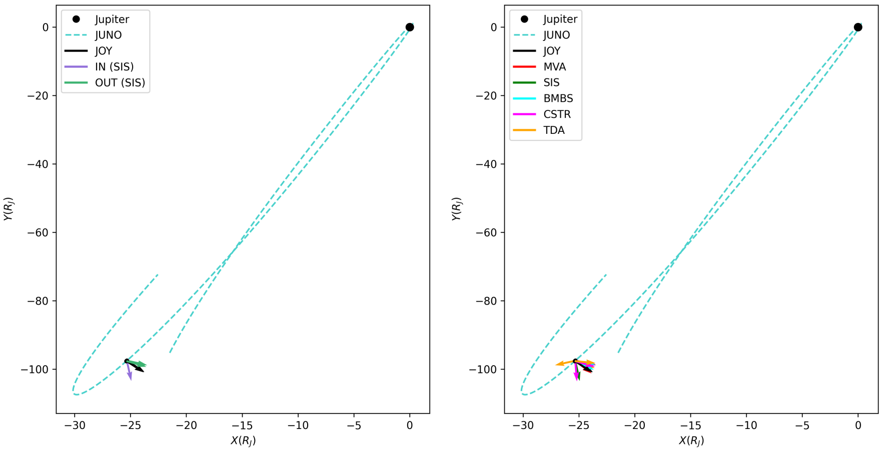

(a) Trajectory between 19 January 2017 and 19 March 2017.

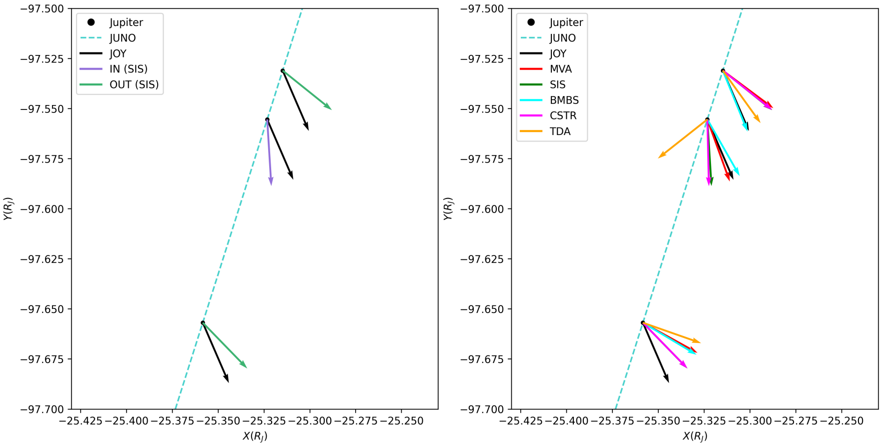

(b) Trajectory on 19 February 2017, around 05:00.

Figure 5.5: Trajectory of Juno in the XY plane. The normals computed via the model of Joy et al. (2002) are plotted on both figures. On the left figure are plotted the normals computed via the SIS method, with the different colours for the **in** and **out** crossings. On the right figure are plotted the normals computed via the different methods, one for each colour.

- For the first crossing: the SIS, CSTR, and MVA normals are on top of each other, while the TDA and the BMBS are closer to Joy's normal.
- For the second crossing: the SIS and CSTR normals point in the same direction, while the three other methods are more dispersed.
- For the third crossing: all methods are on the same side of Joy's normal, the SIS and CSTR normals are on top of each other, the BMBS and MVA too, while the TDA is a bit farther.

The qualitative comparison we made above is an estimation based on the plotted normals. To better estimate the difference between the normals, we computed the angles between the vectors obtained by the different normals and Joy's model in the XY plane. Those angles are shown in Figure 5.6, plotted for the three consecutive crossings of Juno. For the first crossing at 04:33, the BMBS has virtually the same direction as Joy's normal, while the angle for the TDA is around 10 degrees farther, and the three other methods are in the same direction. For the 04:50 crossing, the CSTR and SIS have a near equal angle while the other are farther apart. Lastly, for the 06:01 crossing, the CSTR and SIS agree with each other, and the same goes for the MVA and BMBS, while the TDA is at higher angles.

This comparison between the different methods allows us to be confident in the Siscoe normals plotted on the left side of the figure, because at least one of the other methods agrees with that one for each crossing.

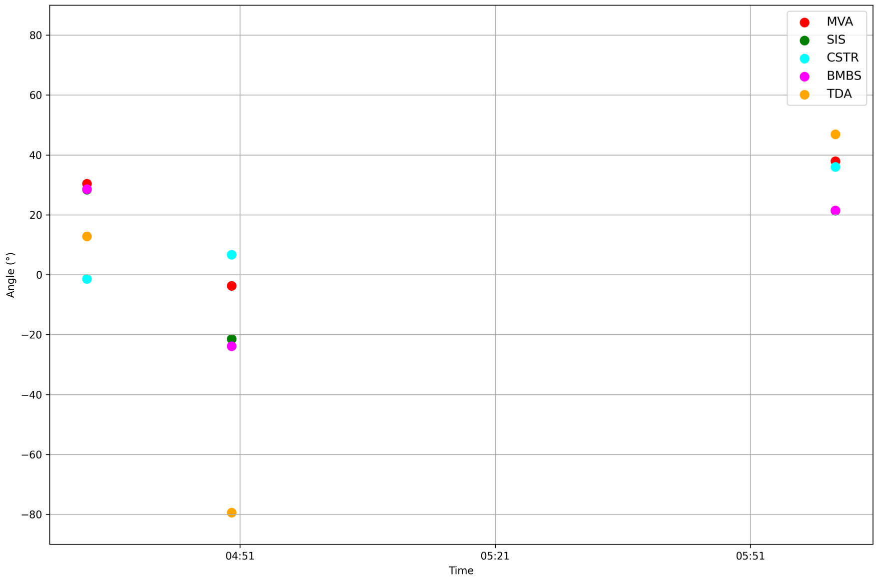

Figure 5.6: Angles between the normals computed by the different methods and the normal of Joy et al. (2002) in the XY plane for each crossing of Juno on 19 February 2017.

5.3 Fixed windows

As for the statistical results, we want to know if the choice of the time window affects the detected consecutive alternative crossings.

Using the optimised window-size option, we identified seven cases where the method normals oscillate around the model normal: three during Galileo crossings and four during Juno crossings. In the previous section, we displayed two examples of such oscillating normals, one for each side of the magnetosphere.

Applying the same search with the fixed window-size option likewise yielded seven cases, three for Galileo and four for Juno. However, only five of these cases were common to both window-size approaches.

This means that the choice of the time window affects the orientation of the normal vectors, and normals that are seen oscillating with one of the options can

DATE (YYYY-MM-DD)	S/C	OPTI	FIXED
1996-05-29	GLL	**Y**	**Y**
1996-05-30	GLL	N	**Y**
1996-06-01	GLL	**Y**	N
2000-12-04	GLL	**Y**	**Y**
2016-08-01	JUNO	**Y**	**Y**
2016-08-08	JUNO	N	N
2016-11-25	JUNO	N	N
2016-12-22	JUNO	N	N
2017-01-24	JUNO	N	**Y**
2017-02-19	JUNO	**Y**	**Y**
2017-03-09	JUNO	N	N
2017-05-06	JUNO	N	N
2017-06-16	JUNO	**Y**	N
2017-06-18	JUNO	**Y**	**Y**
2017-06-29	JUNO	N	N
2018-06-16	JUNO	N	N
2022-06-08	JUNO	N	N

Table 5.3: Comparison between the normal oscillations detected in consecutive alternate crossings, for the optimised and arbitrary options of computation. The columns contain the date of the consecutive alternative crossings, the spacecraft that measured them, and if oscillations around the model normal were detected as a function of the computation option.

be found not oscillating with the other. Table 5.3 allows a comparison between the cases detected via the optimised or fixed option. The first column contains the dates where a minimum of three consecutive alternate crossings were found, and the second column tells us which spacecraft detected these crossings. Then, the last two columns inform about which option allowed the detection of oscillations of Siscoe's normals around the model. We observe that both options entail the detection of seven cases of oscillations, but not on the same dates.

Yet, the two cases studied in the previous sections were observed with the normals obtained by the optimised and fixed methods. The other three cases where oscillations are detected via the fixed and optimised windows can be found in Appendix E. We can measure the angles obtained between the normals from the Siscoe method and the Joy model in the XY plane, between the optimised and arbitrary options for the two case studies performed in this chapter.

The comparison between the angles measured for the two options on the crossings measured by Galileo on 4 December 2000 can be found in Figure 5.7. We observe that the normals point in the same direction for the first crossing, have an angle difference of around 20 degrees for the second crossing and of around 30 degrees for the last one. The critical remark here is that the oscillations between the negative and positive angles are found in both cases.

Figure 5.8 shows the comparison between the angles measured for the two options on the crossings measured by Juno on 19 February 2017. We observe that the normals have an angle difference of around 10 degrees for the first crossing, 20 degrees for the second, and 10 degrees for the last crossing. As for the Galileo crossings, the oscillations between the positive and negative angles are found in both the optimised and arbitrary cases.

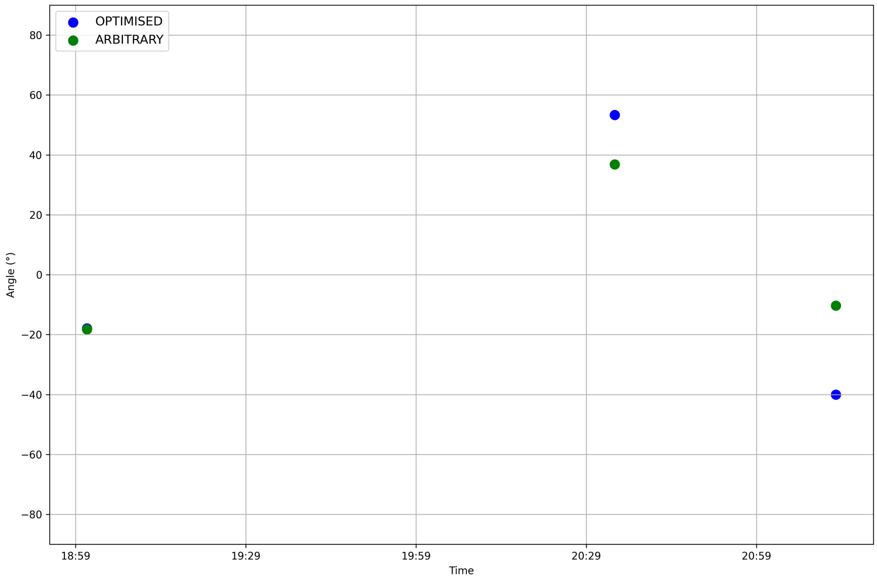

Figure 5.7: Angles between the Siscoe's normal computed by the different options and the normal of Joy et al. (2002) in the XY plane for each crossing on 4 December 2000.

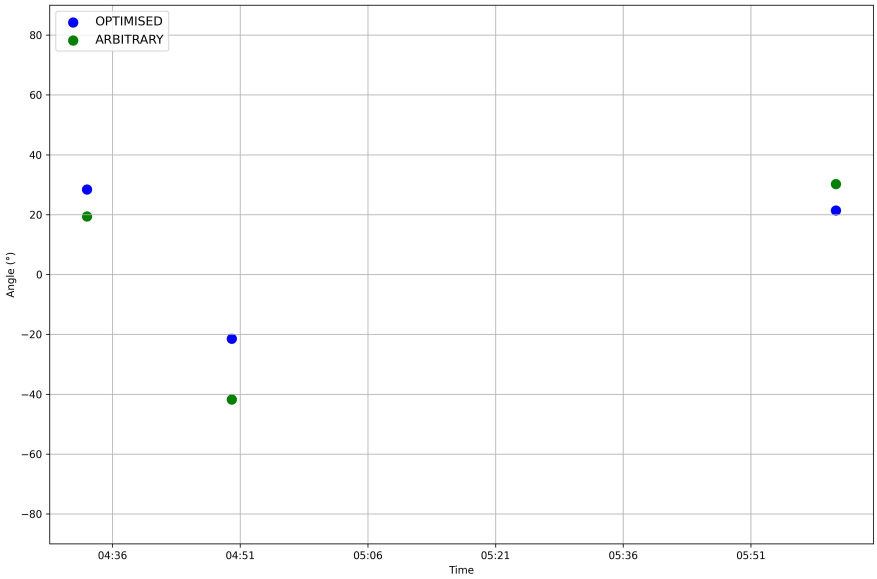

Figure 5.8: Angles between the Siscoe's normal computed by the different options and the normal of Joy et al. (2002) in the XY plane for each crossing on 19 February 2017.

In this section, we found that we see oscillations of the method normals around the model normal in roughly half the cases of consecutive alternate crossings. Contrary to the statistical results, it was observed here that the optimised and fixed options of computation give **different normal vectors**, allowing or not the detection of oscillations. This point is further discussed in the following chapter.

Chapter 6

Discussion

6.1 Reliability

Before discussing the results in terms of the different scenarios responsible for magnetopause perturbations, we first examine the parameters that influence the computation of the normals and the resulting analyses. In this study, we employed five different methods together with two window-size options to determine the normals. These normals were then projected onto the XY plane of the *Jupiter Missions* frame, and their angles relative to the Joy model were calculated. The influence of each of these aspects on the results is discussed in this section.

6.1.1 Joy's magnetopause

In this work, we compared the normal to the magnetopause obtained by the different methods to a model normal. We used the magnetopause model of Joy et al. (2002), which supposes that the position of the boundary is only dependent on the solar wind dynamic pressure. This is an approximation, and Feng, Binzheng Zhang, et al. (2023) showed that the dynamics of the Jovian magnetosphere, especially the rotating magnetodisk, may have a significant impact on the shape of Jupiter's magnetopause. Joy's model only considers the external factor of the solar wind dynamic pressure. Still, internal factors have to be taken into account to represent the phenomenon influencing the position of the magnetopause. Of course, the use of a model here is for comparison purposes, and a more complete representation could complicate the computation.

We can also note that Rutala et al. (2025) established a new model for the shape of Jupiter's bow shock and magnetopause, based on the measurements from the Ulysses, Galileo, Cassini and Juno spacecraft. It was compared to the model of Joy et al. (2002) and shown to predict a closer subsolar standoff distance and a larger polar flattening. We did not use Rutala's model in this master's thesis due to a lack of time, but it could be interesting to compare the two representations of the magnetopause in a future work.

6.1.2 Projection effects

In the previous chapters, we measured the angles between the model and methods normals by projecting them in the XY plane of the *Jupiter Missions* frame. This frame was chosen for the representation of the normals and angles because the spatial configuration can be easily conceptualised, allowing for an intuitive understanding of the different measurements. However, this projection plane is the same for all spacecrafts and all crossings, which can entail projection effects. In some cases, the projected angle measured might be significantly different from the real inclination between the normals.

One potential solution is to define a new reference frame JVT via Joy's normal at each crossing point. The J axis is the normal obtained by Joy's model, the T axis is computed by the cross-product of the J axis and the unit vertical vector (along the Z axis), and the final V axis completes the right-handed frame. The angles can be measured between the normal obtained by the method and Joy's normal (the J axis) in the JT plane.

This computation was not done in the scope of this work, but could be a way to improve the reliability of the angle measurement technique. We do not expect much difference for crossings close to the equatorial plane, as the ones considered in this work, but this could be of importance at higher latitude (e.g. the Juno crossings on the dusk side) or further down-tail.

6.1.3 Methods

Difference between the methods

To compute the normals to the magnetopause at the crossings position, we used five different methods for comparison. Those methods give different results, since they compute the normal vector using various characteristics. We already looked at the difference between those computations via the angle between the method normal and the model normal by Joy et al. (2002) in the cases of Chapter 5 via Figure 5.3 and 5.6. We observed that the Siscoe method is always in agreement with at least one other method, and most of the time it is with the Constraint method.

In this section, we compare the different methods in pairs to see which ones agree with each other. We were inspired by Adam Masters et al. (2012), who measured the angle between the MVA and TDA normals and stated that they were in good agreement, as it was below 30 degrees. We compare the methods two by two, by computing the difference in angle between the normals, and considering that they differ when this angle is greater than 30 degrees. This was done for the 357 crossings for which the angles can be obtained, and we compare the results obtained by the different methods in Figure 6.1.

Figure 6.1 shows the percentage of the total number of crossings for which the angle between normals obtained by the pair of methods is greater than 30 degrees. The comparison tests are sorted from the smallest to the largest number of inconsistencies between the methods. We observe that the Siscoe and Constraint methods are in agreement most of the time, with only 4.2% of the cases where they

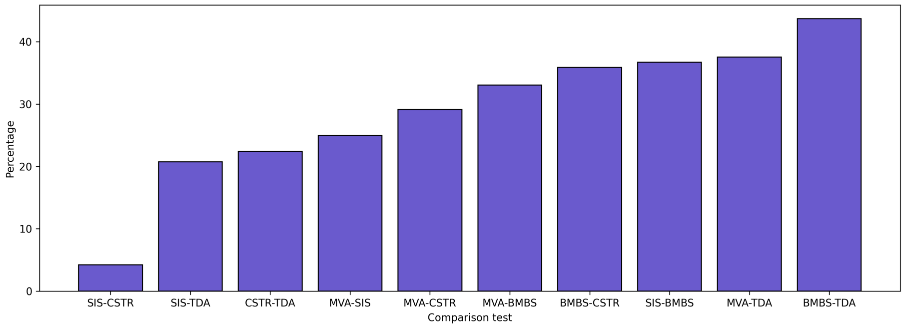

Figure 6.1: Percentage of crossings for which the angle between the normals is greater than 30 degrees. The methods are tested in pairs, and the performed test is referenced on the horizontal axis.

differ by more than 30 degrees. Afterwards, the TDA agrees with the SIS and CSTR methods for approximately 80% of the crossings. Then, the MVA agrees with the SIS and CSTR in more than 70% of the cases. The rest of the method pairs are in disagreement in more than one case out of three.

We can summarise these results as follows: most of the time, the Siscoe and Constraint methods predict the same normal, and if another method agrees with this normal, it is likely to be the Tangential Discontinuity Analysis or the Minimum Variance Analysis. These results are similar to what we found in the case studies and also to the behaviour shown in Figure 3.1, regarding the impact of window size on the computed normal.

The higher amount of outliers for the MVA than for the SIS normals is also illustrated by the difference between the histograms of the angles between the method and the model. Figures 4.10a and 4.11a can be compared, and we see that the histogram for the MVA is broader and noisier than the histogram for the SIS: the Siscoe method gives better-defined normals.

The fact that the Minimum Variance Analysis is not the method that gives the best results - meaning that it provides a higher number of outliers than others, like the Siscoe, the Constraint or the Tangential Discontinuity Analysis - is a significant result. It is the most used method when computing the normal to the magnetopause, but the results should be used with caution. This has already been observed by Knetter et al. (2004), who found that the cross-product method (TDA) yields more accurate normal estimates than the MVA when the magnetic component normal to the surface is small.

Tangential and rotational discontinuity

Let us recall the different principles for the five normal computation methods. The Minimum Variance Analysis defines the normal vector in the direction of minimum variance of the magnetic field [Sonnerup and Cahill Jr, 1967]. The Siscoe method defines the normal as the direction of the smallest average field amplitude [Siscoe et al., 1968]. The BMBS method is an MVA-Siscoe hybrid that was introduced by Xuanye Ma et al. (2016). The constraint method resembles the MVA, but with the added constraint of a tangential discontinuity [Sonnerup and Cahill Jr, 1968]. The tangential discontinuity analysis is the cross-product between the average field before and after the crossing in the case of a tangential discontinuity [Adam Masters et al., 2012].

These methods can be applied to the two different types of discontinuities: rotational and tangential. The MVA and BMBS can be used for all discontinuities, while the SIS, CSTR and TDA are more adequate for tangential discontinuities.

In a rotational discontinuity, the magnitude of the magnetic field component tangential to the magnetopause remains constant as its direction changes, while the normal field component is continuous and non-zero. On the other hand, tangential discontinuities have different tangential field magnitudes on the two sides of the magnetopause, and the normal field component is zero [Sonnerup and Cahill Jr, 1968]. Sonnerup and Cahill Jr (1967) associated rotational discontinuities with open magnetospheres, and tangential discontinuities with closed magnetospheres.

To a first-order approximation, ignoring the reconnection, the magnetopause can be considered a tangential discontinuity separating the plasma of the magnetosphere and magnetosheath [Cutler et al., 2011]. To evaluate the degree to which the magnetopause is regarded as a tangential discontinuity, we can compute the ratio between the mean normal field component and the mean field strength; a discontinuity is considered tangential if this ratio does not exceed 0.3 [Masters et al., 2009].

As most of the crossings used in this study were done by the Juno spacecraft, we used it to estimate whether the magnetopause of Jupiter can be approximated as a tangential discontinuity in most of our cases. We computed the ratio between the mean normal field component and the mean field strength in a time interval of 20 minutes around these crossings. The mean ratio obtained for the normal direction via the Minimum Variance Analysis is 0.332, with a maximum value of 0.987. Around a third of the ratio values exceed the limit value of 0.3, meaning that a tangential discontinuity can approximate the magnetopause for only two-thirds of the crossings (according to the MVA).

However, we already established that the normal direction obtained by the Minimum Variance Analysis is not the most reliable one, and so the above ratio is not necessarily reliable. Consequently, we observed that the methods giving the best results for the normal in the scope of this work are, in order, the Siscoe method, the Constraint method, and the Tangential Discontinuity Analysis. As they are designed especially for tangential discontinuities, this entails that we can approximate the magnetopause as a tangential discontinuity for our crossings list.

6.1.4 Windows

In addition to the comparison between five boundary analysis methods, we also looked at two possible solutions for their windows of application: fixed or optimised. The fixed option is identical to what we found in the literature: it fixes the time window of application of the method at 20 minutes for all methods and all crossings. On the other hand, the optimised option poses a condition evaluating the good definition of the normal, and the windows are different for all methods and all crossings.

We compared the statistical results obtained by both options in Section 4.2.5, and found that the histograms allow us to make the same conclusions on the signs of the angles between the normals. Indeed, we see that the **in** and **out** crossings give two statistically different distributions and that we have a sign inversion between the dawn and dusk sides of the magnetosphere. These observations can be done for the arbitrary windows as well as for the optimised ones, and this allows us to be confident in our results and that our choice of windows did not impact the conclusions on the statistical results.

Nevertheless, we cannot take the shortcut to say that the normal results are precisely the same: depending on the crossings and the considered methods, the vectors obtained through the optimised or fixed options are not equivalent. We observed this difference in the case studies (Chapter 5), where we observed 17 cases of consecutive alternate crossings. We detected oscillations of Siscoe's normals around the model normal in roughly half of those cases. However, the fixed and optimised options allowed the same detection of normal oscillations in only five cases. This emphasises the fragility of the oscillations detection method: the size of the time window used for the computation has an impact on the detection.

As mentioned earlier, the computation time for the optimised methods is greater than that for the arbitrary ones, so if the scope of one's study is to estimate the statistical distributions of the normals rapidly, the arbitrary windows are sufficient. On the other hand, if the principal interest of one's study is to determine the precise orientation of the normals, it is interesting to consider and compare both options.

6.2 Angles between crossings

To determine the existence of wave-like perturbations at the surface of Jupiter's magnetopause and their direction of propagation, we computed the normals to the magnetopause at the crossing positions. Then, we looked at the angles between the normals at consecutive crossings on the dawn sides. We observed two statistically different distributions (for the SIS, BMBS and CSTR normals): one for the angles from an **out** to an **in** crossing and one for the angles from an **in** to an **out** crossing. We wanted to compare these distributions with the ones on the dusk side, but we encountered a problem: we do not have enough consecutive crossings on the dusk side to obtain statistically different distributions.

We had to find another way to look at the variation of the orientation of the normals between the dawn and dusk sides, and we measured the angles between the normals obtained by the different methods and the normal from the model of Joy et al. (2002). In that case, we kept all crossings, not just the consecutive ones, and it allowed us to obtain statistically different distributions for the two sides and all methods. In Section 4.2.4, we examined those histograms for the angles and the results are summarised in Table 6.1. The two distributions are distributed on opposite angle signs, and those signs are inverted when we go from one side of the magnetopause to the other. These results are crucial for discussing the possible disturbances on the surface of Jupiter's magnetopause, which we will do next.

side	angle Joy/in	angle Joy/out
dawn	-	+
dusk	+	-

Table 6.1: Signs of the angles between Joy's normals and the method's normals on both sides of the magnetopause, valid for all methods and both window-size options.

6.3 Perturbations at the magnetopause

As introduced at the beginning of this work, the magnetopause of Jupiter is a deformable surface that various phenomena can perturb. We focus here on three perturbation scenarios: the plasma "fingers" due to the centrifugal interchange instability (similar to the Rayleigh-Taylor instability), the compressions and decompressions of the magnetopause by the solar wind, and the Kelvin-Helmholtz instability. In this section, we are going to look at each scenario and represent schematic wave-like perturbations to illustrate their movements and discuss the potential normal measurement by an imaginary spacecraft traversed by this disturbance.

6.3.1 Centrifugal interchange instability

The so-called plasma "fingers" rotate with Jupiter and graze the magnetopause around the noon sector, meaning that the perturbations created by this phenomenon go from the dawn to the dusk side. Figure 6.2 illustrates the centrifugal interchange scenario: the magnetopause of Jupiter is perturbed by waves going from the dawn to the dusk side. We imagine a stationary spacecraft just outside the magnetopause, and the perturbation of the surface of the boundary traverses it.

Let us describe the crossing made by the imaginary spacecrafts, on the dawn and dusk sides of the magnetopause. Here, the spacecrafts are represented on the outside of the magnetosphere and are considered unmoving, but the passing of the waves at the surface will provoke inwards and outwards crossings.

On the dusk side, the perturbation propagates tailward, and the spacecraft goes through it: it goes out and then in the magnetosphere. At those two crossings, we represented the normal to Joy's magnetopause in black; it represents the normal to the quiet magnetopause. The green and purple arrows are the normals to the perturbed boundary at the **out** and **in** crossings, respectively. The **out** normal is on the right of the model normal, and so the angle (in the XY plane) between the two vectors is negative. On the other hand, the **in** normal is on the left of the model normal, and the angle is therefore positive.

On the dawn side, the perturbation propagates towards the nose of the magnetopause, and the spacecraft goes through it. We have two crossings, inwards

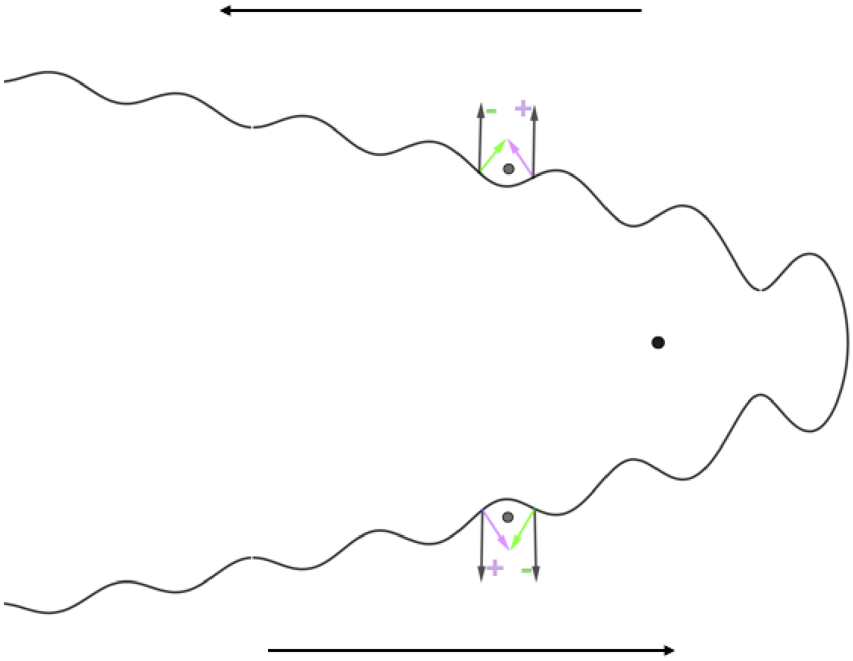

Figure 6.2: Schematic representation of a perturbed magnetopause, in the XY plane with the Sun towards the right of the figure. The waves propagate from dawn to dusk. The black dot represents Jupiter, the grey dot represents an imaginary spacecraft, the black arrows are Joy's normals to the quiet magnetopause, the green arrows are the normals at the **out** crossings, while the purple arrows are the normals at the **in** crossings. The signs are the angles between the model normal and the normal at the perturbed magnetopause. This illustration was done with GeoGebra[2025] and is not to scale.

the magnetosphere and then outwards, and we illustrated those with the model normals and the normals to the perturbed boundary. The **in** normal is on the left of the model normal, and so the angle (in the XY plane) between the two vectors is positive. On the other hand, the **out** normal is on the right of the model normal, and the angle is therefore negative.

We insist here that Figure 6.2 is a schematic representation of the centrifugal interchange instability, and we consider here an imaginary simplified situation to better grasp the impact of the movement of the perturbations on the angles measured.

We summarise the signs of the angles for this phenomenon in Table 6.2, and we compare them to Table 6.1, which is based on our results for the normals computation for all crossings and methods. The signs are separated for the dawn and dusk sides, and the columns contain the angle between the normal to the quiet magnetopause (representing Joy's normal) and the normal to the perturbed magnetopause (representing the normal computed by our methods). We observe in the table that we have two signs for the angles for the **in** and **out** crossings; however, these signs are the same for the dawn and dusk sides. In our statistical results, we found two distributions of opposite signs for the angles at different crossing directions, but we also observed that the signs were inverted between the dawn and dusk sides.

side	angle Joy/in	angle Joy/out
dawn	+	-
dusk	+	-

Table 6.2: Signs of the angles between the normals to the quiet/perturbed magnetopause in the XY plane, for waves propagating from dawn to dusk.

We observe that the centrifugal interchange instability, i.e. the plasma fingers that corotate with Jupiter, is presumably not the principal phenomenon responsible for the magnetopause perturbations we observed in this work. Indeed, MHD simulations of Feng, Binzheng Zhang, et al. (2025) suggest that the effect of this instability would be easier to identify around the noon sector, which is not where we have the bulk of our crossings.

6.3.2 Solar wind interaction

We can focus on the two other scenarios that are dependent on the solar wind. The Kelvin-Helmholtz instability occurs due to a shearing between the solar wind coming to meet the magnetopause and the plasma co-rotating with Jupiter within the magnetosphere. On the other hand, variation of the solar wind dynamic pressure can compress or decompress the boundary, which can create perturbations. In both cases, the wave-like disturbances propagate tailward on the dawn and dusk sides, so we will make the schematic analysis for both at the same time before trying to differentiate the two scenarios.

Schematic analysis

Figure 6.3 illustrates how the perturbations created by the K-H instability or successive compressions/decompressions of the magnetopause propagate and could impact a spacecraft positioned just outside the magnetosphere.

We focus on the crossings made by two imaginary spacecrafts, one on the dawn side and one on the dusk side of the magnetopause. They are represented outside the magnetosphere and considered motionless, but as the oscillating perturbations move the surface, they will provoke inward and outward crossings of the satellites.

On the dusk side, the perturbation propagates tailward, and the spacecraft goes out and then in the magnetosphere. It is the same propagation direction as for the previous scenario. The **out** normal is on the right of the model normal, and so the angle (in the XY plane) between the two vectors is negative. On the other hand, the **in** normal is on the left of the model normal, and the angle is therefore positive.

On the dawn side, the perturbation propagates towards the tail of the magnetosphere, and the spacecraft goes through it. We have two crossings, inwards the magnetosphere and then outwards, and we illustrated the model normals and the

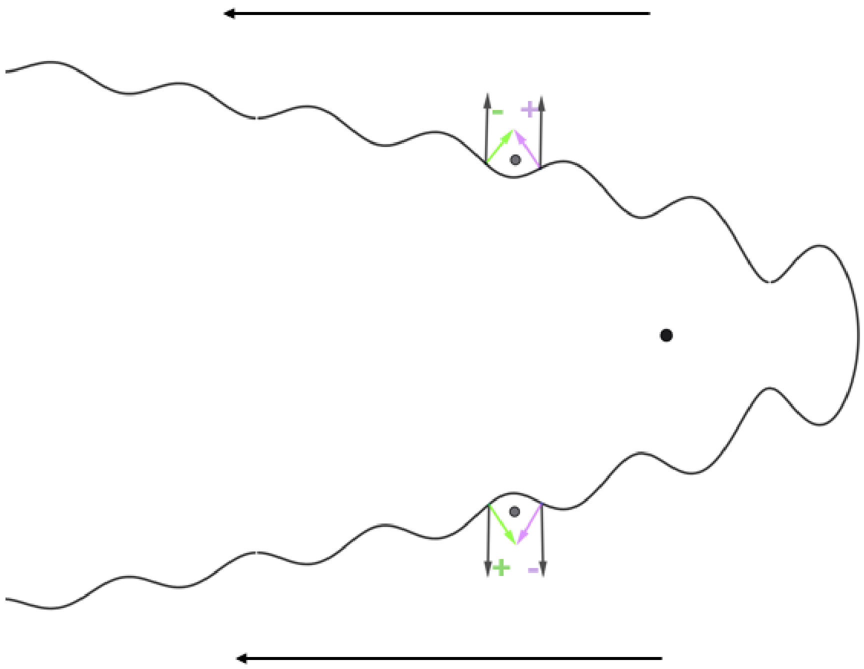

Figure 6.3: Schematic representation of a perturbed magnetopause, in the XY plane with the Sun towards the right of the figure. The waves propagate towards the tail of the magnetopause, on the dawn and dusk sides. The black dot represents Jupiter, the grey dot represents an imaginary spacecraft, the black arrows are Joy's normals to the quiet magnetopause, the green arrows are the normals at the **out** crossings, while the purple arrows are the normals at the **in** crossings. The signs are the angles between the model normal and the normal at the perturbed magnetopause. This illustration was done with GeoGebra[2025] and is not to scale.

normals to the perturbed boundary at those points. We then take a closer look at the signs of the angle between the quiet and perturbed magnetopause normals at each crossing. The **in** normal is on the right of the model normal, and so the angle (in the XY plane) between the two vectors is negative. On the other hand, the **out** normal is on the left of the model normal, and the angle is therefore positive.

As before, we must insist that Figure 6.3 is a schematic representation of the magnetopause perturbed by the solar wind (K-H instability or successive (de)compression), and we consider here an imaginary simplified situation.

The situation in the presence of tailward propagating waves is summarised in Table 6.3, which contains the signs of the angles on the dawn and dusk sides of the magnetopause. We compare this table with Table 6.1, based on our results for the normals computation for all crossings and methods.

The signs are separated for the dawn and dusk sides, and the columns contain the angle between the normal to the quiet magnetopause (representing Joy's normal) and the normal to the perturbed magnetopause (representing the normal computed by our methods). By focusing separately on the dawn and dusk sides, we see that the signs are opposed for the angles on the **in** and **out** crossings. If we compare the angles for the **in** crossings, we see that there is a sign inversion between the dawn and dusk sides, and the same observation can be made for the **out** crossings. The signs examined here are the same as the ones on Table 6.1 containing the results of our computations.

side	angle Joy/in	angle Joy/out
dawn	-	+
dusk	+	-

Table 6.3: Signs of the angles between the normals to the quiet and perturbed magnetopause in the XY plane, for waves propagating towards the tail.

We can conclude from this section that the sign inversion we observed from dawn to dusk in our statistical results is presumably an indication of tailward propagating waves due to the interaction of the magnetopause with the solar wind, in the form of Kelvin-Helmholtz instabilities or successive (de)compressions of the boundary.

Kelvin-Helmholtz instability or compression/decompression

In our statistical results, we observed a dawn-dusk inversion of the sign of the angle between the methods and the model normals. We concluded above that this was evidence that the crossings analysed in this work lead to the detection of wave-like perturbations mainly propagating towards the tail.

After studying the statistical results, we tried to detect cases of consecutive alternate crossings in our results: alternative **in** and **out** crossings within three hours of each other. We observed 17 such cases and found that oscillations of the normal around the model in seven of them: three cases for Galileo and four for Juno, and we examined one for each side of the magnetosphere in Section 5. We observed flipping of the normals around the model normal of Joy et al. (2002): the consecutive **in** and **out** normals are on either side of the model normal. Therefore, the signs of the angles between the model and method normals are opposite for the **in** and **out** crossing, and we also observed the dawn-dusk inversion of those signs between the two studied cases.

As discussed previously, the most probable driving mechanisms for such tailward propagating waves are the Kelvin-Helmholtz instability and the possible fluctuations in the dynamic pressure of the solar wind.

In the case of a variation of solar wind dynamic pressure, the fluctuations provoke compression and decompression of the magnetosphere, with the magnetopause moving inward and outward to achieve those different states. This was observed at Jupiter by Kurth et al. (2002), who noticed **a single magnetopause crossing** via the Galileo and Cassini missions at nearly the same time, and it was associated with the compression of the magnetopause by the solar wind. Indeed, if the Kelvin-Helmholtz instability were responsible, it would have created small-amplitude periodic motions of the boundary and multiple crossings.

On the other hand, we can note that Masters et al. (2009) and Cutler et al. (2011) examined the evidence of surface waves driven by the Kelvin-Helmholtz instability, on the dawn and dusk side of Saturn's magnetopause, respectively. These two articles considered **sets of consecutive crossings** on which the Minimum Variance Analysis (MVA) is applied, and the cross-product (TDA) method is used to estimate whether the normal obtained by the MVA is correctly identified. Then they determined a flipping direction and measured the angles between that direction and the obtained normals for each crossing of the set, which showed oscillations between positive and negative signs. Indeed, they identified tailward propagating surface waves on Saturn's magnetopause, and concluded that the K-H instability is the most plausible mechanism for generating those waves.

In light of these observations, the fact that we have consecutive crossings on short time scales, with normals flipping around the model normal and associated with a tailward propagation, allows us to assume that we detect cases of oscillations due to the Kelvin-Helmholtz instability.

It is, of course, essential to be nuanced: we cannot affirm that all measured perturbations are driven by the Kelvin-Helmholtz instability, and we may have a coexistence of wave-like perturbations induced by the three different mechanisms.

6.4 Complex boundary

As shown by three-dimensional MHD simulations of the Jovian magnetosphere (see supporting information of Feng, Binzheng Zhang, et al. (2025)), the magnetopause is a complex and highly dynamic boundary layer, shaped by multiple perturbing processes. In the previous illustrations, we considered the simplified case of a magnetopause perturbed by sinusoidal oscillations. In reality, however, instabilities such as centrifugal interchange and Kelvin–Helmholtz, together with fluctuations in the solar wind dynamic pressure, are likely to act simultaneously, producing boundary deformations far more complex than a simple sine wave.

Despite this, our statistical analysis of the angles between Joy's model normal and the normals obtained by the different methods consistently indicates tailward-propagating perturbations. This result is robust: it is confirmed across all five methods and holds for both window-size options, giving us confidence in its reliability. The prevalence of tailward-propagating perturbations suggests that the dominant driver is the interaction with the solar wind. This interpretation is consistent with simulations, which show that centrifugal interchange instability is most evident near the noon sector—outside the region where the majority of our crossings were observed.

Solar wind dynamic pressure is expected to vary over the course of the missions, some of which spanned several years. Such variations typically generate large-scale "folds" in the magnetopause surface that also propagate tailward. However, statistical considerations make it more likely for spacecraft to encounter perturbations associated with Kelvin–Helmholtz instabilities, characterised by smalleramplitude, periodic boundary oscillations.

When analysing consecutive alternate crossings, we compared method-derived normals with the model normal. The Siscoe method was used preferentially, as it consistently provided the most reliable results and always agreed with at least one other method. Oscillations of the Siscoe normal around Joy's model normal were detected, which can plausibly be attributed to Kelvin–Helmholtz instability. However, agreement between the two window-size options was less clear at the level of individual cases: depending on whether fixed or optimised windows were applied, oscillations were either observed or absent.

Finally, it is important to note that in the case of Jupiter, we are restricted to single-spacecraft measurements. This limitation reduces both the precision with which perturbations can be identified and the degree to which they can be characterised.

In summary, using only magnetic field data from single-spacecraft measurements, we obtained statistically robust evidence of globally tailward-propagating magnetopause perturbations. However, at the level of individual events, even with multiple methods and window-size options, it is difficult to determine with certainty the true local normal to the boundary, which hinders the precise characterisation of the wave-like perturbations.

Conclusion & Perspectives

In this master's thesis, we investigated wave phenomena on Jupiter's magnetopause and sought to identify the processes responsible for perturbations of the boundary. In particular, we considered three possible drivers: centrifugal interchange instability, Kelvin–Helmholtz instability, and fluctuations in the solar wind dynamic pressure.

To address this problem, we computed the magnetopause normal using different methods and window-size options, comparing the results to assess their reliability. Among the tested approaches, the Siscoe method emerged as the most robust within the scope of this study, as it consistently agreed with at least one other method. This finding is noteworthy, since the Minimum Variance Analysis is more commonly employed in studies of boundary normals.

Our statistical analysis of the normal orientations relative to the probabilistic magnetopause model of Joy et al. (2002) provided strong evidence for tailward-propagating perturbations, a result that was consistent across all methods and window-size options. Such wave-like disturbances are most plausibly linked to solar wind interactions, either through Kelvin–Helmholtz instability or through variations in the solar wind dynamic pressure. While dynamic pressure variations can generate large-scale "folds" propagating tailward along the magnetopause, such signatures are less likely to be detected, especially by a single spacecraft.

We also examined consecutive alternate crossings and, in some cases, observed oscillations of the Siscoe normal around Joy's model normal. These oscillatory signatures are compatible with Kelvin–Helmholtz instability. However, unlike the statistical results, these case studies are less conclusive: the oscillations were not consistently identified across all methods and window-size options.

Overall, this work demonstrates that with magnetic field data from a single spacecraft, it is possible to obtain statistically reliable evidence of tailward-propagating perturbations at Jupiter's magnetopause. However, at the level of individual events, even when multiple methods and window-size options are applied, the precise orientation of the local boundary normal remains uncertain.

A promising direction for future work is the use of three-dimensional MHD simulations of the Jovian magnetosphere. By placing synthetic spacecraft within these simulations, one could examine how different perturbations affect the magnetic field, thereby improving our ability to characterise and distinguish between instability-driven signatures in in-situ data.

Finally, it is worth noting that magnetopause boundary waves have already been investigated at Earth and Saturn. A comparative study of the corresponding signatures could provide valuable insights, helping to refine our understanding of the phenomenon at Jupiter and enhancing detection strategies in future missions.

Appendix A

SPICE kernels list

Table A.1: List of the kernels used in the frame of this master's thesis. The general, frame and trajectory kernels are listed.

FILE	DESCRIPTION
`naif0012.tls.pc`	leapsecond
`pck00010.tpc`	planetary constants
`de430.bsp`	ephemeris for planetary bodies
`jup344-s2003_j24.bsp`	Jupiter's specific ephemeris data
`jup_mission.tf`	Jupiter Missions reference frame
`SUN_IHG.tf`	inertial heliographic frame
`VG1_IHG_RTN.tf`	VG1 inertial heliographic RTN frame
`VG2_IHG_RTN.tf`	VG2 inertial heliographic RTN frame
`JUP_S3.tf`	System III reference frame
`JUNO_JSS.tf`	Juno JSS frame
`Voyager_1.a54206u_V0.2_merged.bsp`	VG1's trajectory
`Voyager_2.m05016u.merged.bsp`	VG2's trajectory
`gll_951120_021126_raj2021.bsp`	GLL's trajectory
`ulysses_1990_2009_2050.bsp`	UL's trajectory
`p10-a.bsp`	P10's trajectory
`p11-a.bsp`	P11's trajectory
`spk_rec_160522_160729_160909.bsp`	Juno's trajectory
`spk_rec_160729_160923_161027.bsp`	Juno's trajectory
`spk_rec_160923_161115_161121.bsp`	Juno's trajectory
`spk_rec_161115_170106_170113.bsp`	Juno's trajectory
`spk_rec_170106_170228_170307.bsp`	Juno's trajectory
`spk_rec_170228_170422_170427.bsp`	Juno's trajectory
`spk_rec_170422_170608_170621.bsp`	Juno's trajectory
`spk_rec_170608_170728_170803.bsp`	Juno's trajectory
`spk_rec_170728_170918_170922.bsp`	Juno's trajectory
`spk_rec_170918_171121_171127.bsp`	Juno's trajectory
`spk_rec_171121_180113_180117.bsp`	Juno's trajectory
`spk_rec_180113_180307_180312.bsp`	Juno's trajectory

FILE	DESCRIPTION
`spk_rec_180307_180429_180504.bsp`	Juno’s trajectory
`spk_rec_180429_180621_180626.bsp`	Juno’s trajectory
`spk_rec_180620_180812_180821.bsp`	Juno’s trajectory
`spk_rec_180812_181004_181011.bsp`	Juno’s trajectory
`spk_rec_181004_181126_181205.bsp`	Juno’s trajectory
`spk_rec_181126_190118_190124.bsp`	Juno’s trajectory
`spk_rec_190118_190312_190319.bsp`	Juno’s trajectory
`spk_rec_190312_190504_190509.bsp`	Juno’s trajectory
`spk_rec_190504_190626_190627.bsp`	Juno’s trajectory
`spk_rec_190626_190817_190822.bsp`	Juno’s trajectory
`spk_rec_190817_191010_191022.bsp`	Juno’s trajectory
`spk_rec_191010_191201_191210.bsp`	Juno’s trajectory
`spk_rec_191201_200124_200129.bsp`	Juno’s trajectory
`spk_rec_200124_200316_200324.bsp`	Juno’s trajectory
`spk_rec_200316_200508_200512.bsp`	Juno’s trajectory
`spk_rec_200508_200629_200709.bsp`	Juno’s trajectory
`spk_rec_200629_200822_200826.bsp`	Juno’s trajectory
`spk_rec_200822_201014_201016.bsp`	Juno’s trajectory
`spk_rec_201014_201205_201208.bsp`	Juno’s trajectory
`spk_rec_201205_210127_210210.bsp`	Juno’s trajectory
`spk_rec_210127_210321_210329.bsp`	Juno’s trajectory
`spk_rec_210321_210513_210517.bsp`	Juno’s trajectory
`spk_rec_210513_210630_210707.bsp`	Juno’s trajectory
`spk_rec_210630_210813_210825.bsp`	Juno’s trajectory
`spk_rec_210813_210925_211005.bsp`	Juno’s trajectory
`spk_rec_210925_211108_211115.bsp`	Juno’s trajectory
`spk_rec_211108_211222_220104.bsp`	Juno’s trajectory
`spk_rec_211222_220204_220210.bsp`	Juno’s trajectory
`spk_rec_220204_220319_220330.bsp`	Juno’s trajectory
`spk_rec_220319_220502_220510.bsp`	Juno’s trajectory
`spk_rec_220502_220614_220622.bsp`	Juno’s trajectory
`spk_rec_220614_220728_220805.bsp`	Juno’s trajectory
`spk_rec_220728_220909_220913.bsp`	Juno’s trajectory
`spk_rec_220909_221019_221027.bsp`	Juno’s trajectory
`spk_rec_221019_221127_221208.bsp`	Juno’s trajectory
`spk_rec_221127_230104_230111.bsp`	Juno’s trajectory
`spk_rec_230104_230211_230221.bsp`	Juno’s trajectory
`spk_rec_230211_230321_230327.bsp`	Juno’s trajectory
`spk_rec_230321_230428_230504.bsp`	Juno’s trajectory
`spk_rec_230428_230605_230613.bsp`	Juno’s trajectory
`spk_rec_230605_230713_230720.bsp`	Juno’s trajectory
`spk_rec_230713_230820_230823.bsp`	Juno’s trajectory
`spk_rec_230820_230927_231003.bsp`	Juno’s trajectory
`spk_rec_230927_231104_231109.bsp`	Juno’s trajectory

FILE	DESCRIPTION
`spk_rec_231104_231212_231220.bsp`	Juno's trajectory
`spk_rec_231212_240118_240119.bsp`	Juno's trajectory
`spk_rec_240118_240221_240226.bsp`	Juno's trajectory
`spk_rec_240221_240325_240401.bsp`	Juno's trajectory
`spk_rec_240325_240426_240430.bsp`	Juno's trajectory
`spk_rec_240426_240529_240605.bsp`	Juno's trajectory
`spk_rec_240529_240701_240705.bsp`	Juno's trajectory
`spk_rec_240701_240802_240814.bsp`	Juno's trajectory
`spk_rec_240802_240904_240910.bsp`	Juno's trajectory
`spk_rec_240904_241007_241014.bsp`	Juno's trajectory
`spk_rec_241007_241109_241119.bsp`	Juno's trajectory
`spk_rec_241109_241211_241218.bsp`	Juno's trajectory
`spk_rec_241211_250113_250116.bsp`	Juno's trajectory
`spk_rec_250113_250215_250219.bsp`	Juno's trajectory

Appendix B

Crossings list

Table B.1: Information about the magnetopause crossings by the Pioneer 10 and 11, Voyager 1 and 2, Ulysses, Galileo, and Juno missions: the precise date and time, the direction of the crossing, and its position in the *Jupiter Missions* frame.

S/C	**DATE**	**TIME**	**IN/OUT**	**X** (R_J)	**Y** (R_J)	**Z** (R_J)
P10	1973-11-27	19:53:00	in	78.858	-54.139	-10.183
P10	1973-12-01	02:33:00	in	45.405	-26.517	-6.502
P10	1973-12-01	13:36:00	in	40.255	-22.319	-5.917
P10	1973-12-10	11:53:00	out	-16.079	-95.266	14.67
P10	1973-12-12	09:43:00	out	-17.947	-118.611	17.75
P10	1973-12-12	09:58:00	out	-17.957	-118.736	17.767
P10	1973-12-14	18:50:00	out	-20.331	-146.815	21.459
P11	1974-11-27	02:46:00	in	71.668	-64.136	-13.409
P11	1974-11-27	07:52:00	in	69.502	-62.412	-13.181
P11	1974-11-29	13:19:00	in	46.149	-43.601	-10.651
P11	1974-12-06	08:07:00	out	47.617	-4.005	30.24
P11	1974-12-06	18:28:00	out	52.967	-5.018	33.11
P11	1974-12-08	00:36:00	out	68.001	-7.952	41.133
VG1	1979-03-01	19:56:00	in	63.479	-20.8	2.235
VG1	1979-03-02	07:54:00	in	56.454	-17.206	1.853
VG1	1979-03-02	14:30:00	in	52.509	-15.197	1.64
VG1	1979-03-02	20:03:00	in	49.144	-13.491	1.459
VG1	1979-03-02	20:45:00	in	48.717	-13.274	1.436
VG1	1979-03-02	21:12:00	in	48.441	-13.135	1.422
VG1	1979-03-02	21:53:00	in	48.022	-12.924	1.399
VG1	1979-03-02	22:28:00	in	47.664	-12.743	1.38
VG1	1979-03-03	02:27:00	in	45.202	-11.503	1.249
VG1	1979-03-15	09:30:00	out	-68.029	-141.948	14.687
VG1	1979-03-15	17:00:00	out	-69.693	-146.036	15.111
VG1	1979-03-15	21:19:00	out	-70.65	-148.384	15.355
VG2	1979-07-05	01:10:00	in	63.937	-29.533	7.002

following on the next page

DATE	**TIME**	**IN/OUT**	**SC**			
VG2	1979-07-05	18:40:00	in	56.898	-23.572	5.801
VG2	1979-07-24	01:35:00	out	-124.656	-119.577	14.57
VG2	1979-07-24	05:31:00	out	-125.767	-120.907	14.746
VG2	1979-07-24	05:57:00	out	-125.89	-121.054	14.765
VG2	1979-07-24	09:27:00	out	-126.877	-122.236	14.921
VG2	1979-07-25	00:52:00	out	-131.218	-127.422	15.604
VG2	1979-07-25	04:10:00	out	-132.146	-128.529	15.75
VG2	1979-07-27	18:20:00	out	-149.524	-149.134	18.475
VG2	1979-08-01	15:17:00	out	-181.929	-186.867	23.495
VG2	1979-08-02	02:22:00	out	-184.991	-190.383	23.964
VG2	1979-08-02	07:22:00	out	-186.372	-191.966	24.176
VG2	1979-08-03	06:11:00	out	-192.673	-199.167	25.139
VG2	1979-08-03	07:57:00	out	-193.16	-199.723	25.213
UL	1992-02-02	23:08:00	in	97.43	-46.812	11.991
UL	1992-02-03	17:20:00	in	84.641	-42.026	11.409
UL	1992-02-03	19:45:00	in	82.933	-41.384	11.33
UL	1992-02-04	00:25:00	in	79.629	-40.138	11.177
UL	1992-02-04	01:00:00	in	79.215	-39.982	11.158
UL	1992-02-04	01:25:00	in	78.919	-39.87	11.144
UL	1992-02-04	04:00:00	in	77.084	-39.177	11.058
UL	1992-02-12	00:24:00	out	-9.211	57.618	-42.619
UL	1992-02-12	01:00:00	out	-9.197	57.983	-42.907
UL	1992-02-12	10:58:00	out	-8.963	64.005	-47.661
UL	1992-02-12	12:26:00	out	-8.927	64.886	-48.357
UL	1992-02-12	13:57:00	out	-8.89	65.796	-49.076
UL	1992-02-12	17:40:00	out	-8.797	68.021	-50.833
UL	1992-02-12	19:10:00	out	-8.759	68.917	-51.541
UL	1992-02-14	10:30:00	out	-7.671	92.095	-69.864
UL	1992-02-14	14:00:00	out	-7.567	94.134	-71.476
UL	1992-02-14	16:00:00	out	-7.507	95.297	-72.397
UL	1992-02-14	18:15:00	out	-7.439	96.605	-73.431
UL	1992-02-14	18:25:00	out	-7.434	96.702	-73.507
UL	1992-02-14	21:40:00	out	-7.335	98.588	-75.0
GLL	1996-05-24	20:07:00	out	-72.815	-166.998	-20.428
GLL	1996-05-25	07:52:00	in	-71.782	-165.921	-20.269
GLL	1996-05-25	11:09:00	out	-71.492	-165.618	-20.224
GLL	1996-05-26	02:28:00	in	-70.128	-164.185	-20.013
GLL	1996-05-26	12:38:00	out	-69.214	-163.219	-19.871
GLL	1996-05-29	14:51:00	in	-62.336	-155.784	-18.782
GLL	1996-05-29	15:48:00	out	-62.246	-155.685	-18.768
GLL	1996-05-29	17:20:00	in	-62.1	-155.523	-18.744
GLL	1996-05-30	07:25:00	in	-60.749	-154.027	-18.526
GLL	1996-05-30	07:53:00	out	-60.704	-153.977	-18.519

following on the next page

DATE	**TIME**	**IN/OUT**	**SC**			
GLL	1996-05-30	08:21:00	in	-60.659	-153.927	-18.512
GLL	1996-05-30	17:33:00	out	-59.769	-152.934	-18.367
GLL	1996-05-31	14:37:00	out	-57.707	-150.614	-18.031
GLL	1996-06-01	01:32:00	in	-56.626	-149.387	-17.853
GLL	1996-06-01	07:07:00	in	-56.069	-148.752	-17.762
GLL	1996-06-01	07:51:00	out	-55.996	-148.668	-17.75
GLL	1996-06-01	08:01:00	in	-55.979	-148.649	-17.747
GLL	1996-06-01	08:41:00	in	-55.913	-148.573	-17.736
GLL	2000-05-28	03:07:00	out	15.308	69.846	-1.907
GLL	2000-05-28	05:06:00	out	15.233	70.45	-1.913
GLL	2000-05-28	08:42:00	out	15.095	71.538	-1.924
GLL	2000-05-30	16:45:00	in	12.783	87.263	-2.07
GLL	2000-06-03	17:50:00	out	8.457	110.498	-2.241
GLL	2000-06-05	18:57:00	in	6.249	120.86	-2.304
GLL	2000-06-06	06:00:00	out	5.755	123.086	-2.316
GLL	2000-06-12	08:22:00	out	-0.596	149.642	-2.444
GLL	2000-11-30	15:22:00	in	-50.928	164.361	0.013
GLL	2000-12-01	06:03:00	out	-50.82	162.205	0.044
GLL	2000-12-01	06:48:00	in	-50.814	162.095	0.046
GLL	2000-12-04	19:01:00	out	-50.073	149.073	0.23
GLL	2000-12-04	20:34:00	in	-50.058	148.822	0.234
GLL	2000-12-04	21:13:00	out	-50.051	148.717	0.235
GLL	2000-12-06	17:40:00	in	-49.556	141.341	0.335
GLL	2000-12-08	12:14:00	out	-49.002	133.925	0.432
GLL	2000-12-12	09:40:00	in	-47.422	116.255	0.648
GLL	2000-12-13	10:51:00	out	-46.886	111.117	0.707
GLL	2000-12-13	11:41:00	in	-46.868	110.944	0.708
GLL	2001-01-10	20:51:00	out	40.591	93.638	-0.842
GLL	2001-10-20	06:06:00	out	45.114	21.011	-1.467
GLL	2001-10-20	08:57:00	in	45.782	21.759	-1.487
GLL	2001-10-22	11:01:00	out	55.823	33.982	-1.773
GLL	2001-10-22	12:51:00	in	56.142	34.4	-1.781
GLL	2001-10-23	10:29:00	out	59.694	39.192	-1.879
GLL	2001-10-23	20:24:00	in	61.208	41.308	-1.92
GLL	2001-10-24	04:01:00	out	62.327	42.902	-1.951
GLL	2001-10-24	11:32:00	in	63.396	44.448	-1.979
GLL	2001-10-24	16:52:00	out	64.134	45.53	-1.999
GLL	2001-10-26	19:58:00	in	70.462	55.3	-2.163
GLL	2001-10-27	16:37:00	in	72.691	58.972	-2.219
GLL	2001-10-28	05:13:00	out	73.971	61.141	-2.251
GLL	2001-10-28	17:11:00	out	75.134	63.154	-2.279
GLL	2001-10-28	19:33:00	in	75.359	63.547	-2.285
GLL	2001-10-28	23:34:00	out	75.735	64.209	-2.294

following on the next page

DATE	**TIME**	**IN/OUT**	**SC**			
GLL	2002-01-04	12:36:00	in	36.262	93.579	-0.651
GLL	2002-01-05	08:24:00	out	33.815	90.709	-0.589
GLL	2002-01-07	04:57:00	out	28.037	83.605	-0.446
GLL	2002-01-08	03:18:00	in	24.988	79.657	-0.372
GLL	2002-01-23	04:41:00	out	60.132	17.561	-1.573
GLL	2002-10-27	06:10:00	in	69.435	58.357	-1.468
GLL	2002-10-27	12:28:00	in	67.976	57.471	-1.44
GLL	2002-10-27	15:42:00	out	67.221	57.011	-1.426
GLL	2002-10-27	23:25:00	in	65.398	55.898	-1.392
GLL	2002-10-28	04:35:00	out	64.162	55.141	-1.369
GLL	2002-10-28	05:45:00	in	63.881	54.969	-1.364
GLL	2002-10-31	21:05:00	out	40.482	40.12	-0.925
GLL	2002-11-01	16:46:00	in	34.33	35.987	-0.808
JUNO	2016-07-14	21:18:00	out	2.555	-80.744	-14.323
JUNO	2016-07-15	07:16:00	in	2.552	-82.466	-14.252
JUNO	2016-07-15	17:06:00	out	2.545	-84.104	-14.172
JUNO	2016-07-15	19:11:00	in	2.543	-84.443	-14.154
JUNO	2016-07-16	23:07:00	out	2.504	-88.748	-13.869
JUNO	2016-07-19	17:26:00	in	2.317	-97.306	-12.94
JUNO	2016-07-19	20:43:00	out	2.305	-97.674	-12.887
JUNO	2016-07-20	09:18:00	in	2.256	-99.039	-12.675
JUNO	2016-07-20	19:16:00	out	2.215	-100.07	-12.501
JUNO	2016-07-21	01:49:00	in	2.186	-100.724	-12.384
JUNO	2016-07-21	02:02:00	out	2.185	-100.745	-12.38
JUNO	2016-07-22	14:31:00	in	2.013	-104.049	-11.686
JUNO	2016-07-23	14:06:00	out	1.888	-105.894	-11.204
JUNO	2016-07-23	19:54:00	in	1.857	-106.314	-11.082
JUNO	2016-07-24	18:47:00	out	1.726	-107.843	-10.588
JUNO	2016-07-25	01:12:00	in	1.688	-108.235	-10.446
JUNO	2016-07-25	14:33:00	out	1.608	-109.002	-10.145
JUNO	2016-07-30	00:22:00	in	0.911	-112.778	-7.568
JUNO	2016-08-01	19:36:00	out	0.435	-113.115	-5.786
JUNO	2016-08-01	20:57:00	in	0.425	-113.106	-5.749
JUNO	2016-08-01	21:55:00	out	0.418	-113.099	-5.723
JUNO	2016-08-02	08:13:00	in	0.345	-113.002	-5.441
JUNO	2016-08-02	10:50:00	out	0.326	-112.972	-5.37
JUNO	2016-08-02	13:59:00	in	0.303	-112.932	-5.283
JUNO	2016-08-02	22:12:00	out	0.245	-112.811	-5.057
JUNO	2016-08-02	22:49:00	in	0.24	-112.801	-5.04
JUNO	2016-08-06	19:56:00	out	-0.412	-109.73	-2.409
JUNO	2016-08-06	23:50:00	in	-0.439	-109.532	-2.297
JUNO	2016-08-07	01:20:00	out	-0.449	-109.455	-2.254
JUNO	2016-08-08	08:44:00	in	-0.657	-107.635	-1.346

following on the next page

DATE	**TIME**	**IN/OUT**	**SC**			
JUNO	2016-08-08	14:35:00	out	-0.695	-107.254	-1.177
JUNO	2016-08-08	15:26:00	in	-0.7	-107.197	-1.152
JUNO	2016-08-08	15:38:00	out	-0.702	-107.184	-1.146
JUNO	2016-08-11	17:12:00	in	-1.143	-101.182	0.995
JUNO	2016-08-11	23:25:00	out	-1.177	-100.57	1.176
JUNO	2016-08-12	03:56:00	in	-1.201	-100.114	1.307
JUNO	2016-08-12	10:05:00	out	-1.234	-99.479	1.485
JUNO	2016-08-12	12:39:00	in	-1.247	-99.209	1.56
JUNO	2016-08-12	21:11:00	out	-1.291	-98.29	1.807
JUNO	2016-08-12	23:55:00	in	-1.305	-97.988	1.886
JUNO	2016-09-06	11:02:00	out	-3.099	-81.062	-15.752
JUNO	2016-09-06	21:47:00	in	-3.232	-82.883	-15.703
JUNO	2016-09-07	03:15:00	out	-3.299	-83.782	-15.673
JUNO	2016-09-08	23:56:00	in	-3.842	-90.475	-15.309
JUNO	2016-09-14	22:50:00	out	-5.469	-105.314	-13.11
JUNO	2016-09-16	21:51:00	in	-5.956	-108.33	-12.137
JUNO	2016-09-19	07:05:00	out	-6.504	-110.885	-10.83
JUNO	2016-09-19	20:41:00	in	-6.627	-111.317	-10.502
JUNO	2016-09-20	07:05:00	out	-6.718	-111.603	-10.247
JUNO	2016-09-20	13:20:00	in	-6.772	-111.756	-10.092
JUNO	2016-09-22	02:28:00	out	-7.078	-112.382	-9.146
JUNO	2016-09-22	09:40:00	in	-7.134	-112.448	-8.958
JUNO	2016-09-23	18:09:00	out	-7.372	-112.516	-8.091
JUNO	2016-09-23	21:05:00	in	-7.393	-112.504	-8.012
JUNO	2016-09-28	01:35:00	out	-7.958	-110.254	-5.169
JUNO	2016-09-29	13:05:00	in	-8.088	-108.586	-4.119
JUNO	2016-09-30	13:17:00	out	-8.152	-107.177	-3.393
JUNO	2016-09-30	16:36:00	in	-8.159	-106.966	-3.293
JUNO	2016-10-01	03:54:00	out	-8.181	-106.216	-2.95
JUNO	2016-10-01	05:40:00	in	-8.184	-106.094	-2.897
JUNO	2016-10-01	17:48:00	out	-8.201	-105.224	-2.528
JUNO	2016-10-01	21:44:00	in	-8.205	-104.93	-2.408
JUNO	2016-10-02	01:04:00	out	-8.208	-104.675	-2.306
JUNO	2016-10-04	04:36:00	in	-8.196	-100.15	-0.72
JUNO	2016-11-07	23:46:00	out	-12.981	-105.566	-14.67
JUNO	2016-11-08	09:02:00	in	-13.118	-106.146	-14.488
JUNO	2016-11-08	11:31:00	out	-13.154	-106.295	-14.438
JUNO	2016-11-09	17:32:00	in	-13.571	-107.921	-13.815
JUNO	2016-11-09	18:09:00	out	-13.579	-107.951	-13.802
JUNO	2016-11-13	08:28:00	in	-14.569	-110.776	-11.784
JUNO	2016-11-13	15:08:00	out	-14.632	-110.884	-11.615
JUNO	2016-11-13	19:55:00	in	-14.676	-110.952	-11.494
JUNO	2016-11-13	21:40:00	out	-14.692	-110.975	-11.449

following on the next page

DATE	TIME	IN/OUT	SC			
JUNO	2016-11-14	00:45:00	in	-14.72	-111.012	-11.37
JUNO	2016-11-14	05:04:00	out	-14.758	-111.059	-11.258
JUNO	2016-11-14	10:55:00	in	-14.808	-111.112	-11.106
JUNO	2016-11-19	06:12:00	out	-15.462	-109.71	-7.889
JUNO	2016-11-19	11:24:00	in	-15.475	-109.535	-7.735
JUNO	2016-11-21	22:39:00	out	-15.522	-106.85	-5.933
JUNO	2016-11-24	04:01:00	in	-15.381	-103.291	-4.245
JUNO	2016-11-25	12:22:00	out	-15.201	-100.576	-3.197
JUNO	2016-11-25	12:54:00	in	-15.198	-100.527	-3.18
JUNO	2016-11-25	13:13:00	out	-15.196	-100.498	-3.169
JUNO	2016-11-25	13:16:00	in	-15.195	-100.494	-3.168
JUNO	2016-11-25	13:29:00	out	-15.194	-100.474	-3.161
JUNO	2016-11-25	14:40:00	in	-15.186	-100.366	-3.122
JUNO	2016-11-25	14:52:00	out	-15.184	-100.347	-3.115
JUNO	2016-11-25	17:40:00	in	-15.165	-100.089	-3.024
JUNO	2016-11-25	20:44:00	out	-15.143	-99.801	-2.923
JUNO	2016-11-26	06:15:00	in	-15.069	-98.884	-2.611
JUNO	2016-12-19	01:50:00	out	-11.577	-67.448	-18.29
JUNO	2016-12-19	07:14:00	in	-11.805	-68.591	-18.362
JUNO	2016-12-19	08:47:00	out	-11.87	-68.915	-18.381
JUNO	2016-12-19	14:12:00	in	-12.095	-70.03	-18.444
JUNO	2016-12-21	08:48:00	out	-13.75	-78.032	-18.747
JUNO	2016-12-21	15:37:00	in	-13.998	-79.196	-18.767
JUNO	2016-12-22	06:05:00	out	-14.51	-81.57	-18.787
JUNO	2016-12-22	06:08:00	in	-14.512	-81.578	-18.787
JUNO	2016-12-22	06:10:00	out	-14.513	-81.583	-18.787
JUNO	2016-12-22	09:09:00	in	-14.616	-82.057	-18.788
JUNO	2016-12-31	11:38:00	out	-20.338	-104.823	-16.42
JUNO	2016-12-31	18:00:00	in	-20.456	-105.186	-16.297
JUNO	2017-01-01	04:26:00	out	-20.642	-105.748	-16.092
JUNO	2017-01-01	09:23:00	in	-20.728	-106.001	-15.993
JUNO	2017-01-01	16:39:00	out	-20.852	-106.355	-15.844
JUNO	2017-01-01	22:09:00	in	-20.943	-106.61	-15.73
JUNO	2017-01-02	13:47:00	out	-21.191	-107.276	-15.397
JUNO	2017-01-04	18:27:00	in	-21.907	-108.878	-14.184
JUNO	2017-01-11	10:22:00	out	-22.897	-107.81	-9.782
JUNO	2017-01-13	03:18:00	in	-22.838	-106.087	-8.51
JUNO	2017-01-24	20:01:00	out	-17.804	-75.215	1.265
JUNO	2017-01-24	20:36:00	in	-17.782	-75.107	1.286
JUNO	2017-01-24	21:18:00	out	-17.756	-74.976	1.311
JUNO	2017-01-24	22:38:00	in	-17.705	-74.727	1.36
JUNO	2017-01-25	00:23:00	out	-17.639	-74.398	1.423
JUNO	2017-01-25	17:53:00	in	-16.938	-70.976	2.054

following on the next page

DATE	TIME	IN/OUT	SC			
JUNO	2017-02-11	01:42:00	out	-17.487	-71.735	-20.041
JUNO	2017-02-11	19:08:00	in	-18.377	-74.913	-20.219
JUNO	2017-02-19	04:33:00	out	-25.315	-97.531	-19.645
JUNO	2017-02-19	04:50:00	in	-25.323	-97.555	-19.642
JUNO	2017-02-19	06:01:00	out	-25.358	-97.657	-19.627
JUNO	2017-02-19	10:15:00	in	-25.483	-98.015	-19.574
JUNO	2017-02-19	10:50:00	out	-25.5	-98.064	-19.566
JUNO	2017-02-22	04:21:00	in	-27.212	-102.698	-18.565
JUNO	2017-03-04	20:49:00	out	-30.135	-106.105	-12.281
JUNO	2017-03-05	08:24:00	in	-30.119	-105.725	-11.924
JUNO	2017-03-08	15:17:00	out	-29.629	-101.861	-9.36
JUNO	2017-03-09	07:05:00	in	-29.446	-100.811	-8.819
JUNO	2017-03-09	09:58:00	out	-29.41	-100.609	-8.72
JUNO	2017-03-09	13:53:00	in	-29.358	-100.329	-8.584
JUNO	2017-03-09	14:57:00	out	-29.344	-100.252	-8.547
JUNO	2017-03-09	15:21:00	in	-29.339	-100.223	-8.533
JUNO	2017-03-10	00:50:00	out	-29.205	-99.516	-8.201
JUNO	2017-03-10	08:53:00	in	-29.083	-98.888	-7.918
JUNO	2017-03-12	13:14:00	out	-28.081	-94.154	-6.023
JUNO	2017-03-12	19:48:00	in	-27.929	-93.478	-5.779
JUNO	2017-04-08	15:02:00	out	-27.174	-84.02	-22.178
JUNO	2017-04-10	00:05:00	in	-28.742	-88.085	-22.145
JUNO	2017-04-11	10:26:00	out	-30.213	-91.773	-21.978
JUNO	2017-04-12	03:49:00	in	-30.899	-93.444	-21.847
JUNO	2017-04-12	21:17:00	out	-31.551	-94.997	-21.687
JUNO	2017-04-13	13:39:00	in	-32.127	-96.341	-21.511
JUNO	2017-04-19	16:18:00	out	-35.902	-103.959	-19.016
JUNO	2017-04-20	08:26:00	in	-36.168	-104.339	-18.653
JUNO	2017-05-05	13:14:00	out	-33.578	-89.079	-6.917
JUNO	2017-05-06	18:12:00	in	-32.516	-85.662	-5.742
JUNO	2017-05-06	21:04:00	out	-32.402	-85.302	-5.624
JUNO	2017-05-06	23:57:00	in	-32.286	-84.935	-5.505
JUNO	2017-05-31	13:02:00	out	-32.572	-81.692	-23.911
JUNO	2017-05-31	21:38:00	in	-33.069	-82.765	-23.937
JUNO	2017-06-01	18:17:00	out	-34.209	-85.196	-23.96
JUNO	2017-06-02	01:25:00	in	-34.586	-85.991	-23.955
JUNO	2017-06-02	20:46:00	out	-35.567	-88.033	-23.912
JUNO	2017-06-02	23:46:00	in	-35.714	-88.335	-23.901
JUNO	2017-06-06	00:18:00	out	-38.844	-94.527	-23.356
JUNO	2017-06-06	00:30:00	in	-38.851	-94.541	-23.354
JUNO	2017-06-16	08:18:00	out	-43.99	-101.628	-18.281
JUNO	2017-06-16	09:58:00	in	-43.996	-101.608	-18.233
JUNO	2017-06-16	10:46:00	out	-43.999	-101.597	-18.21

following on the next page

DATE	**TIME**	**IN/OUT**	**SC**			
JUNO	2017-06-17	14:12:00	in	-44.04	-101.123	-17.4
JUNO	2017-06-18	09:02:00	out	-44.006	-100.655	-16.819
JUNO	2017-06-18	23:42:00	in	-43.943	-100.21	-16.353
JUNO	2017-06-19	01:44:00	out	-43.932	-100.143	-16.287
JUNO	2017-06-19	03:35:00	in	-43.921	-100.08	-16.227
JUNO	2017-06-27	21:27:00	out	-39.004	-85.04	-8.298
JUNO	2017-06-28	12:58:00	in	-38.303	-83.224	-7.627
JUNO	2017-06-28	14:48:00	out	-38.217	-83.002	-7.547
JUNO	2017-06-28	18:10:00	in	-38.056	-82.59	-7.399
JUNO	2017-06-28	21:11:00	out	-37.909	-82.217	-7.267
JUNO	2017-06-29	01:58:00	in	-37.673	-81.615	-7.056
JUNO	2017-06-29	02:18:00	out	-37.656	-81.573	-7.042
JUNO	2017-06-29	02:40:00	in	-37.638	-81.526	-7.025
JUNO	2017-06-29	02:53:00	out	-37.627	-81.498	-7.016
JUNO	2017-06-29	02:58:00	in	-37.623	-81.488	-7.012
JUNO	2017-06-29	03:43:00	out	-37.585	-81.392	-6.979
JUNO	2017-06-29	04:05:00	in	-37.566	-81.345	-6.963
JUNO	2017-06-29	04:17:00	out	-37.556	-81.319	-6.954
JUNO	2017-06-29	05:14:00	in	-37.508	-81.197	-6.912
JUNO	2017-06-29	05:41:00	out	-37.485	-81.14	-6.892
JUNO	2017-06-29	05:44:00	in	-37.482	-81.133	-6.89
JUNO	2017-06-29	07:46:00	out	-37.378	-80.87	-6.799
JUNO	2017-06-29	09:31:00	in	-37.288	-80.642	-6.722
JUNO	2017-08-08	08:28:00	out	-50.535	-98.053	-20.357
JUNO	2017-08-08	08:40:00	in	-50.536	-98.051	-20.351
JUNO	2017-08-13	00:52:00	out	-49.796	-94.561	-16.694
JUNO	2017-08-13	03:43:00	in	-49.749	-94.419	-16.591
JUNO	2017-09-14	23:21:00	out	-43.862	-77.933	-27.473
JUNO	2017-09-15	18:42:00	in	-45.191	-79.964	-27.567
JUNO	2017-10-01	05:48:00	out	-56.797	-93.645	-21.707
JUNO	2017-10-02	18:29:00	in	-56.592	-92.68	-20.519
JUNO	2017-10-02	18:52:00	out	-56.588	-92.668	-20.506
JUNO	2017-10-02	22:39:00	in	-56.552	-92.544	-20.378
JUNO	2017-10-03	01:54:00	out	-56.519	-92.435	-20.268
JUNO	2017-10-03	08:56:00	in	-56.44	-92.187	-20.026
JUNO	2017-11-10	11:18:00	out	-54.554	-82.162	-29.456
JUNO	2017-11-10	12:56:00	in	-54.648	-82.277	-29.451
JUNO	2018-01-06	08:43:00	out	-64.216	-82.732	-30.537
JUNO	2018-01-06	11:19:00	in	-64.323	-82.829	-30.504
JUNO	2018-06-16	13:24:00	out	-80.414	-69.082	-35.209
JUNO	2018-06-16	13:35:00	in	-80.42	-69.084	-35.206
JUNO	2018-06-16	13:51:00	out	-80.429	-69.088	-35.201
JUNO	2018-06-16	14:03:00	in	-80.435	-69.091	-35.198

following on the next page

DATE	**TIME**	**IN/OUT**	**SC**			
JUNO	2018-06-16	14:28:00	out	-80.449	-69.097	-35.191
JUNO	2018-06-16	15:13:00	in	-80.473	-69.107	-35.178
JUNO	2018-06-16	16:14:00	out	-80.505	-69.12	-35.161
JUNO	2018-06-16	17:09:00	in	-80.534	-69.132	-35.145
JUNO	2018-08-04	06:30:00	out	-79.297	-60.942	-37.932
JUNO	2018-08-04	08:51:00	in	-79.441	-61.021	-37.924
JUNO	2021-12-25	19:45:00	out	-51.738	67.232	-46.737
JUNO	2021-12-26	12:10:00	in	-51.29	66.959	-45.893
JUNO	2022-02-16	06:25:00	out	-36.593	57.449	-31.68
JUNO	2022-02-16	07:17:00	out	-36.521	57.355	-31.588
JUNO	2022-02-16	11:15:00	in	-36.189	56.92	-31.161
JUNO	2022-02-16	11:15:00	in	-36.189	56.92	-31.161
JUNO	2022-03-19	08:17:00	out	-43.932	71.335	-52.422
JUNO	2022-03-19	08:20:00	out	-43.932	71.336	-52.42
JUNO	2022-03-19	22:59:00	in	-43.859	71.53	-51.982
JUNO	2022-03-19	22:59:00	in	-43.859	71.53	-51.982
JUNO	2022-05-08	12:52:00	out	-36.156	70.861	-45.823
JUNO	2022-05-08	15:42:00	in	-36.057	70.736	-45.627
JUNO	2022-06-07	21:52:00	out	-33.202	67.787	-55.869
JUNO	2022-06-08	06:56:00	in	-33.39	68.397	-55.982
JUNO	2022-06-08	11:12:00	out	-33.473	68.674	-56.026
JUNO	2022-06-08	11:28:00	in	-33.478	68.691	-56.029
JUNO	2022-06-08	11:40:00	out	-33.482	68.704	-56.03
JUNO	2022-06-08	16:33:00	in	-33.573	69.012	-56.074
JUNO	2022-06-09	00:54:00	out	-33.717	69.519	-56.132
JUNO	2022-06-09	10:12:00	in	-33.864	70.055	-56.173
JUNO	2022-06-09	12:45:00	out	-33.901	70.196	-56.18
JUNO	2022-06-10	15:44:00	in	-34.226	71.553	-56.141
JUNO	2022-06-17	13:21:00	out	-33.536	74.301	-51.659
JUNO	2022-06-18	17:45:00	in	-32.963	73.778	-50.178

Appendix C

Computed normals for all spacecrafts

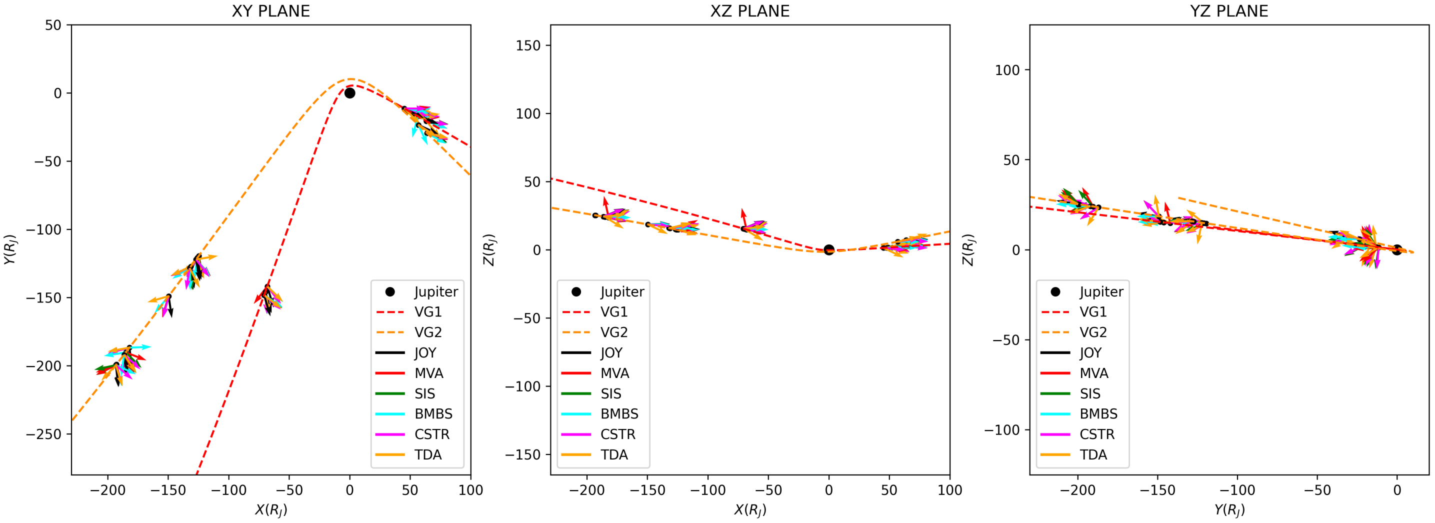

Figure C.1: Trajectory of the Voyager missions in the XY, XZ, and YZ planes with the model and methods normals computed at the different crossings in different colours.

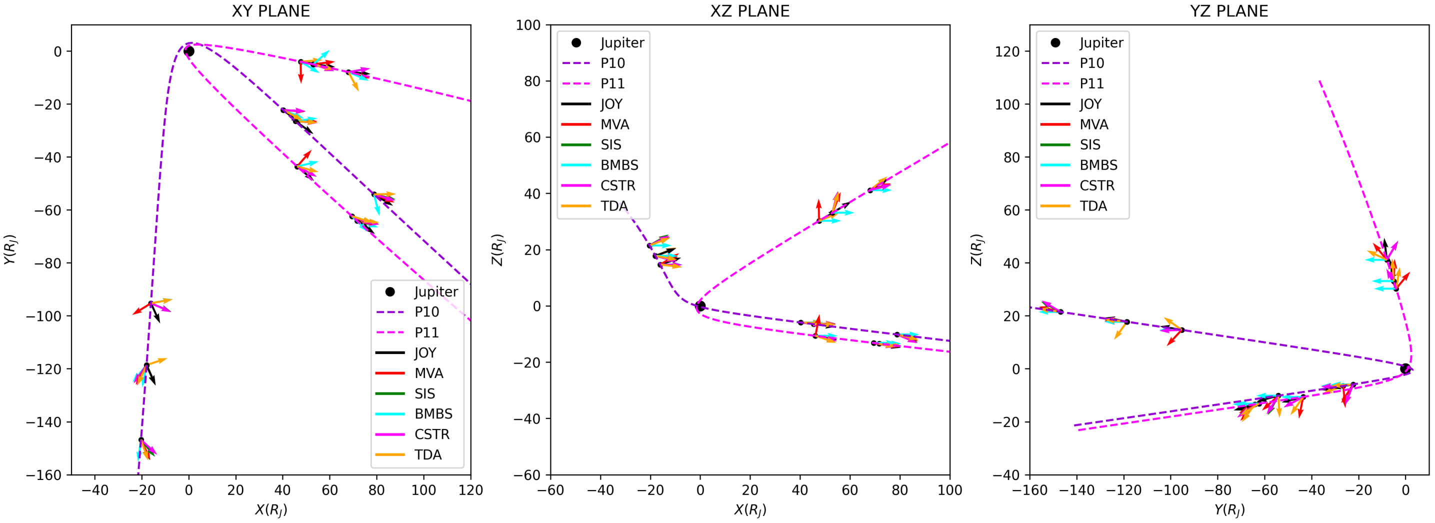

Figure C.2: Trajectory of the Pioneer missions in the XY, XZ, and YZ planes with the model and methods normals computed at the different crossings in different colours.

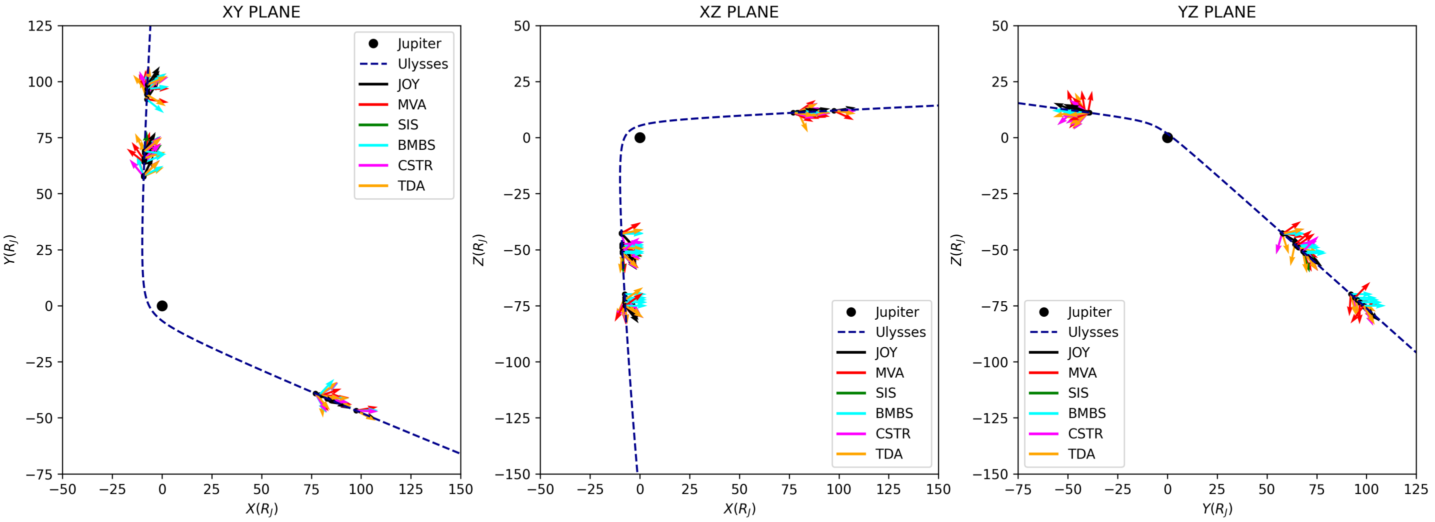

Figure C.3: Trajectory of Ulysses in the XY, XZ, and YZ planes with the model and methods normals computed at the different crossings in different colours.

Appendix D

Statistical results

D.1 Optimised windows

Table D.1: Angles between the normals at consecutive crossings in the XY plane. The angles between the vectors from an **in** to an **out** crossing are plotted in pink, and in green for the inverse. The results are displayed for both sides of the magnetopause, and for the BMBS, CSTR, and TDA methods.

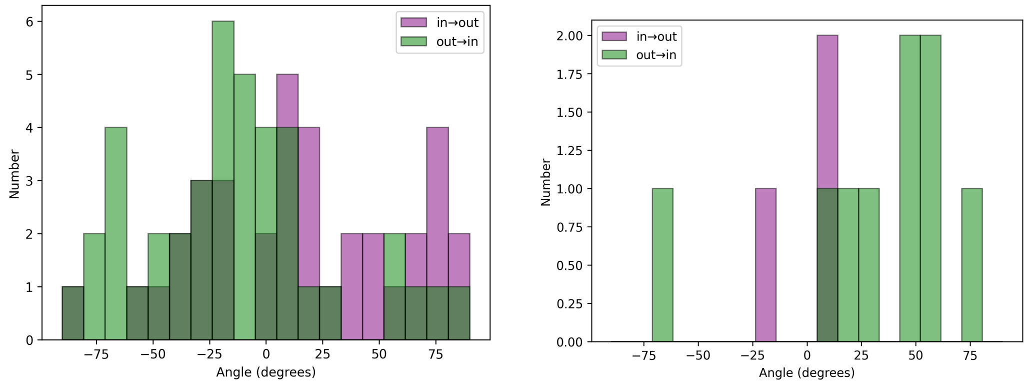

BMBS on dawn side

BMBS on dusk side

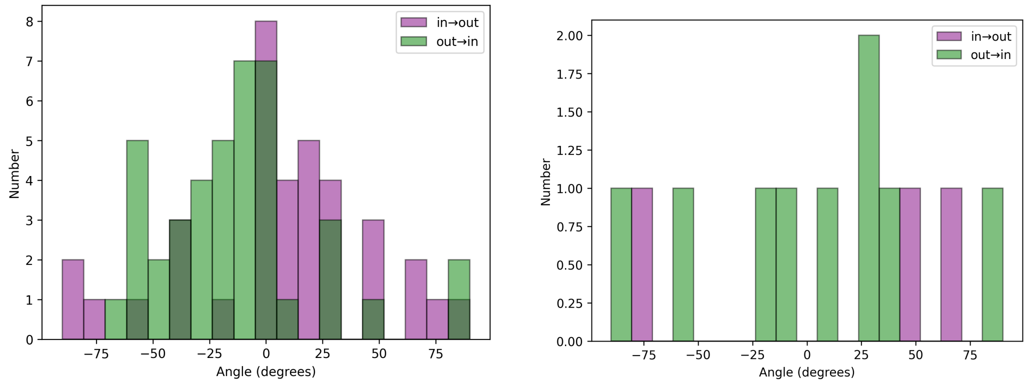

CSTR on dawn side

CSTR on dusk side

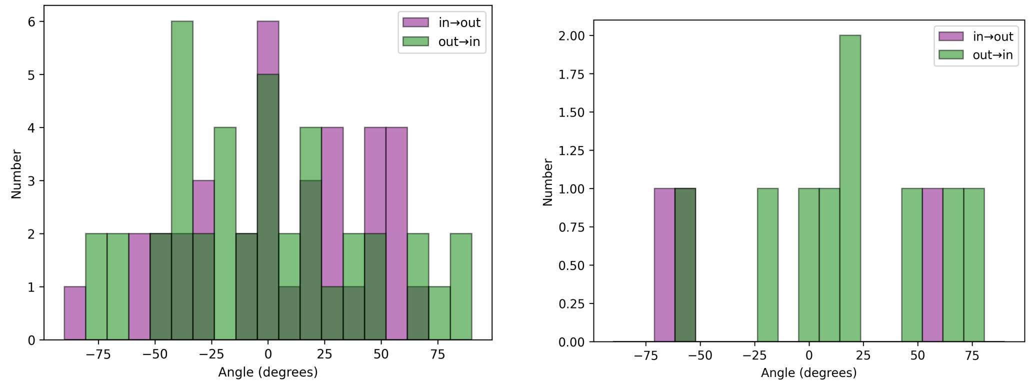

TDA on dawn side

TDA on dusk side

Table D.2: Angles between the normal of Joy et al. (2002) and the method normal, measured in the XY plane. The colours differentiate the angles measured at **in** or **out** crossings. The results are displayed for both sides of the magnetopause, and for the BMBS, CSTR, and TDA methods.

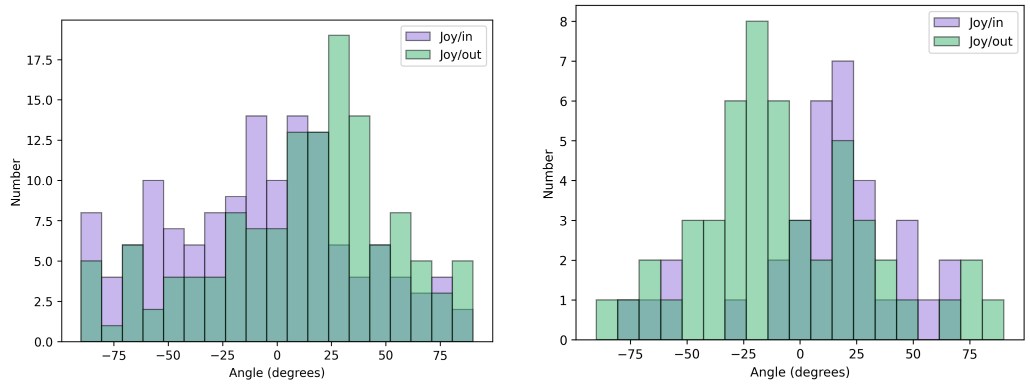

BMBS on dawn side

BMBS on dusk side

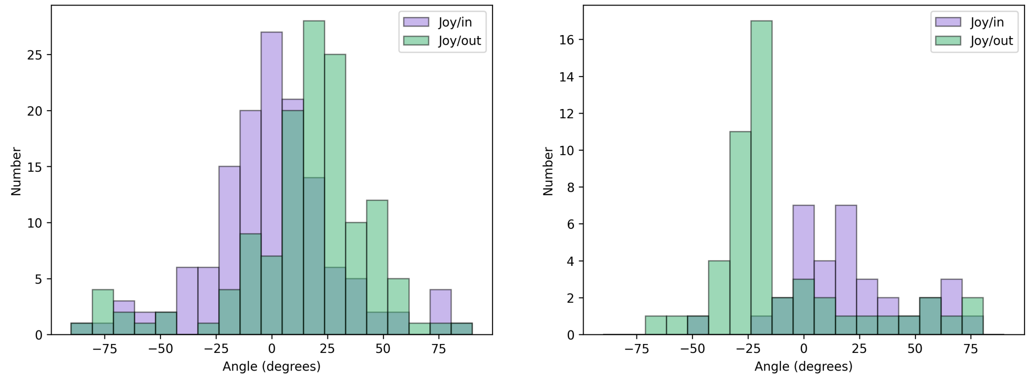

CSTR on dawn side

CSTR on dusk side

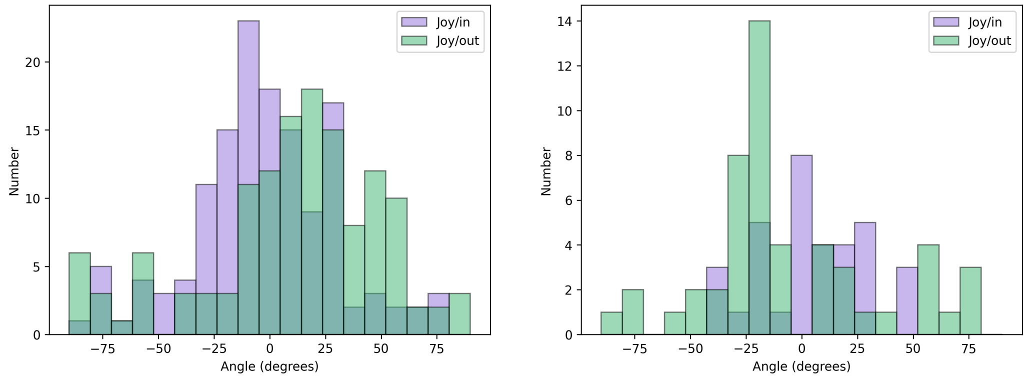

TDA on dawn side

TDA on dusk side

D.2 Fixed windows

Table D.3: Angles between the normals at consecutive crossings in the XY plane. The angles between the vectors from an **in** to an **out** crossing are plotted in pink, and in green for the inverse. The results are displayed for both sides of the magnetopause, and for the MVA, SIS, BMBS, CSTR, and TDA methods.

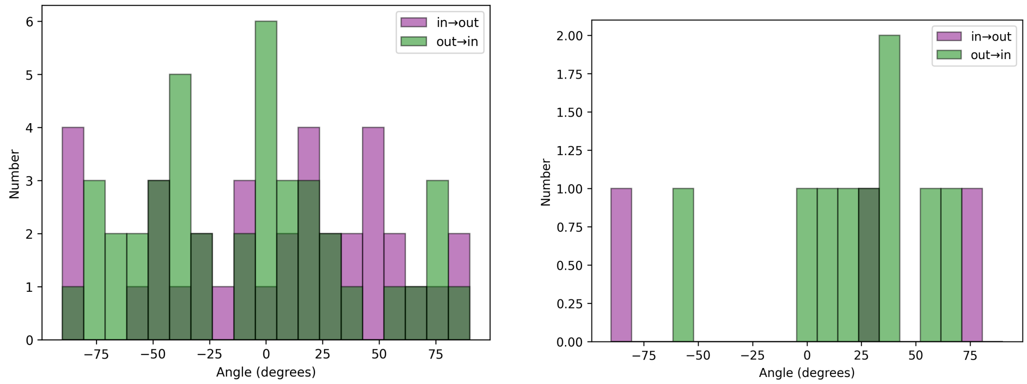

MVA on dawn side

MVA on dusk side

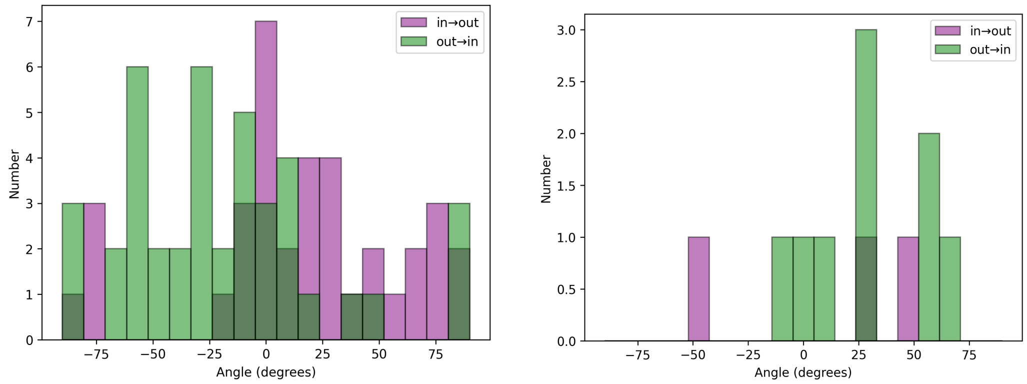

SIS on dawn side

SIS on dusk side

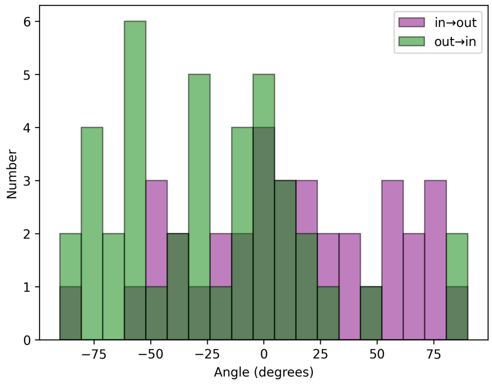

BMBS on dawn side

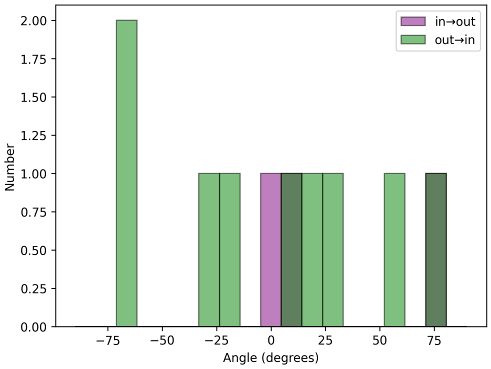

BMBS on dusk side

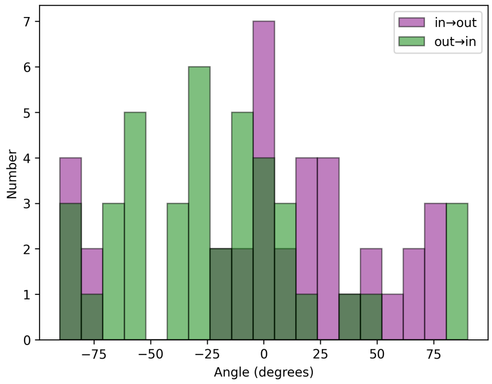

CSTR on dawn side

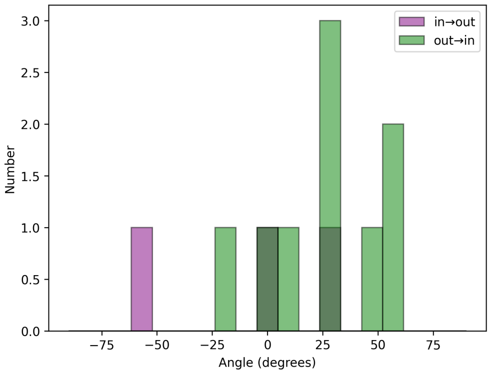

CSTR on dusk side

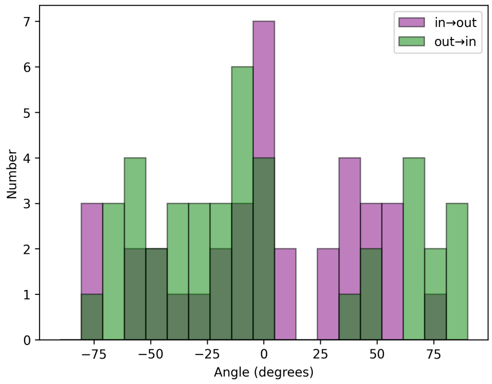

TDA on dawn side

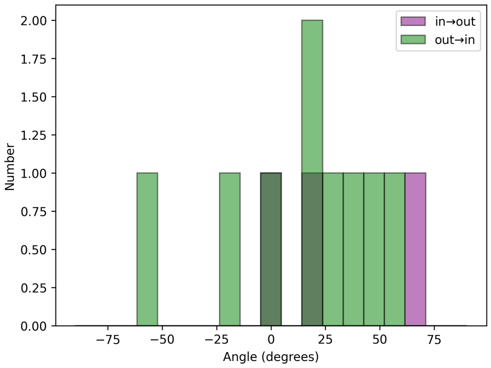

TDA on dusk side

Table D.4: Angles between the normal of Joy et al. (2002) and the method normal, measured in the XY plane. The colours differentiate the angles measured at **in** or **out** crossings. The results are displayed for both sides of the magnetopause, and for the MVA, SIS, BMBS, CSTR, and TDA methods.

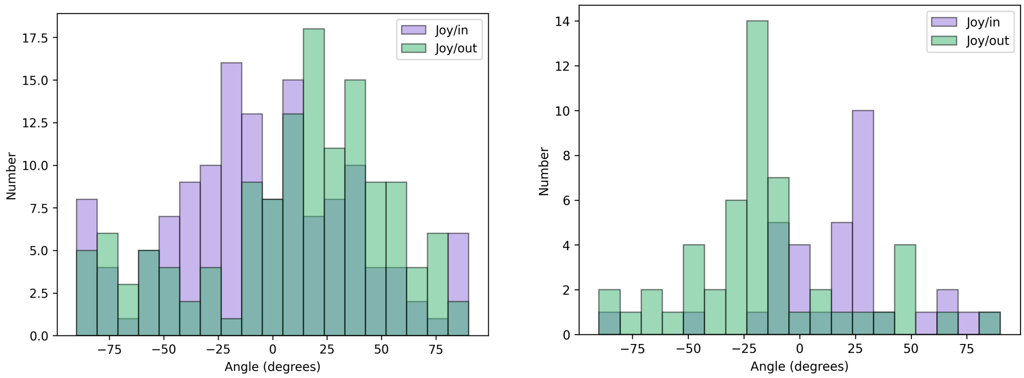

MVA on dawn side MVA on dusk side

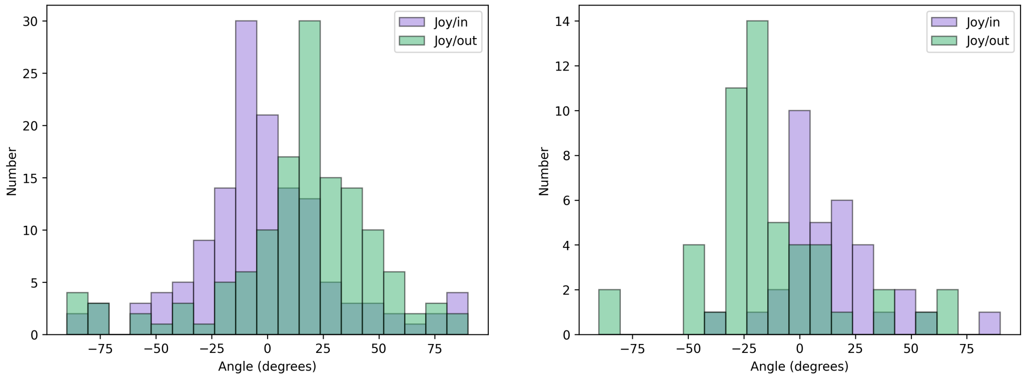

SIS on dawn side SIS on dusk side

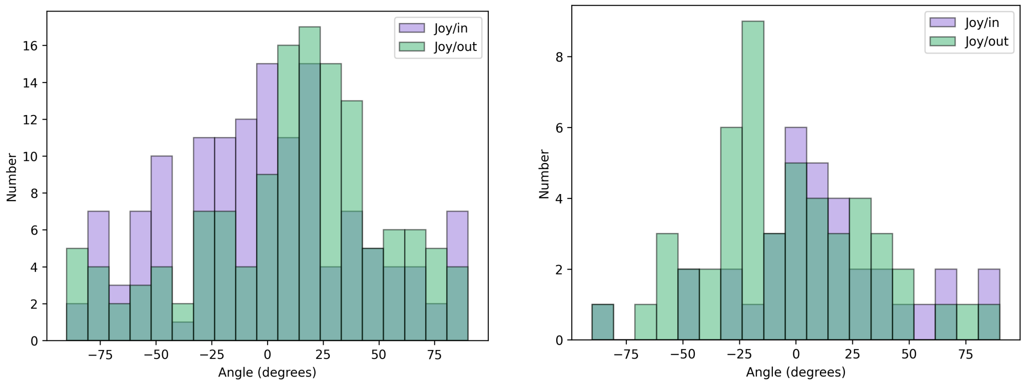

BMBS on dawn side BMBS on dusk side

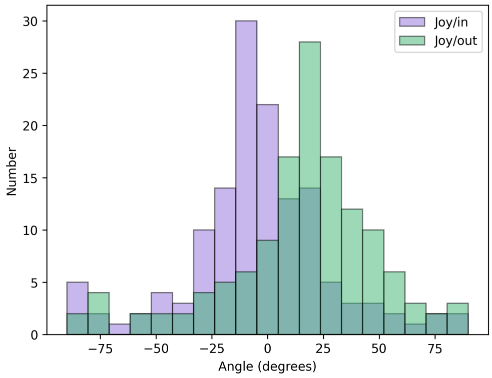

CSTR on dawn side

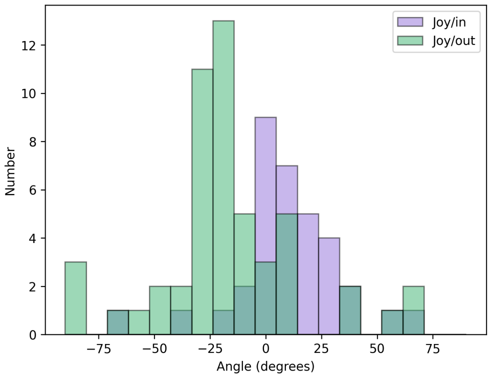

CSTR on dusk side

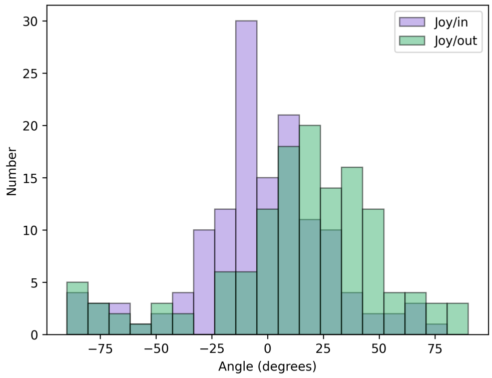

TDA on dawn side

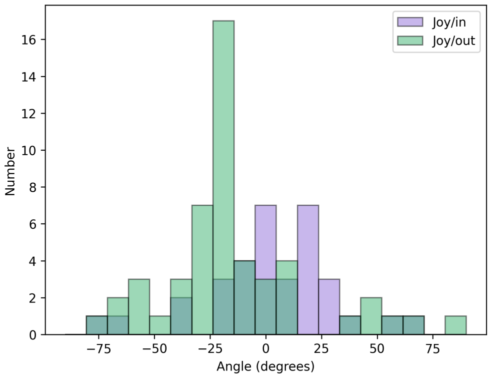

TDA on dusk side

Appendix E

Case study

E.1 Galileo

E.1.1 29 May 1996

TIME	IN/OUT	X (R_J)	Y (R_J)	ANGLE (°)
14:51:00	in	-62.34	-155.78	-39.69
15:48:00	out	-62.25	-155.68	40.44
17:20:00	in	-62.10	-155.52	-27.43

Table E.1: Time, direction, position and angle between the normal by Siscoe and the normal by Joy in the XY plane, for the three consecutive alternate crossings made by Galileo on 29 May 1996.

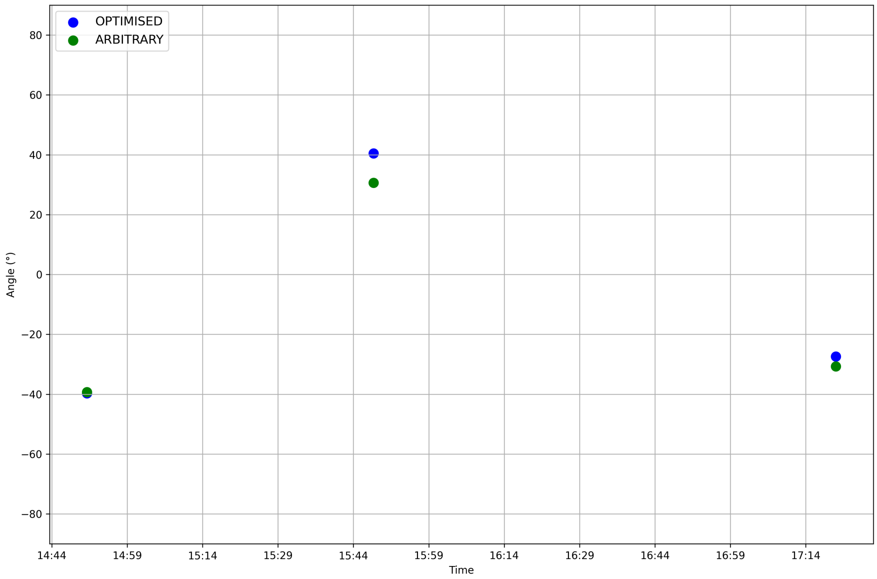

Figure E.1: Angles between the Siscoe's normal computed by the different options and the normal of Joy et al. (2002) in the XY plane for the 29 May 1996 crossings.

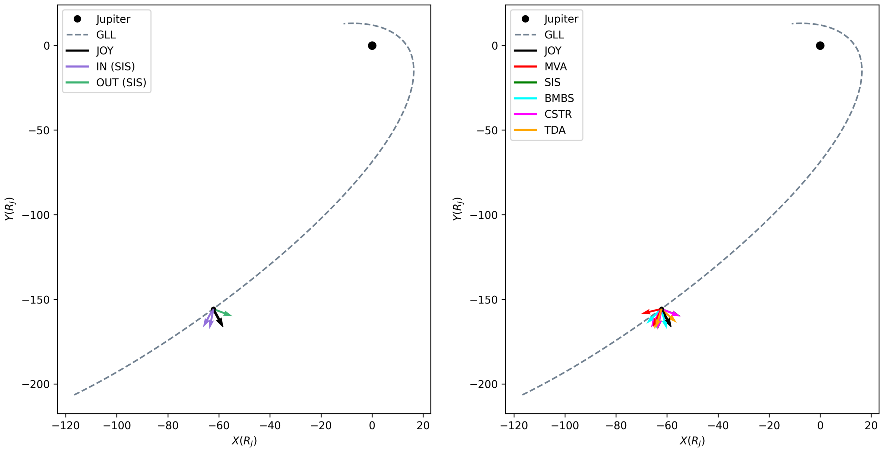

(a) Trajectory between 29 April 1996 and 29 June 1996.

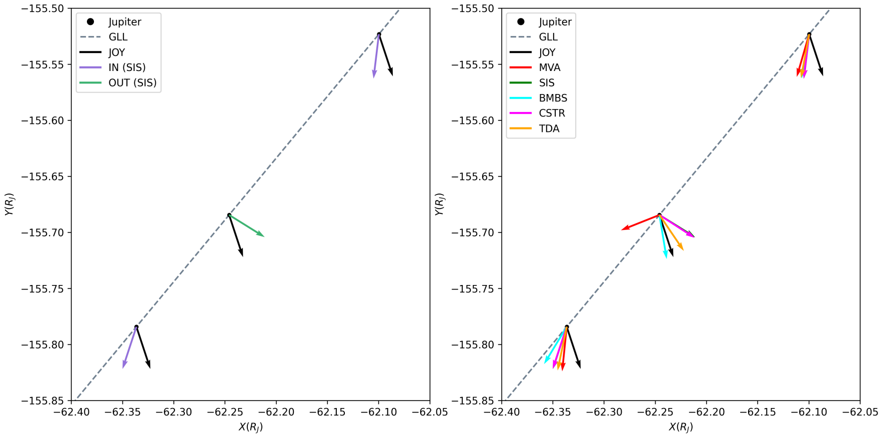

(b) Trajectory on 29 May 1996, around 16:00.

Figure E.2: Trajectory of Galileo in the XY plane. The normals computed via the model of Joy et al. (2002) are plotted on both figures. On the left figure are plotted the normals computed via the SIS method, with the two colours for the **in** and **out** crossings. On the right figure are plotted the normals computed via the different methods, one for each colour.

E.2 Juno

E.2.1 1 August 2016

TIME	IN/OUT	X (R_J)	Y (R_J)	ANGLE (°)
19:36:00	out	0.43	-113.12	30.64
20:57:00	in	0.43	-113.11	-9.95
21:55:00	out	0.42	-113.10	35.38

Table E.2: Time, direction, position and angle between the normal by Siscoe and the normal by Joy in the XY plane, for the three consecutive alternate crossings made by Juno on 1 August 2016.

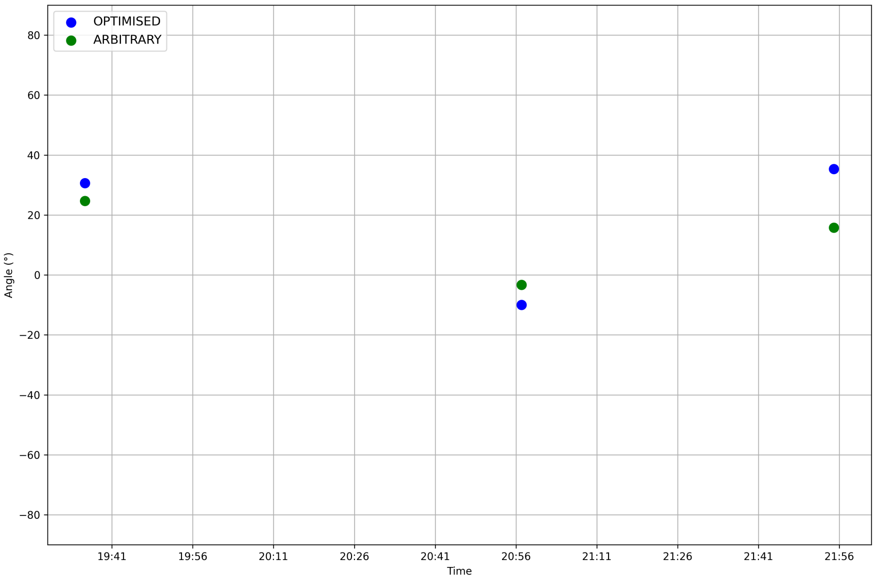

Figure E.3: Angles between the Siscoe's normal computed by the different options and the normal of Joy et al. (2002) in the XY plane for the 1 August 2016 crossings.

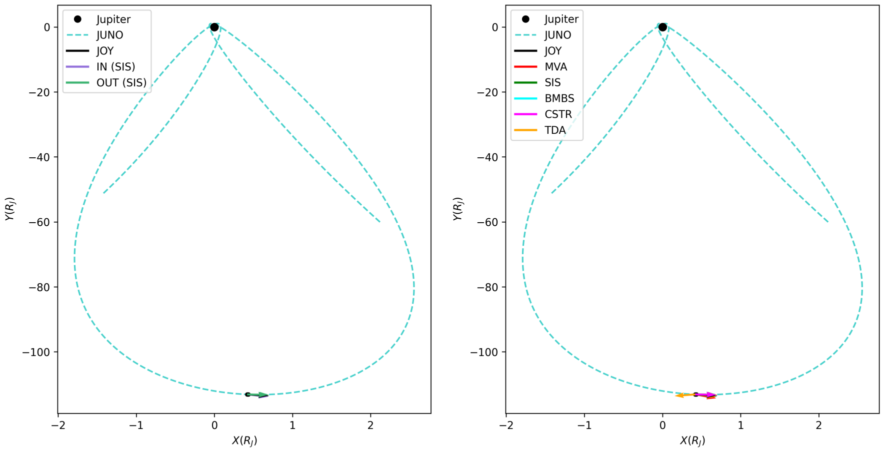

(a) Trajectory between 1 July 2016 and 1 September 2016.

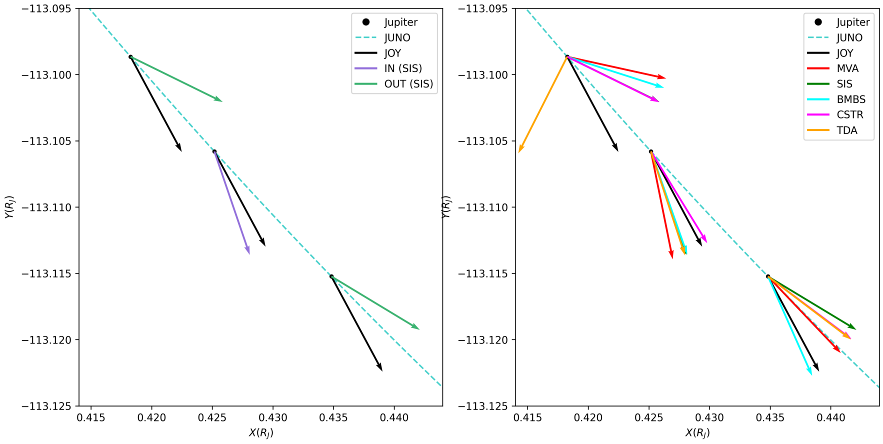

(b) Trajectory on 1 August 2016, around 21:00.

Figure E.4: Trajectory of Juno in the XY plane. The normals computed via the model of Joy et al. (2002) are plotted on both figures. On the left figure are plotted the normals computed via the SIS method, with the two colours for the **in** and **out** crossings. On the right figure are plotted the normals computed via the different methods, one for each colour.

E.2.2 19 June 2017

TIME	IN/OUT	X (R_J)	Y (R_J)	ANGLE (°)
23:42:00	in	-43.94	-100.21	-5.7
01:44:00	out	-43.93	-100.14	16.07
03:35:00	in	-43.92	-100.08	-10.8

Table E.3: Time, direction, position and angle between the normal by Siscoe and the normal by Joy in the XY plane, for the three consecutive alternate crossings made by Juno on 19 June 2017.

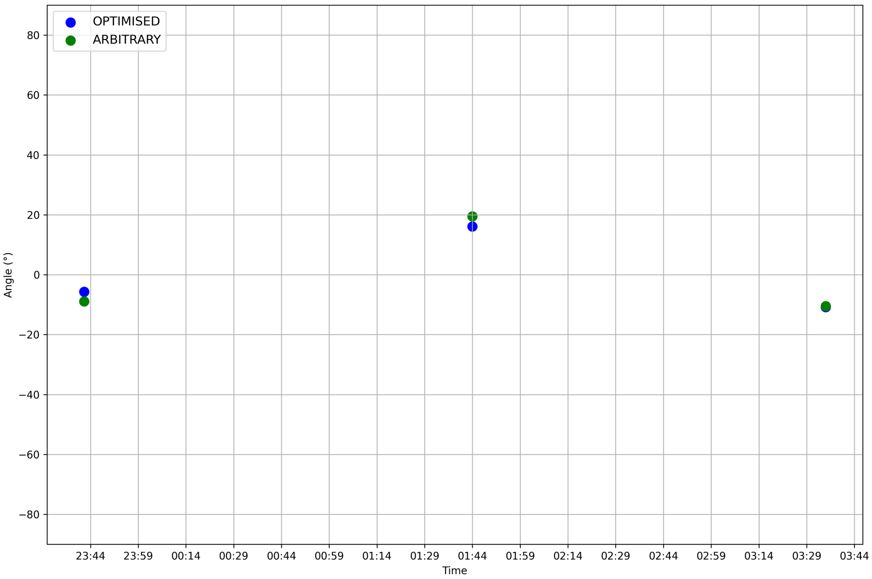

Figure E.5: Angles between the Siscoe's normal computed by the different options and the normal of Joy et al. (2002) in the XY plane for the 19 June 2017 crossings.

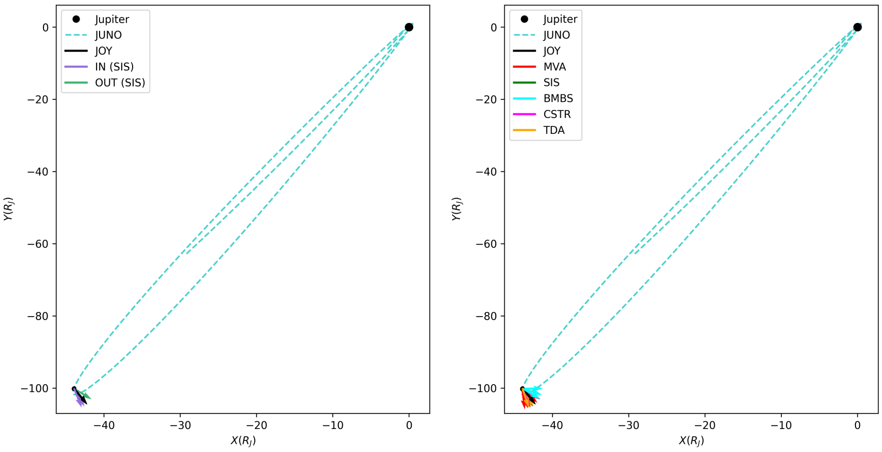

(a) Trajectory between 19 May 2017 and 19 July 2017.

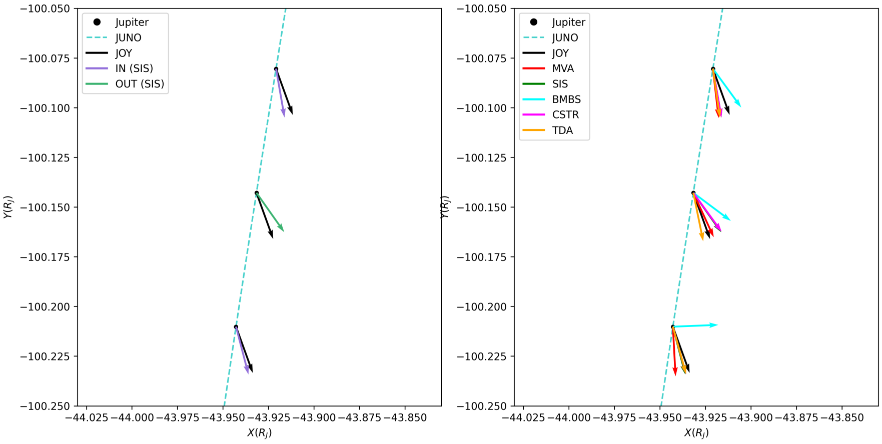

(b) Trajectory on 19 June, around 01:30.

Figure E.6: Trajectory of Juno in the XY plane. The normals computed via the model of Joy et al. (2002) are plotted on both figures. On the left figure are plotted the normals computed via the SIS method, with the two colours for the **in** and **out** crossings. On the right figure are plotted the normals computed via the different methods, one for each colour.

Bibliography

Achilleos, Nicholas et al. [2015]. “1. Transport of mass, momentum and energy in planetary magnetodisc regions”. In: *Space Science Reviews* 187.1, pp. 229–299.

Bagenal, F and RJ Wilson [2016]. *Jupiter coordinate systems*. URL: https://lasp.colorado.edu/mop/files/2015/02/CoOrd_systems12.pdf.

Bagenal, Fran [Oct. 2024]. *Magnetosphere of Jupiter*. DOI: 10.1093/acrefore/9780190647926.013.165. URL: https://oxfordre.com/planetaryscience/view/10.1093/acrefore/9780190647926.001.0001/acrefore-9780190647926-e-165.

Bagenal, Fran and Steve Bartlett [2025]. URL: https://lasp.colorado.edu/mop/resources/graphics/.

Bagenal, Fran and Peter A. Delamere [2011]. “Flow of mass and energy in the magnetospheres of Jupiter and Saturn”. In: *Journal of Geophysical Research: Space Physics* 116.A5.

Bennett, James S et al. [2021]. “Precision magnetometers for aerospace applications: A review”. In: *Sensors* 21.16, p. 5568.

Bolton, Scott J et al. [2017]. “The juno mission”. In: *Space Science Reviews* 213.1, pp. 5–37.

Collier, Michael R. et al. [2020]. “A K-Means Clustering Analysis of the Jovian and Terrestrial Magnetopauses: A Technique to Classify Global Magnetospheric Behavior”. In: *Journal of Geophysical Research: Planets* 125.9, e2019JE006366. DOI: https://doi.org/10.1029/2019JE006366.

Connerney, J. E. P. et al. [2017]. “The Juno Magnetic Field Investigation”. In: *Space Science Reviews* 213, pp. 39–138. DOI: https://doi.org/10.1007/s11214-017-0334-z.

Cutler, JC et al. [2011]. “Evidence of surface wave on the dusk flank of Saturn’s magnetopause possibly caused by the Kelvin-Helmholtz instability”. In: *Journal of Geophysical Research: Space Physics* 116.A10.

Delamere, PA and F Bagenal [2010]. “Solar wind interaction with Jupiter’s magnetosphere”. In: *Journal of Geophysical Research: Space Physics* 115.A10.

Delamere, PA, RJ Wilson, et al. [2013]. “Magnetic signatures of Kelvin-Helmholtz vortices on Saturn’s magnetopause: Global survey”. In: *Journal of Geophysical Research: Space Physics* 118.1, pp. 393–404.

Ebert, R. W. et al. [2017]. “Accelerated flows at Jupiter’s magnetopause: Evidence for magnetic reconnection along the dawn flank”. In: *Geophysical Research Letters* 44.10, pp. 4401–4409. DOI: https://doi.org/10.1002/2016GL072187.

Fairfield, DH et al. [2000]. "Geotail observations of the Kelvin-Helmholtz instability at the equatorial magnetotail boundary for parallel northward fields". In: *Journal of Geophysical Research: Space Physics* 105.A9, pp. 21159–21173.

Feng, Enhao, Binzheng Zhang, et al. [2023]. "Variation of the Jovian magnetopause under constant solar wind conditions: Significance of magnetodisc dynamics". In: *Geophysical Research Letters* 50.12, e2023GL104046.

— [2025]. "Control of the Jovian magnetopause by iogenic plasma: Initial results from global MHD simulations". In: *Geophysical Research Letters* 52.7, e2024GL112624.

Feng, Enhao, Zhiqi Zheng, et al. [2025]. "Dawn-dusk asymmetry of Kelvin-Helmholtz vortices along the Kronian magnetopause". In: *Geophysical Research Letters* 52.11, e2025GL114758.

GeoGebra [2025]. Accessed lastly on August 5, 2025. URL: https://www.geogebra.org/?lang=fr.

Guillot, Tristan et al. [2022]. "Giant planets from the inside-out". In: *arXiv preprint arXiv:2205.04100*.

Helled, Ravit and Saburo Howard [2024]. "Giant planet interiors and atmospheres". In: *arXiv preprint arXiv:2407.05853*.

Helled, Ravit, Naor Movshovitz, and Nadine Nettelmann [2023]. "The nature of gas giant planets". In: *Planetary Systems Now*, pp. 181–210.

Ikoma, Masahiro and Hiroshi Kobayashi [2025]. "Formation of Giant Planets". In: *Annual Review of Astronomy and Astrophysics* 63.

Intriligator, DS and JH Wolfe [1976]. "Results of the plasma analyzer experiment on Pioneers 10 and 11". In: *IAU Colloq. 30: Jupiter: Studies of the Interior, Atmosp here, Magnetosphere and Satellites*, pp. 848–869.

Joy, SP et al. [2002]. "Probabilistic models of the Jovian magnetopause and bow shock locations". In: *Journal of Geophysical Research: Space Physics* 107.A10, SMP–17.

Khurana, Krishan K et al. [2004]. "The configuration of Jupiter's magnetosphere". In: *Jupiter. The planet, satellites and magnetosphere* 1, pp. 593–616.

Knetter, T et al. [2004]. "Four-point discontinuity observations using Cluster magnetic field data: A statistical survey". In: *Journal of Geophysical Research: Space Physics* 109.A6.

Krupp, Norbert et al. [2004]. "Dynamics of the Jovian magnetosphere". In: *Jupiter: The planet, satellites and magnetosphere* 1, pp. 617–638.

Kurth, WS et al. [2002]. "The dusk flank of Jupiter's magnetosphere". In: *Nature* 415.6875, pp. 991–994.

Lepping, RP, MJ Silverstein, and Norman F Ness [1981]. *Magnetic field measurements at Jupiter by Voyagers 1 and 2: Daily plots of 48 second averages.* Technical Memorandum 83864. NASA.

Louis, C. K. et al. [2023]. "Effect of a Magnetospheric Compression on Jovian Radio Emissions: In Situ Case Study Using Juno Data". In: *Journal of Geophysical Research: Space Physics* 128.9, e2022JA031155. DOI: https://doi.org/10.1029/2022JA031155.

Ma, X, PA Delamere, and A Otto [2016]. “Plasma transport driven by the Rayleigh-Taylor instability”. In: *Journal of Geophysical Research: Space Physics* 121.6, pp. 5260–5271.

Ma, X, PA Delamere, A Schok, et al. [2022]. “Jupiter’s sheared flow unstable magnetopause boundary observed by Juno”. In: *Journal of Geophysical Research: Space Physics* 127.10, e2022JA030719.

Ma, Xuanye et al. [2016]. “Interaction between reconnection and Kelvin–Helmholtz at the high-latitude magnetopause”. In: *Advances in Space Research* 58.2, pp. 231–239.

Masson, A and K Nykyri [2018]. “Kelvin–Helmholtz instability: Lessons learned and ways forward”. In: *Space Science Reviews* 214.4, p. 71.

Masters, A et al. [2009]. “Surface waves on Saturn’s dawn flank magnetopause driven by the Kelvin–Helmholtz instability”. In: *Planetary and Space Science* 57.14-15, pp. 1769–1778.

Masters, Adam et al. [2012]. “Surface waves on Saturn’s magnetopause”. In: *Planetary and Space Science* 65.1, pp. 109–121.

Mizuno, Hiroshi, Kiyoshi Nakazawa, and Chushiro Hayashi [1978]. “Instability of a gaseous envelope surrounding a planetary core and formation of giant planets”. In: *Progress of Theoretical Physics* 60.3, pp. 699–710.

Montgomery, Jake et al. [2023]. “Investigating the occurrence of kelvin-helmholtz instabilities at Jupiter’s dawn magnetopause”. In: *Geophysical Research Letters* 50.14, e2023GL102921.

NASA [2025a]. *Jupiter*. https://science.nasa.gov/jupiter/. Accessed on July 1, 2025.

— [2025b]. *Mission - Galileo*. https://science.nasa.gov/mission/galileo/. Accessed on July 1, 2025.

— [2025c]. *Mission - JUNO*. https://science.nasa.gov/mission/juno/. Accessed on July 1, 2025.

— [2025d]. *Mission - Pioneer 10*. https://science.nasa.gov/mission/pioneer-10/. Accessed on July 1, 2025.

— [2025e]. *Mission - Pioneer 11*. https://science.nasa.gov/mission/pioneer-11/. Accessed on July 1, 2025.

— [2025f]. *Mission - Ulysses*. https://science.nasa.gov/mission/ulysses/. Accessed on July 1, 2025.

— [2025g]. *Mission - Voyager 1*. https://science.nasa.gov/mission/voyager/voyager-1/. Accessed on July 1, 2025.

— [2025h]. *Mission - Voyager 2*. https://science.nasa.gov/mission/voyager/voyager-2/. Accessed on July 1, 2025.

— [2025i]. *The Navigation and Ancillary Information Facility - Jet Propulsion Laboratory*. Accessed lastly on August 1, 2025. URL: https://naif.jpl.nasa.gov/naif/index.html.

NASA Planetary Data System [1998a]. *UL one-minute MAG dataset*. DOI: 10.17189/1519874. URL: https://pds-ppi.igpp.ucla.edu/collection/ULY-J-VHM/FGM-4-SUMM-JGCOORDS-60S-V1.0.

NASA Planetary Data System [1998b]. *VG1 1.92S MAG dataset.* DOI: 10.17189/1519884. URL: https://pds-ppi.igpp.ucla.edu/collection/VG1-J-MAG-4-SUMM-HGCOORDS-1.92SEC-V1.0.

— [2001]. *P11 one-minute MAG dataset.* DOI: 10.17189/1519770. URL: https://pds-ppi.igpp.ucla.edu/collection/P10-J-HVM-4-SUMM-S3COORDS-1MIN-V1.0.

— [2004a]. *P10 high-resolution MAG dataset.* DOI: 10.17189/1519768. URL: https://pds-ppi.igpp.ucla.edu/collection/P10-J-HVM-3-RDR-HIGHRES-V1.0.

— [2004b]. *P11 high-resolution MAG dataset.* DOI: 10.17189/1519783. URL: https://pds-ppi.igpp.ucla.edu/collection/P11-J-HVM-3-RDR-HIGHRES-V1.0.

— [2022]. *VG2 1.92S MAG dataset.* DOI: 10.17189/pwc8-5732. URL: https://pds-ppi.igpp.ucla.edu/collection/VG2-J-MAG-4-RDR-HGCOORDS-1.92SEC-V1.0.

— [2024a]. *Galileo Jupiter Magnetometer Magnetospheric Survey Data Collection.* DOI: 10.17189/fq45-wv97. URL: https://pds-ppi.igpp.ucla.edu/data/galileo-mag-jup-calibrated/data-magspheric-survey/.

— [2024b]. *Juno MAG CALIBRATED DATA.* NASA Planetary Data System. DOI: 10.17189/1519711. URL: https://pds-ppi.igpp.ucla.edu/collection/JNO-J-3-FGM-CAL-V1.0.

— [2025a]. *Mission: Galileo.* https://pds-ppi.igpp.ucla.edu/mission/Galileo. Accessed on July 1, 2025.

— [2025b]. *Mission: Juno.* https://pds-ppi.igpp.ucla.edu/mission/Juno. Accessed on July 1, 2025.

— [2025c]. *Mission: Pioneer 10.* https://pds-ppi.igpp.ucla.edu/mission/Pioneer_10. Accessed on July 1, 2025.

— [2025d]. *Mission: Pioneer 11.* https://pds-ppi.igpp.ucla.edu/mission/Pioneer_11. Accessed on July 1, 2025.

— [2025e]. *Mission: Ulysses.* https://pds-ppi.igpp.ucla.edu/mission/Ulysses. Accessed on July 1, 2025.

— [2025f]. *Mission: Voyager.* https://pds-ppi.igpp.ucla.edu/mission/Voyager. Accessed on July 1, 2025.

Otto, A and DH Fairfield [2000]. "Kelvin-Helmholtz instability at the magnetotail boundary: MHD simulation and comparison with Geotail observations". In: *Journal of Geophysical Research: Space Physics* 105.A9, pp. 21175–21190.

Ranquist, D. A. et al. [2019]. "Survey of Jupiter's Dawn Magnetosheath Using Juno". In: *Journal of Geophysical Research: Space Physics* 124.11, pp. 9106–9123. DOI: https://doi.org/10.1029/2019JA027382.

Roth, Lorenz et al. [2025]. "Mass supply from Io to Jupiter's magnetosphere". In: *Space Science Reviews* 221.1, p. 13.

Rutala, MJ et al. [2025]. "New models of Jupiter's magnetopause and bow shock through the Juno prime mission: Probabilistic location, shape, and internally-driven variation". In: *Journal of Geophysical Research: Space Physics* 130.5, e2025JA033842.

Saur, Joachim, Emmanuel Chané, and Oliver Hartkorn [2018]. “Modeling magnetospheric fields in the Jupiter system”. In: *Magnetic Fields in the Solar System: Planets, Moons and Solar Wind Interactions*. Springer, pp. 153–182.

Sibeck, David G, RE Lopez, and Edmond C Roelof [1991]. “Solar wind control of the magnetopause shape, location, and motion”. In: *Journal of Geophysical Research: Space Physics* 96.A4, pp. 5489–5495.

Siscoe, GL et al. [1968]. “Power spectra and discontinuities of the interplanetary magnetic field: Mariner 4”. In: *Journal of Geophysical Research* 73.1, pp. 61–82.

Smith, E, B Connor, and G Foster [1975]. “Measuring the magnetic fields of Jupiter and the outer solar system”. In: *IEEE Transactions on Magnetics* 11.4, pp. 962–980.

Song, Pu, RC Elphic, and CT Russell [1988]. “ISEE 1 & 2 observations of the oscillating magnetopause”. In: *Geophysical research letters* 15.8, pp. 744–747.

Sonnerup, BU Ö and LJ Cahill Jr [1967]. “Magnetopause structure and attitude from Explorer 12 observations”. In: *Journal of Geophysical Research* 72.1, pp. 171–183.

— [1968]. “Explorer 12 observations of the magnetopause current layer”. In: *Journal of Geophysical Research* 73.5, pp. 1757–1770.

Southwood, David J and Margaret G Kivelson [1990]. “The magnetohydrodynamic response of the magnetospheric cavity to changes in solar wind pressure”. In: *Journal of Geophysical Research: Space Physics* 95.A3, pp. 2301–2309.

Tanaka, T et al. [2023]. “Radial transport of Io plasma from the inner magnetosphere to the tail”. In: *Journal of Geophysical Research: Space Physics* 128.5, e2022JA030891.

Wei, Songrui et al. [2021]. “Recent progress of fluxgate magnetic sensors: Basic research and application”. In: *Sensors* 21.4, p. 1500.

Zhang, B et al. [2018]. “Asymmetric Kelvin-Helmholtz instability at Jupiter’s magnetopause boundary: Implications for corotation-dominated systems”. In: *Geophysical Research Letters* 45.1, pp. 56–63.